

RICE UNIVERSITY

**Polyethyleneimine functionalized nano-carbons
for the absorption of carbon dioxide**

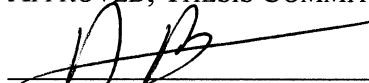
by

Eoghan P. Dillon


A THESIS SUBMITTED
IN PARTIAL FULFILLMENT OF THE
REQUIREMENTS FOR THE DEGREE

Doctor of Philosophy

APPROVED, THESIS COMMITTEE:




Andrew R. Barron, Chair
Charles W. Duncan, Jr. – Welch Chair of
Chemistry and Professor of Materials Science

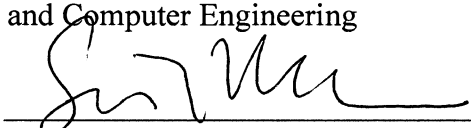


James M. Tour

T. T. and W. F. Chao Professor of Chemistry
Professor of Computer Science
Professor of Mechanical Engineering and Materials
Science



Kevin F. Kelly
Associate Professor of Electrical
and Computer Engineering



Seiichi P. T. Matsuda
E. Dell Butcher Professor of Chemistry and
Professor of Biochemistry & Cell Biology

HOUSTON, TEXAS
NOVEMBER 2011

ABSTRACT

Polyethyleneimine functionalized nano-carbons for the absorption of carbon dioxide

The evolution of nanotechnology over the past 20 years has allowed researchers to use a wide variety of techniques and instruments to synthesize and characterize new materials on the nano scale. Due to their size, these nano materials have a wide variety of interesting properties, including, high tensile strength, novel electronic and optical properties and high surface areas. In any absorption system, a high surface areas is desirable, making carbon nano materials ideal candidates for use in absorption systems. To that end, we have prepared a variety of nano carbons, single walled carbon nanotubes, multi walled carbon nanotubes, graphite intercalation compounds, graphite oxide, phenylalanine modified graphite and fullerenes, for the absorption of carbon dioxide. These nano carbons are functionalized with the polymer, polyethyleneimine, and fully characterized using Raman spectroscopy, x-ray photoelectron spectroscopy, scanning electron microscopy, atomic force microscopy, solid state ^{13}C NMR, and thermogravimetric analysis. The carbon dioxide absorption potential of the PEI-nano carbons was evaluated using thermogravimetric analysis at standard room temperature and pressure. We have demonstrated the high gravimetric capacity of carbon dioxide capture on these materials with extremely high capacities for PEI-C₆₀.

Acknowledgments

During my time here at Rice several collaborations were formed, I would like to take this opportunity to thank them. Many thanks to Dr. Manoop Bhutani of M. D. Anderson Cancer Center for imparting his vast knowledge on pancreatic cancer and endoscopic ultrasound and also, allowing me to observe several endoscopic ultrasound procedures while providing access to the instrument for my experiments. I would also like to thank Dr. Seamus Curran and his lab in the University of Houston, in particular Nigel Alley for the collaboration that was formed.

The shared equipment authority here at Rice University deserves a special thanks for allowing students access to a wide variety of analytical tools. In particular I would like to thank Dr. Angelo Benadeto and Dr. Bo Chen for all of their assistance, training and instrument maintenance. I would also like to thank Dr. Larry Alemany for his assistance in performing solid state NMR experiments that were vital to my research.

I would like to thank all of my committee members; Dr. James Tour, Dr. Kevin Kelly and Dr. Seiichi Matsuda. Dr. Kelly was always available to talk to students about any research interests that they may have, usually over a beer in Valhalla. While mentioning Valhalla it would be rude not to thank all of the managers of Valhalla, past, present and future, for providing graduate students a place to relax and have a beer if they so fancied.

I would most importantly like to thank all of those people I worked with everyday, the members of the Barron group, past and present. In particular, the Irish contingent, Alvin and Sam. It's always nice to have a bit of home with you in a foreign land. I would also like to thank several past members of the group, Chris Hamilton, Jonathan Brege, Nadjemeh Doostar and Chris Crouse, whom I initially worked with when I first arrived here at Rice. There were also several other Irish who came here on internships similar to mine and worked in the Barron lab, Colm and Caoimhe.

I would like to thank FAS, an Irish government agency who brought me here to Rice initially for a six month study. I would like to thank in particular, Dr. Pauline Ward for all of her assistance to the Irish who came over here on the program, it would not have been successful without her.

I would like to thank Dr. Barron for first of all allowing me to come to his lab initially for a six month internship, and allowing me to stay for my PhD even though my knowledge of chemistry was minimal at best. Furthermore he has always stood up for and supported his students, me in particular, even when their own idiocy lands them in trouble. There are not a lot of bosses that have that kind of loyalty and character and it has been a true pleasure to work for Andy. It would be hard to imagine a group that would be more fun to work in, days at the track, trips to several national conferences, fire extinguisher training with the Harris County Hazmat response team, and days trips to the bomb squad.

I Finally and most importantly I would like to thank my family. I was only in the country two weeks when Jonathan offered me tickets to go see a world series game, it was there that I first met my wife Amanda Strom. I can't express enough gratitude for all her help throughout my graduate career. There is no way that I would have survived without her help, from me wanting to quit before my 2nd year oral exam, to her help and guidance during the thesis writing portion of my final year. I cannot wait to finally get up to Dallas and begin our new life together. I would finally like to thank my parents for all their support through the years. They, like Amanda, never gave up on me and I hope this degree in some way makes up for all the report cards they have gotten throughout the years saying "could do better if he applied himself". I could not have asked for better parents.

Table of Contents

Introduction	1
Chapter 1. Synthesis and characterization of polyethyleneimine nanocarbons	
Introduction	10
Results and Discussion	18
Conclusions	49
Experimental	51
References	56
Chapter 2. Carbon Dioxide Absorption Potential of Polyethyleneimine Functionalized Carbon Nanomaterials	
Introduction	60
Results and Discussion	71
Conclusions	87
Experimental	89
References	89
Chapter 3. Small molecule capture and release from PEI-SWNTs	
Introduction	92
Results and Discussion	96
Conclusions	100
Experimental	101
References	102

Abbreviations

μL	microliter(s), 10^{-6} L
μm	micrometer(s), 10^{-6} m
μM	micromolar, 10^{-3} M
A.U.	absorbance units
AFM	atomic force microscopy
atm	atmosphere (101,325 Pa)
Baa	Bucky amino acid, fullerene phenylalanine
Boc	<i>tert</i> -butyloxidecarbonyl, $-\text{C}(\text{O})\text{OC}(\text{CH}_3)_3$
C_{60}	Buckminsterfullerene, [60] fullerene
<i>ca.</i>	circa, approximately
CCS	carbon capture and storage
cm	centimeter, 10^{-2} m
Da.	dalton
DIC	diisopropylcarbodiimide
DNA	deoxyribonucleic acid
EOR	enhanced oil recovery
Eq.	equation
<i>et al.</i>	<i>et alia</i> , and others
EtOH	ethanol, $\text{CH}_3\text{CH}_2\text{OH}$
EUS	endoscopic ultra-sound
eV	electron volts
g	gram
GIC	graphite intercalation compound
GIST	gastrointestinal stromal tumor
GO	graphite oxide

GtCO ₂ yr ⁻¹	giga tons of CO ₂ per year
h	hour
HCC	hyrdophilic carbon clusters
Hz	hertz
i.e.	<i>id est</i> , that is (to say)
IR	infrared spectroscopy
J	Joule
K	kelvin
L	liter(s)
m	meter(s)
M	molar
MEA	monoethanol amine
mg	milligram(s), 10 ⁻³ g
min	minute(s)
mL	milliliter(s), 10 ⁻³ L
mol	mole(s)
M _w	molecular weight
MWNT	multi walled carbon nanotube
NC	nano carbon
nm	nanometer, 10 ⁻⁹ m
NMR	nuclear magnetic resonance spectroscopy
°	degrees
°C	degrees centigrade
ODCB	ortho-dichlorobenzene
PEG	polyethylene glycol
PEI	polyethyleneimine
PEIT	percutaneous ethanol injection therapy

Phe	phenylalanine
PL	phospholipid
ppm	parts per million
PSA	pressure swing adsorption
PTFE	polytetrafluoroethylene
PTX	paclitaxel
QD	quantum dot
R.T.	room temperature
rpm	revolutions per minute
s	second (s)
sccm	standard cubic centimeters per minute
SEM	scanning electron microscopy
STEM	scanning tunneling electron microscopy
STM	scanning tunneling microscopy
SWNT	single walled carbon nanotube
TEA	triethylamine
TEM	transmission electron microscopy
TGA	thermogravimetric analysis
TSA	temperature swing adsorption
UV-vis	ultraviolet/visible spectroscopy
XPS	X-ray photoelectron spectroscopy
δ	delta, chemical shift (NMR)
λ	lambda, wavelength

List of Figures

Introduction

- Figure I.1.** Base forms for nano carbons, (a) C₆₀, (b) SWNT, and (c) graphene/graphite. A. K. Geim and K. S. Novoselov, *Nat Mater*, 2007, **6**, 183-191. 1
- Figure I.2.** Number of research papers on the use of nanomaterials as therapeutic agents in the last 20 years. X. Xue, F. Wang and X. Liu, *J. Mater. Chem.*, 2011, **21**, 13107. 2
- Figure I.3.** Cartoon of the Dai method for the delivery of paclitaxel from pegylated SWNTs. Z. Liu, K. Chen, C. Davis, S. Sherlock, Q. Cao, X. Chen and H. Dai, *Cancer Res.*, 2008, **68**, 6652-6660. 3

Chapter 1

- Figure 1.1.** Various methods for the modification of single and multi-walled carbon nanotubes. 10
- Figure 1.2.** Various methods for the modification of graphitic materials. 14
- Figure 1.3.** Reaction pathways for the chemical modification of fullerenes. 15
- Figure 1.4.** Comparison of (a) non-covalently attached PEI(600)/SWNTs, and (b) covalently attached PEI(600)-SWNTs after aqueous dialysis for 20 minutes and 4 days, respectively. 19
- Figure 1.5.** C_{1s} high-resolution XPS spectra for (a) F-SWNTs and (b) PEI(10000)-SWNTs. Peak fits and assignments are shown. 20

- Figure 1.6.** Plot of the number of PEI molecules per SWNT carbon ($\text{PEI:C}_{\text{SWNT}}$) as a function of the molecular weight (Da). 22
- Figure 1.7.** Raman spectrum (780 nm) of (a) purified SWNTs, (b) F-SWNTs, and (c) PEI(600)-SWNTs. 23
- Figure 1.8.** Plot of the Raman D:G ratio as a function of PEI molecular weight (Da) for PEI-SWNTs. 24
- Figure 1.9.** Schematic representation of PEI-SWNTs with molecular weights of (a) 600 Da, (b) 10000 Da, and (c) 25000 Da, showing the orientation of PEI which represents the results of Table 1.1, indicating why there is no substantial increase PEI:SWNT above 10,000 Da. 25
- Figure 1.10.** UV-Vis spectrum of PEI(600)-SWNTs. 26
- Figure 1.11.** AFM image of a PEI(600)-SWNT showing the presence of PEI “globules”. 26
- Figure 1.12.** TEM images of (a) a single PEI(600)-SWNTs exposed from a bundle and (b) PEI(600)-SWNTs functionalized with gold nanoparticles formed from the reduction of HAuCl_4 by the PEI substituents. 27
- Figure 1.13.** Raman spectra of (a) Bay-MWNTs and (b) PEI-MWNTs. 29
- Figure 1.14.** C1s spectrum of PEI-MWNT showing the presence of C-N bonding at 286.5 eV. 29
- Figure 1.15.** AFM image of PEI-MWNT showing polymer “globules” on MWNT. 30

- Figure 1.16.** AFM sectional analysis of PEI-MWNT showing a height difference of 5.024 nm between functionalized and un-functionalized sections. 31
- Figure 1.17.** SEM analysis of PEI-MWNTs showing large aggregates. 31
- Figure 1.18.** SEM image showing the larger aggregates are composed of PEI-MWNTs. 31
- Figure 1.19.** Raman spectra of (a) Graphite, (b) F-GIC and (c) PEI-GIC. 33
- Figure 1.20.** (a) C1s spectrum, (b) O1s spectrum and (c) N1s spectrum of phenylalanine modified graphite. 36
- Figure 1.21.** (a) C1s and (b) O1s XPS spectra of PEI-Phe-N-G. 37
- Figure 1.22.** Raman spectra of (a) GO and (b) PEI-GO. 39
- Figure 1.23.** XPS C1s spectra of (a) GO and (b) PEI-GO indicating covalent functionalization of GO by PEI. 40
- Figure 1.24.** TEM image of PEI-GIC showing the presence of PEI (black). 41
- Figure 1.25.** AFM image showing the polymer coating on PEI-GIC. 42
- Figure 1.26.** AFM image showing PEI functionalized Phe-G with PEI linkages. 43
- Figure 1.27.** AFM sectional analysis of PEI-Phe(4-N-G) indicating a height of 156.62 nm. 43
- Figure 1.28.** SEM analysis showing large aggregates of PEI-Phe(4-N-G). 44
- Figure 1.29.** AFM image of PEI-GO showing PEI globules on the surface of GO. 44
- Figure 1.30.** SEM image of PEI-GO showing large aggregate structures. 45

- Figure 1.31.** XPS survey analysis showing C1s and N1s peaks of PEI-C₆₀. 47
- Figure 1.32.** C1s XPS spectrum of PEI-C₆₀ showing the presence of C-N bonds at ~ 286.5. 47
- Figure 1.33.** AFM image of PEI-C₆₀ showing internalized C₆₀. 48
- Figure 1.34.** AFM sectional analysis of PEI-C₆₀ indicating a height of ~ 2 nm. 48
- Figure 1.35.** SEM image of PEI-C₆₀ in powdered form showing PEI nodules on exterior. 49

Chapter 2

- Figure 2.1.** Measured CO₂ concentration in the atmosphere at Mauna Loa observatory. Earth System research Laboratory, <http://www.esrl.noaa.gov/gmd/ccgg/trends/>, Accessed 5/15/11, 2011. 61
- Figure 2.2.** Structure of monoethanol amine (MEA). 68
- Figure 2.3.** Structure of branched PEI. 69
- Figure 2.4.** Solid state NMR spectra of PEI(600)-SWNTs. (a) ¹³C MAS NMR spectrum with a 12 kHz spinning speed, and (b) ¹H-¹³C CPMAS spectrum with a 7 kHz spinning speed. 72
- Figure 2.5.** TGA of PEI(25000)-SWNT showing the mass change associated with the adsorption and desorption of CO₂. 74
- Figure 2.6.** A plot of CO₂ adsorption efficiency as a function of molecular weight of the PEI for PEI-SWNTs. 75
- Figure 2.7.** TGA of PEI(600)-SWNT showing the mass change associated with the repeated adsorption and desorption of CO₂ irrespective of

- exposure times. The mass has been normalized to the lowest mass recorded, which is equivalent to PEI(600)-SWNT. 76
- Figure 2.8.** TGA for PEI(10000)-SWNT heated to 110 °C under argon, followed by exposure to CO₂ at a range of temperatures showing the increase in CO₂ adsorption with decrease in temperature. 76
- Figure 2.9.** A plot of CO₂ adsorption efficiency as a function of temperature for PEI(10000)-SWNT. 77
- Figure 2.10.** TGA showing CO₂ absorption capacity of PEI-MWNT, (~ 5%). 78
- Figure 2.11.** TGA curve showing CO₂ absorption capacity of PEI-GIC (~ 1 %). 79
- Figure 2.12.** TGA curve showing the CO₂ absorption potential of PEI-Phe-G (~ 6%). 79
- Figure 2.13.** CO₂ absorption capacity of PEI functionalized graphite oxide, ~ 8%. 80
- Figure 2.14.** TGA curve showing maximum absorption capacity of PEI-C₆₀ (~32%). 81
- Figure 2.15.** TGA curve showing dry CO₂ absorption capacity of PEI-C₆₀ (~3%). 81
- Figure 2.16.** Absorption capacity of wet argon by PEI-C₆₀ (~ 16%). 83
- Figure 2.17.** Water absorption capacity of PEI-C₆₀ using degassed water (~ 9%). 84
- Figure 2.18.** Solid state ¹³C NMR showing the PEI signal at 47 ppm, the fullerene signal 149 ppm and CO₂ 164 ppm. 85
- Figure 2.19.** Solid state ¹³C NMR of ammonium bicarbonate with carbonyl peak at 163.48 ppm 86

Chapter 3

- Figure 3.1.** Diagram of the pathway of EUS through gastrointestinal tract, for direct injection to the pancreas. Large black arrow shows needle

- pathway through gastrointestinal tract to pancreas. Small arrows indicate tumorous mass. Taken from⁸ 91
- Figure 3.2.** Ulcer formation at ethanol injection site. Ulcer is circled in red. Taken from¹¹ 92
- Figure 3.3.** Structure of (a) deoxycytidine and (b) Gemcitabine 93
- Figure 3.4.** Cytotoxicity of various concentrations of gemcitabine against MIA, As-PC-1, PANC-1 and PANC-48 pancreatic cancer cell lines. Taken from¹² 94
- Figure 3.5.** Plot of change in pH as a function of EUS exposure time for AcOH-PEI-SWNTs. 96
- Figure 3.6.** Release of deoxycytidine monitored by UV-Vis spectroscopy (271 nm). 97

List of Tables

Chapter 1

Table 1.1. Selected physical and spectroscopic data for branched PEI-SWNTs.	24
Table 1.2. Carbon, nitrogen, oxygen and fluorine content of PEI-Graphites by XPS and weight percentage of NC content from TGA.	41
Table 1.3. Summary of physical properties of synthesized materials.	50

Chapter 2

Table 2.1. Typical flue gas composition from gas and coal fired power plants. ⁵	62
Table 2.2. Summary of the CO ₂ capacity of PEI modified mesoporous silica's.	70
Table 2.3. Selected physical and spectroscopic data for branched PEI-SWNTs.	74
Table 2.4. Summary of PEI functionalized NCs properties.	88
Table 2.5. CO ₂ capacities of PEI-NCs compared to other amine tethered substrates.	88

List of Schemes

Introduction

- Scheme I.1.** Targeted delivery of paclitaxel from PEG hydrophilic carbon clusters. J. M. Berlin, T. T. Pham, D. Sano, K. A. Mohamedali, D. C. Marcano, J. N. Myers, and J. M. Tour, *ACS Nano*, 2011, **5**, 6643. 4
- Scheme I.2.** Binding mechanism of chromium to maghemite nanoparticles. J. Hu, G. Chen, and I. M. C. Lo, *Water Res.*, 2005, **39**, 4528. 6
- Scheme I.3.** CO₂ absorption mechanism of primary and secondary amines. 7

Chapter 1

- Scheme 1.1.** Reaction of PEI with fluorinated graphite intercalation compound (GIC). 32
- Scheme 1.2.** Synthesis of PEI-Phe(4-N-G) from Aza-Phe and exfoliated graphite. Phe is Boc protected at the alpha N. 35
- Scheme 1.3.** PEI addition to exfoliated GO in refluxing ethanol. 38

Chapter 2

- Scheme 2.1.** CO₂ capture mechanism of 1° and 2° amines. 66
- Scheme 2.2.** CO₂ absorption mechanism of 3° amines. 67
- Scheme 2.3.** Reaction of primary amines with CO₂ via carbamate formation. 73
- Scheme 2.4.** Tertiary amine CO₂ absorption mechanism. 82

Chapter 3

- Scheme 3.1.** Reaction mechanism for formation of PEI-SWNTs. 97

Introduction

Nanotechnology is a relatively new science that came to researchers attention due to developments in the fields of both chemistry and physics in the 1980s. The development of the scanning tunneling microscope (STM) by Binnig and Rohrer was awarded half of the Nobel prize in physics in 1986. The STM allowed researchers to image at a scale that was not previously possible, the atomic scale. The other half of the Nobel prize in 1986 went to Ruska for his work on the development of the scanning electron microscope (SEM) fifty years prior. Also in the 1980s, Curl, Kroto and Smalley discovered the fullerene at Rice University, for which they were awarded the Nobel prize in chemistry in 1996. Following on from these discoveries, an entirely new field of research has emerged, nanotechnology, with a further prize being received by Geim and Novoselov for their experiments involving graphene.

There are several different forms of carbon utilized in the field of nanotechnology, the base forms of these are, C_{60} , single walled carbon nanotubes, and graphene, Figure I.1.¹

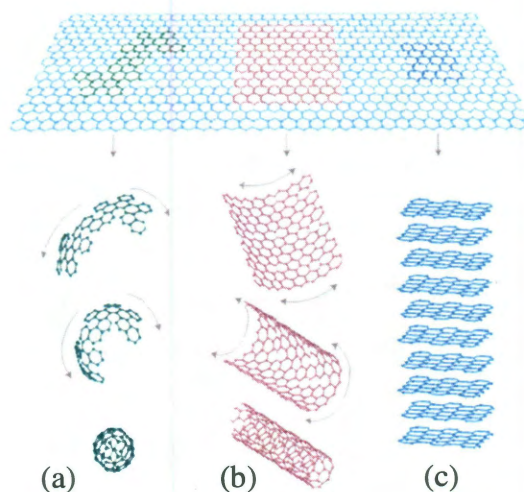


Figure I.1. Base forms for nano carbons, (a) C_{60} , (b) SWNT, and (c) graphene/graphite.

A. K. Geim and K. S. Novoselov, *Nat Mater*, 2007, **6**, 183.

As can be seen in Figure I.1, all of these carbon allotropes are derived from the same base structure, meaning they share many of the same properties. Many of these properties make nano-materials excellent candidates for the capture and/or release of a wide variety of materials. For any application involving capture of a material, one of the most important factors to consider is surface area. Due to their size, nano-materials have extremely high surface areas, making them ideal candidates for capture and release.

Similar to nano-carbons (NC), nano particles (NP) have been around long before our ability to image them. As with NC, nano particles have extremely high surface areas and many interesting properties, such as the ability to heat due to exposure to light. Properties such as these make NP ideal candidates for capture and release.

Drug delivery using nano-materials is a prevalent area of research in the scientific community, with a wide variety of targets, materials and methods of release. As we can see from Figure I.2 the rate of interest in the area has grown at an exponential rate in recent years.²

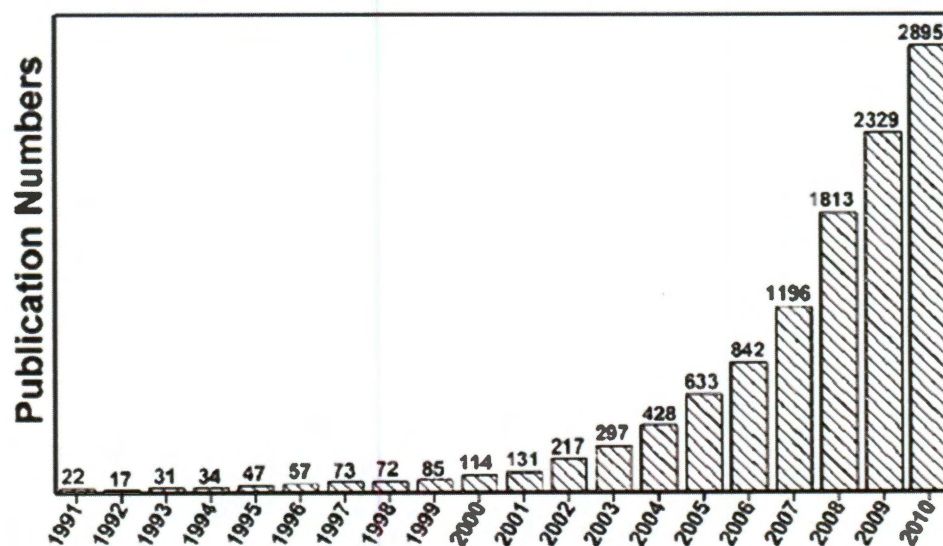


Figure I.2. Number of research papers on the use of nanomaterials as therapeutic agents in the last 20 years. X. Xue, F. Wang and X. Liu, *J. Mater. Chem.*, 2011, **21**, 13107.

One of the most cited papers in the area, from the Dai group in Stanford, involves the use of SWNTs as biological transporters of oligonucleotides.³ Furthermore, his group also showed the heating of SWNTs with NIR radiation caused localized heating of the SWNT, leading to cell death of cancerous cells *in vitro*. This localized heating is also the method for the unloading of the cargo of the SWNT, with short time pulses leading to release while longer exposure time results in cell death.

Further work from the Dai group involves the delivery, *in vivo*, of the cancer drug, paclitaxel.⁴ Using similar non-covalent modification with phospholipids (PL) as they did in their *in vitro* experiments, SWNTs were modified with PL-polyethylene glycol (PEG) terminated with a cleavable ester bond to paclitaxel (Figure I.3).⁴

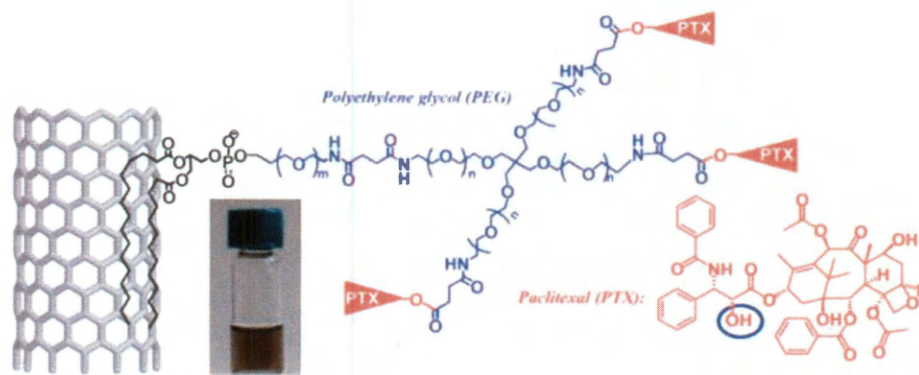
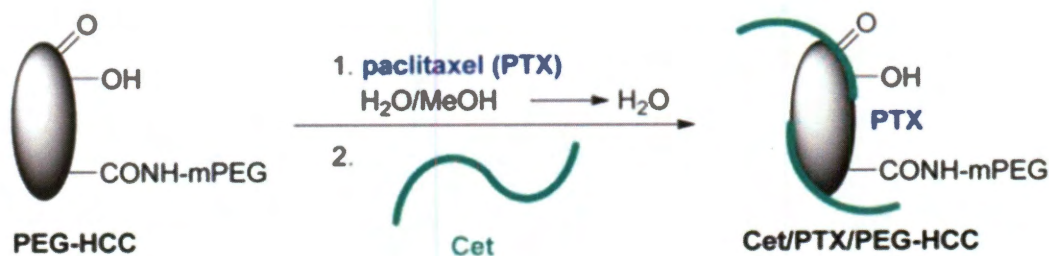


Figure I.3. Cartoon of the Dai method for the delivery of paclitaxel from pegylated SWNTs. Z. Liu, K. Chen, C. Davis, S. Sherlock, Q. Cao, X. Chen, and H. Dai, *Cancer Res.*, 2008, **68**, 6652.

This study, using mice, was the first reported use of SWNTs for delivery of a chemotherapeutic agent *in vivo*. Similar studies involved the changing of the nano substrate and drug to be released, resulting in PEG functionalized graphene-oxide (GO) loaded with doxorubicin, an anti cancer drug.⁵ This study also highlights an intrinsic

property of GO, its photoluminescence, allowing for live tracking of the delivery device *in vitro*.

The Tour group at Rice university have also developed vectors for the delivery of paclitaxel using nano-carbon materials.⁶ In contrast to the early work by Dai's group, the Tour system uses covalent modification of nano-carbons with PEG, instead of the hydrophobic conjugation deployed by Dai. This should allow for enhanced biological compatibility of the material *in vivo*. Furthermore, SWNTs are treated with oleum prior to functionalization with PEG. This results in "hydrophilic carbon clusters" that no longer retain the tubular properties of SWNTs due to defect formation by such a harsh oxidizing agent. Further work has shown that these HCCs can be further modified, non-covalently with the a targeting molecule for the targeted delivery of paclitaxel (Scheme I.1).⁷



Scheme I.1. Targeted delivery of paclitaxel from PEG hydrophilic carbon clusters. J. M. Berlin, T. T. Pham, D. Sano, K. A. Mohamedali, D. C. Marcano, J. N. Myers, and J. M. Tour, *ACS Nano*, 2011, **5**, 6643.

As well as nano-carbon materials, there are several other nano materials that are used for therapeutic purposes, metallic nanoparticles, polymeric nanoparticles, mesoporous silica, and nanoshells. Work on nanoshells for therapeutic purposes was pioneered by West and Halas, who formed gold nanoshells with tunable absorption properties.⁸ Particles can be tuned to absorb near infrared radiation at 820 nm, a region of the spectrum that is not absorbed by tissue. When absorbed by the NP, this radiation

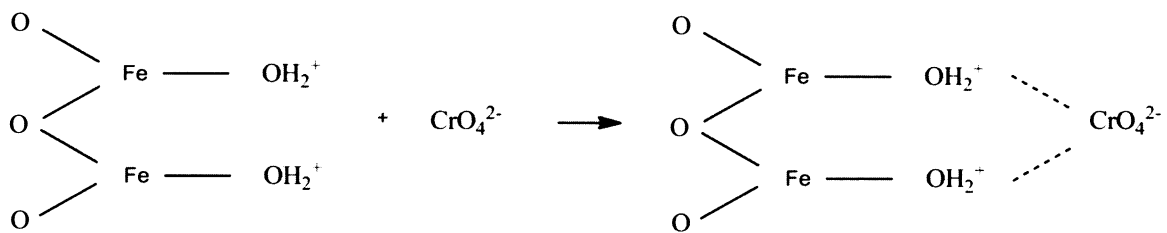
causes localized heating of the nanoshells resulting in the thermal destruction of cancer cells. Further work from West shows the ability of these nanospheres to release a variety of drugs, methylene blue, insulin and lysozyme, in a controlled fashion through a temperature sensitive hydrogel with imbedded nanoshells.⁹

Along with nanoshells, nanoparticles have a number of uses in the capture and release of materials. Similar to the nanoshells previously discussed, gold nanorods display similar optical properties for imaging and heating properties for the destruction of cancerous cells via thermal ablation.¹⁰ Silica nanoparticles with nanometer sized pores can be loaded with different carrier agents such as quantum dots (QD) and SWNTs, which can themselves be loaded with a variety of therapeutics. Furthermore, these particles have the ability to release their cargo over an extended period of time.¹¹

In addition to biological capture and release applications, nano materials can be used for the capture of a variety of hazardous materials. The purification of water is an area of large concern, due both to environmental and health risks. Several varieties of nano materials have been deployed for the removal of hazardous materials from water. There are many chemical processes that result in hazardous materials in waste water after the process is complete. There is always a danger of contamination from this water leaking into aquifers. For example, lead can be a contaminant in waste water from a number of chemical processes, such as, battery manufacture, painting, printing and dye factories.

Due to their high surface area and hollow interiors SWNTs make ideal candidates for the capture of lead. Wei and coworkers demonstrated the ability of SWNTs to absorb lead at high concentrations. when SWNTs are treated with nitric acid, the formation of oxygen containing species on the surface, hydroxyl, carboxyl and carbonyl, enhance the lead uptake ability of SWNTs.¹² Hexavalent chromium is another well known contaminant in waste water from metal processing plants. Iron oxide nanoparticles have been shown to have an excellent capture capacities of hexavalent chromium (Scheme

I.2), furthermore, these maghemite particles proved to be selective to hexavalent chromium. Tests with other ions such as, Na, Ca, Mg, Cu, NO, Cl, proved to have no effect on the uptake. The magnetic qualities of these particles allows for the separation of the metal loaded nanoparticles by simple magnetic separation.¹³

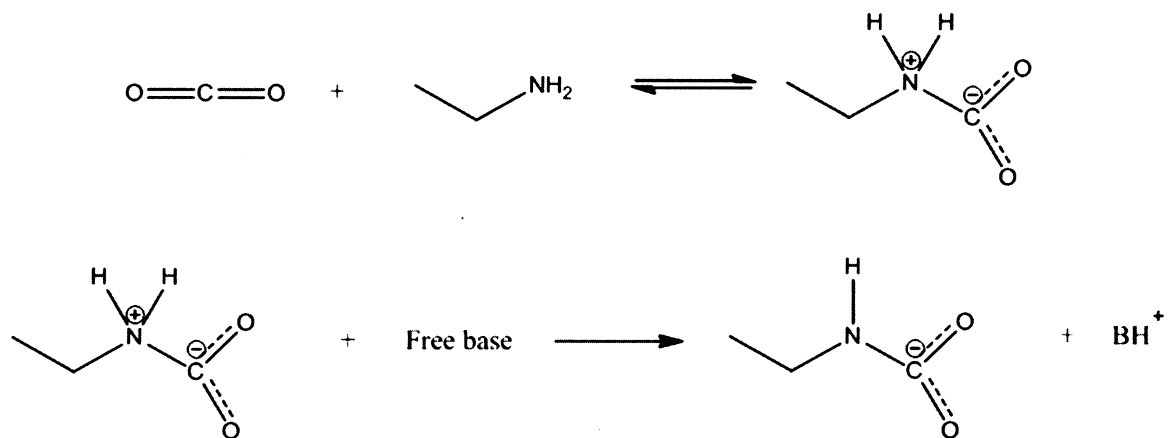


Scheme I.2. Binding mechanism of chromium to maghemite nanoparticles. J. Hu, G. Chen, and I. M. C. Lo, *Water Res.*, 2005, **39**, 4528.

Another environmental concern involves the capture of carbon dioxide (CO_2) from a variety of sources to help reduce emissions into the atmosphere. Work from the Barron lab has shown that polyethyleneimine functionalized single walled carbon nanotubes can absorb CO_2 with a higher gravimetric capacity than the polymer alone, once again taking advantage of the high surface area of nano carbons.¹⁴ The reaction of CO_2 with amines is shown in Scheme I.3. Further work on this topic will be discussed in detail in Chapter 2.

Mesoporous silica particles have been widely used for the same application. In this case, the high surface area comes from a nano-scale pore structure running throughout the particle, in contrast to SWNTs in which all of their surface area is on the exterior. Studies from Xu et. al. show how mesoporous silica can be modified with polyethyleneimine (PEI) and used as molecular sieves for the absorption of CO_2 .¹⁵ Using MCM-41 as the silica substrate, PEI was physisorbed onto the surface *via* reflux, and

studies showed that the capacity was 10 times that of MCM-41 alone and double the capacity of the polymer alone. Continuing along this line of research, Jones from Georgia Tech. demonstrates mesoporous silica particles, SBA-15, loaded with a variety of amines by physisorption and in situ polymerization, including PEI, can be used for CO₂ absorption.¹⁶



Scheme I.3. CO₂ absorption mechanism of primary and secondary amines.

Another area of interest for researchers is in the field of hydrogen storage. Due to the decline in the earth's supply of fossil fuels, researchers are interested in alternative fuel sources, including hydrogen. The idea for the storage of hydrogen using nano materials first came from Dillon *et. al.*, where they demonstrate the high hydrogen storage capacity of SWNTs.¹⁷ Furthering this research, the hydrogen capacity of graphite oxide has been explored.¹⁸ One of the problems with using organometallic materials for hydrogen storage is metal clustering. Using graphite oxide as a substrate, researchers have attached titanium atoms to the surface, allowing the capture of molecular hydrogen. This provides a high surface area substrate for absorption, while also eliminating the metal clustering problem by having the titanium anchored to the oxygen containing species on graphite oxide.

References

1. A. K. Geim and K. S. Novoselov, *Nat Mater*, 2007, **6**, 183.
2. X. Xue, F. Wang, and X. Liu, *J. Mater. Chem.*, 2011, **21**, 13107.
3. N. W. S. Kam, M. O'Connell, J. A. Wisdom, and H. Dai, *PNAS*, 2005, **102**, 11600.
4. Z. Liu, K. Chen, C. Davis, S. Sherlock, Q. Cao, X. Chen, and H. Dai, *Cancer Res.*, 2008, **68**, 6652.
5. X. Sun, Z. Liu, K. Welsher, J. Robinson, A. Goodwin, S. Zaric, and H. Dai, *Nano Res.*, 2008, **1**, 203.
6. J. M. Berlin, A. D. Leonard, T. T. Pham, D. Sano, D. C. Marcano, S. Yan, S. Fiorentino, Z. L. Milas, D. V. Kosynkin, B. K. Price, R. M. Lucente-Schultz, X. Wen, M. G. Raso, S. L. Craig, H. T. Tran, J. N. Myers, and J. M. Tour, *ACS Nano*, 2010, **4**, 4621.
7. J. M. Berlin, T. T. Pham, D. Sano, K. A. Mohamedali, D. C. Marcano, J. N. Myers, and J. M. Tour, *ACS Nano*, 2011, **5**, 6643.
8. L. R. Hirsch, R. J. Stafford, J. A. Bankson, S. R. Sershen, B. Rivera, R. E. Price, J. D. Hazle, N. J. Halas, and J. L. West, *PNAS*, 2003, **100**, 13549.
9. M. Bikram, A. M. Gobin, R. E. Whitmire, and J. L. West, *J. Controlled Release*, 2007, **123**, 219.
10. X. Huang, I. H. El-Sayed, W. Qian, and M. A. El-Sayed, *J. Am. Chem. Soc.*, 2006, **128**, 2115.
11. E. Tasciotti, L. Xuewu, R. Bhavane, K. Plant, A. D. Leonard, B. K. Price, M. M.-C. Cheng, P. Decuzzi, J. M. Tour, F. Robertson, and M. Ferrari, *Nat. Nanotechnol.*, 2008, **3**, 151.
12. Y.-H. Li, S. Wang, J. Wei, X. Zhang, C. Xu, Z. Luan, D. Wu, and B. Wei, *Chem. Phys. Lett.*, 2002, **357**, 263.

13. J. Hu, G. Chen, and I. M. C. Lo, *Water Res.*, 2005, **39**, 4528.
14. E. P. Dillon, C. A. Crouse, and A. R. Barron, *ACS Nano*, 2008, **2**, 156.
15. X. Xu, C. Song, J. M. Andrésen, B. G. Miller, and A. W. Scaroni, *Microporous Mesoporous Mater.*, 2003, **62**, 29.
16. J. C. Hicks, J. H. Drese, D. J. Fauth, M. L. Gray, G. Qi, and C. W. Jones, *J. Am. Chem. Soc.*, 2008, **130**, 2902.
17. A. C. Dillon, K. M. Jones, T. A. Bekkedahl, C. H. Kiang, D. S. Bethune, and M. J. Heben, *Nature*, 1997, **386**, 377.
18. L. Wang, K. Lee, Y.-Y. Sun, M. Lucking, Z. Chen, J. J. Zhao, and S. B. Zhang, *ACS Nano*, 2009, **3**, 2995.

Chapter 1

Synthesis and Characterization of Polyethylenimine Nano Carbons

Introduction

Carbon Nanotubes. Single walled carbon nanotubes (SWNTs) have a variety of remarkable properties, ranging from electrical conductivity to tensile strength. However, the extreme hydrophobic nature and bundling tendencies make SWNTs difficult to work with. In order to overcome these issues a wide range of chemical modifications such as wrapping, dispersion in super acids, use of non-polar solvents, and covalent functionalization have been utilized. Figure 1.1 illustrates these different methods and subsequent reactions that can be performed.

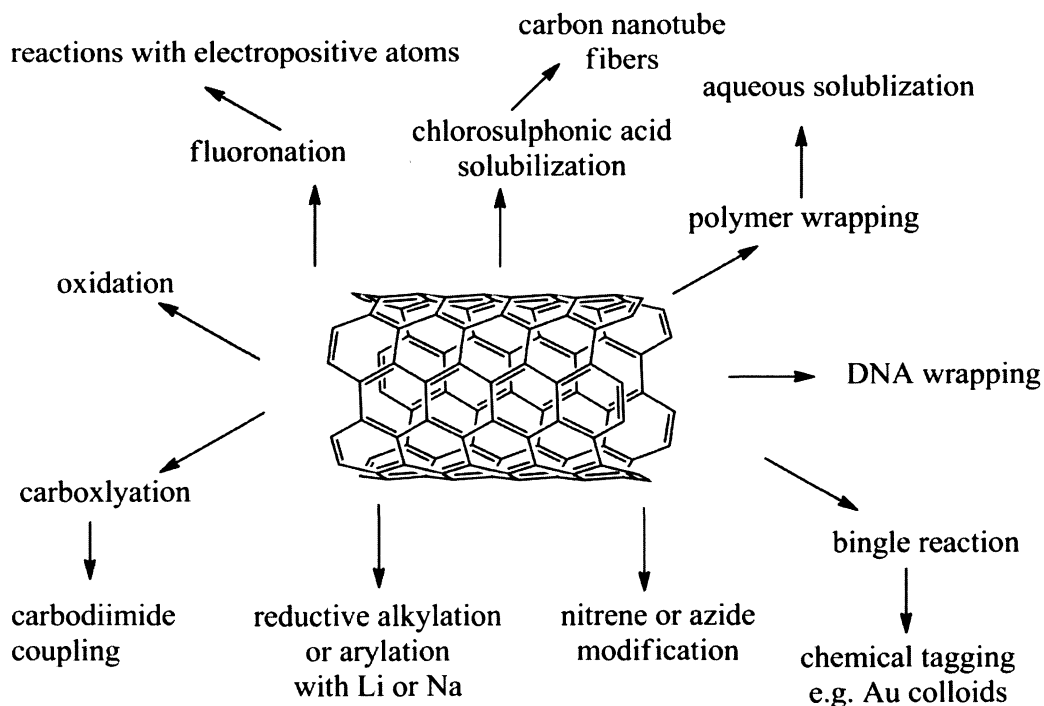


Figure 1.1. Various methods for the modification of single and multi-walled carbon nanotubes.

Due to the hydrophobic nature of carbon nanotubes (CNT) they are not fully soluble in common laboratory solvents. The best solvent for the full solubilization of SWNTs has been shown to be chlorosulphonic acid.¹ Spinning of nanotubes from chlorosulphonic acid has resulted in long fibers with high electrical conductivity.

Polymer and DNA wrapping of SWNTs are non-covalent chemical modifications that allow for the use of SWNTs in biological applications.,^{2, 3} Several studies have been carried out that show the uptake of SWNTs into a wide variety of cells via an initial polymer wrapping. Polymer wrapping, rather than covalent functionalization, is an interesting method for using SWNTs in biological applications. When SWNTs are covalently modified they lose many of their novel properties due to the formation of sp^3 hybridized carbon. A widely used technique for tracking carbon nanotubes inside a cellular matrix is fluorescence,⁴ which is a property of semi-conducting SWNTs that is lost with covalent modification. Polymer wrapping has also been used a method for the solubilization of SWNTs in aqueous media and buffers.³ DNA wrapped SWNTs have been proposed as sensors for hydrogen peroxide and glucose. Double stranded DNA will wrap around SWNTs when sonication is employed, with small segments (100 - 300 base pairs) of DNA interacting with the SWNT. By monitoring near infra-red optical changes in the DNA-SWNT hybrid the authors were able to measure changes in concentration of hydrogen peroxide and glucose.⁵

Chemical functionalization of CNT provides another route to solubility in a variety of organic solvents. Carboxylation of SWNTs allows for further modification with a wide variety of functional moieties.⁶ Dicyclohexylcarbodiimide (DCC) or diisopropylcarbodiimide (DIC) can then be used to couple functional groups, such as amines, onto the surface of the SWNTs.⁷ Reductive alkylation and arylation with Li or Na salts allows for the attachment of long chains terminated with hydrophilic or hydrophobic moieties depending on the requirements of the application.⁸ SWNTs can also be highly functionalized using diazonium salts.⁹ Several different moieties can be

deployed on the phenyl substituent: carboxylic acid, halides, NO₂, and *tert*-butyl. This results in highly functionalized SWNTs that are soluble in a wide variety of solvents.

Other methods for a high degree of functionalization of SWNTs include reactions with nitrenes¹⁰ and carbenes.¹¹ The modification of SWNTs with oxycarbonyl nitrenes results in highly functionalized SWNTs and can include a variety of functional moieties, including alkyl chains, aromatic groups, dendrimers and crown ethers. Similar to the diazonium functionalization, nitrene functionalization leads to highly functionalized SWNTs that are more readily soluble in organic or aqueous solution depending on the R group.

Other methods of chemically modifying CNTs include treatments with aggressive acids. Oxidation of SWNTs using piranha, a highly oxidizing acid, is a method that results in the cutting of SWNTs to different lengths depending on the temperature of the solution and the reaction time.^{12, 13} The oxidation results in the addition of several different oxygen containing groups such as carboxyls, hydroxyls and epoxides. As previously mentioned, carboxyl and hydroxyl groups can be further modified using DCC and DIC coupling techniques. However, no backside attack can occur on the epoxide groups in the case of SWNTs due to the closed nature of the SWNT. This is not the case for graphite as will be discussed later. Along with piranha, another acid that can be used to cut SWNTs is oleum. This cutting procedure results in ultra-short SWNTs,¹⁴ or hydrophilic carbon clusters as they later became known⁷ due to the fact that there was no tubular structure remaining after treatment in such harsh oxidizing conditions.

Fluorination of SWNTs has widely been used as a method for the sidewall modification of SWNTs.¹⁵ When SWNTs are fluorinated, the fluorination usually occurs in bands in the 1,2 or 1,4 positions along the surface of the sidewall.¹⁶ The fluorination allows for further modification of the SWNTs by activating the neighboring carbon atom for nucleophilic attack with amines or other nucleophiles. Covalent functionalization of F-SWNTs with amines, such as polyethyleneimine (PEI), has been achieved by first

fluorinating the SWNTs and reacting them with PEI in the presence of pyridine.¹⁷ In addition to covalent functionalization, fluorination followed by subsequent pyrolysis can also result in cut SWNTs that are as little as 60 nm long, depending on the temperature and time of fluorination.¹⁸ There are various other nanocarbons that have similar properties and reactions pathways as SWNTs but are significantly less expensive commercially. For these reasons other nanocarbons have been explored for applications similar to those of SWNTs.

Graphite/graphene. Graphene has many of the same properties that occur in SWNTs, such as, high electrical conductivity and tensile strength. This is to be expected as their structures are quite similar, the only difference being the cylindrical nature of SWNTs versus the planar structure of graphene. This difference, the curvature of the SWNT sidewalls versus the flat plane of graphene, creates strain in the SWNT and encourages reactions on the sidewalls to alleviate the strain. Being so chemically similar, it follows that both nanocarbons have the same solubility issues. Further modification of graphite is required for solubilization into common laboratory solvents. Several of the modification methods are shown in Figure 1.2.

Graphite can be made water soluble via conversion to graphite oxide (GO). There are several different methods for this conversion, the most well known being the Hummers method.¹⁹ The degree of oxidation can be controlled by the method used, the graphite source, and by varying the reaction conditions.²⁰ GO has a variety of functional moieties: carboxylic acid, hydroxyl and epoxide group. Each of these functional groups provides a convenient handle for further chemical modification of GO. The attachment of amines to graphite oxide via nucleophilic reaction of the amines with the epoxy groups present on GO has previously been shown.²¹ While GO provides a very reactive material, the framework responsible for the unique properties of graphene is destroyed in the

process. However, dispersions of graphene have been achieved through simple sonication and homogenization of graphite in ODCB and subsequent centrifugation.²²

Similar to SWNTs, exfoliated graphite has been covalently modified through both nitrene chemistry and radical additions resulting in high density functionalization. The attachment of azido phenylalanine to exfoliated micro-crystalline graphite via the decomposition of the azido group to a nitrene and subsequent attachment to graphite has been demonstrated.²³

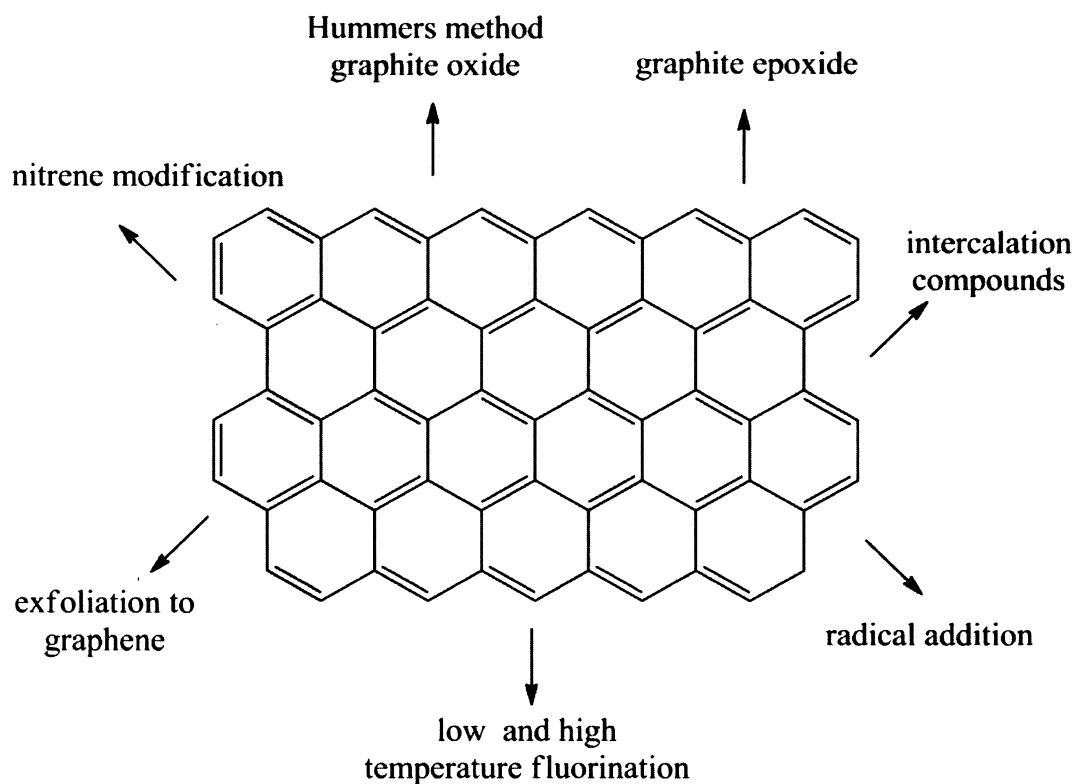


Figure 1.2. Various methods for the modification of graphitic materials.

Radical addition of perfluorinated alkyl iodides has been achieved on both SWNTs and graphene. Radical generation can come from two different sources, thermolysis and UV photolysis. The resulting compounds show improved solubility in

chloroform while having similar to properties to a wide variety of hydrophobic materials that are commercially viable due to their extreme hydrophobic nature, such as GoreTex.²⁴

Another method of producing reactive graphene is fluorination which can be used to produce a wide variety of graphite fluoride compounds. Depending on the temperature of fluorination, two kinds of fluorine-graphite compounds can be formed. High temperature fluorination ($> 400\text{ }^{\circ}\text{C}$) results in the formation of graphite fluoride $[\text{CF}_x$ or $(\text{CF})_x]$.²⁵ Low temperature fluorination of graphite can result in graphite intercalation compounds (GICs), where HF_2^- molecules work their way between the layers of graphite expanding the spacing between layers.²⁶ These compounds can have a variety of applications including their potential use as battery cathodes.²⁷

Fullerenes (C_{60}). Fullerenes are another variety of nanocarbons that have the possibility to be used in a variety of applications from biological applications to applications requiring high surface area materials. Figure 1.3 shows some of the different methods of modification that can be applied to fullerenes.

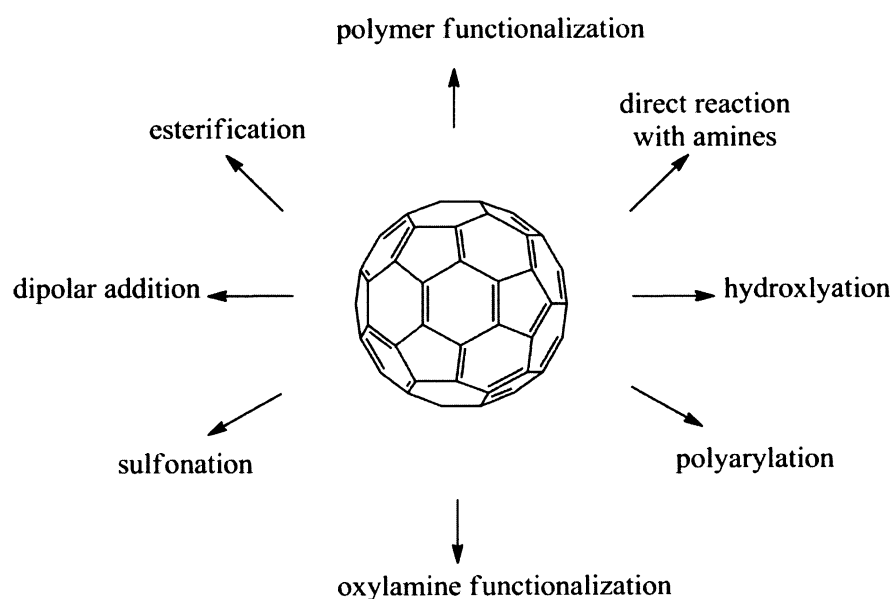


Figure 1.3. Reaction pathways for the chemical modification of fullerenes.

Unlike SWNTs or graphite, fullerenes are soluble in toluene and some other solvents due to their nanometer scale. Furthermore, they are more reactive than SWNTs and graphite due to their extreme curvature. Similar to SWNTs but to a larger degree, the curvature of fullerenes leads to a large degree of strain within the molecule. For example, fullerenes will react directly with nucleophilic atoms such as primary amines.²⁸ This is in contrast to amine reactions with SWNTs or graphite which require the use of fluorination or other modification to generate reactive materials.

Due to their size and shape, fullerenes have the potential to be useful in a wide variety of biological applications. However, because of their hydrophobic nature their use in these applications is limited. Several methods have been developed to attach a wide variety of hydrophilic moieties to allow for aqueous solubility of fullerenes. The first chemically modified fullerenes for use in biological studies were carboxylic acid functionalized, which led to the discovery of some of the biological applications that were previously postulated, such as the ability to inhibit HIV protease.²⁹ Several groups have utilized amino acid functionalization of fullerenes to impart biocompatibility to C₆₀. Prato and Barron used dipolar additions of azomethine ylides,³⁰ dienes and azido-amino acids to the cage of C₆₀ to form fullerene amino acids.³¹

While the unique size, shape and hydrophobicity of C₆₀ give it the ability to interact with biological superstructures, the non-biological applications of functionalized fullerenes are even more promising. Polyarylated fullerenes have a variety of applications when used in mixtures with poly-hydroxylated fullerenes and poly-aminated fullerenes. Applications include photoresists for extreme UV lithography, proton conductors for fuel cells, organic photovoltaic cells and optical limiting materials. In general, the production of polyarylated fullerenes is an expensive process due to the cost of the reagents. The process can be simplified by using a FeCl₃ catalyst to produce penta-aryl(chloro)fullerene.³²

Fisher esterification can be utilized for the controlled addition of substituents to fullerenes, which can eliminate some of the problems associated with fullerene modification, such as the need for purification due to the formation of multiple-addition adducts. This can then be further modified by click chemistry for the attachment of a variety of azide terminated molecules, such as, azido-poly(caprolactone).³³ Several other modification methods have been developed, such as the use to nitronium chemistry to attach a wide variety of hydrophilic moieties including hydroxyl and carboxylic esters.

As previously mentioned, fullerenes are able to react directly with primary amines, this method has been used to attach amino acids and polymers directly to C₆₀.²⁸

The modification of fullerenes with polystyrene and further incorporation into a block copolymer with poly(ethylene oxide) results in improved lamellar structure of the self-assembled structure.³⁴ Due to their hydrophobic nature, fullerenes can exhibit self-assembly characteristics when attached to hydrophilic chains. These amphiphilic structures have the ability to form micelles and reverse micelles in solution depending on the solvent used.

In the current work, a wide variety of functionalization methods have been used to functionalize SWNTs, MWNTs, a variety of graphitic compounds and fullerenes with polyethyleneimine, for aqueous solubility and possible biological applications. The choice of PEI was made due its previous use as a cellular transfection agent. Furthermore, the amine functionality allows for simple chemistry using fluorinated SWNTs, providing a template for future work involving any amine terminated polymer. The degree of functionalization will be determined using a variety of techniques including Raman spectroscopy, thermogravimetric analysis (TGA), scanning electron spectroscopy (SEM) atomic force microscopy (AFM) and X-ray photoelectron spectroscopy (XPS). The carbon dioxide absorptive properties of the materials will be further characterized in Chapter 2.

Results and Discussion

PEI-SWNTs. Ultimately, we intend to compare the PEI functionalization of various nanocarbons, including SWNTs, MWNTs, graphitic compounds, and fullerenes; however, our initial and most in-depth analysis is on the PEI-SWNT materials. PEI-SWNTs were prepared by the reaction of F-SWNTs with various molecular weights (M_w) of PEI as suspension in ethanol (EtOH) with a pyridine catalyst (see Experimental). PEI-SWNTs were prepared using branched PEI of $M_w = 600, 1800, 10000,$ and 25000 Da and linear PEI ($M_w = 25000$ Da), yielding PEI(600)-SWNT, PEI(1800)-SWNT, PEI(10000)-SWNT, PEI(25000)-SWNT and linear-PEI, respectively. We investigated their solubility, confirmed covalent attachment of PEI to the nanotube, and determined the degree of functionalization.

Although the reaction of F-SWNTs with amines in the presence of a catalyst results in covalent attachment by NMR measurements, we initially prepared the non-covalent, or wrapped, conjugates using both pristine SWNTs and F-SWNTs wrapped with PEI ($M_w = 600$ Da) to determine their stability in an aqueous environment for comparison to covalent examples. The wrapped conjugates, PEI(600)/SWNT and PEI(600)/F-SWNTs are prepared in the same manner as the covalent examples but without the pyridine catalyst. Both non-covalent conjugates are soluble in water upon preparation; however, aqueous dialysis for 20 minutes results in the aggregation and precipitation of the nanotubes. In contrast, no precipitation is observed in each of the PEI-SWNTs prepared in the presence of a pyridine catalyst after four days of dialysis. The comparison between covalent and non-covalent attachment after dialysis is shown in Figure 1.4.

The aqueous solubility of the PEI-SWNTs was evaluated at neutral pH. For example, PEI(600)-SWNTs were sonicated for 15 minutes in de-ionized water and then were transferred to a centrifuge tube. The solution was centrifuged to remove all of the bundled tubes and insoluble material from the decant. The resulting decant was deep

black in color with no visible particulates in the solution. The solubility was determined to $0.4 \text{ mg}\cdot\text{mL}^{-1}$.

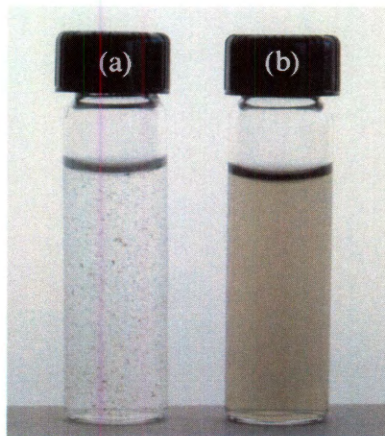


Figure 1.4. Comparison of (a) non-covalently attached PEI(600)/SWNTs, and (b) covalently attached PEI(600)-SWNTs after aqueous dialysis for 20 minutes and 4 days, respectively.

Qualitatively, each of the branched PEI-SWNTs showed comparable solubility at neutral pH, suggesting that even at the lowest molecular weight the branched PEI allowed solubilization of the SWNT. In contrast, linear-PEI-SWNT shows only transient solubility in water. After sonication, a solution is observed for only a few minutes before aggregation and precipitation occur.

In addition to the neutral solutions, the branched PEI-SWNT's showed good solubility between the pH ranges 1.7 to 8.31. At a pH above 8.5 aggregation was observed; however, the rate of aggregation was dependent on the base source. Raising the pH with a NaOH solution resulted in aggregation over a period of about 6 hours. In contrast, addition of NaHCO_3 solution to the PEI-SWNT solution resulted in instantaneous aggregation, compared at the same pH. This observation is consistent with

the CO₂ absorbing qualities of the PEI-SWNT's, which will be discussed in detail in Chapter 2.

As expected, based upon the known reaction of F-SWNTs with amines and a catalyst, the X-ray photoelectron spectroscopy (XPS) spectra indicates a decrease in the fluorine concentration for the PEI-SWNTs versus the F-SWNT starting material with a concurrent increase in the nitrogen content (Figure 1.5).

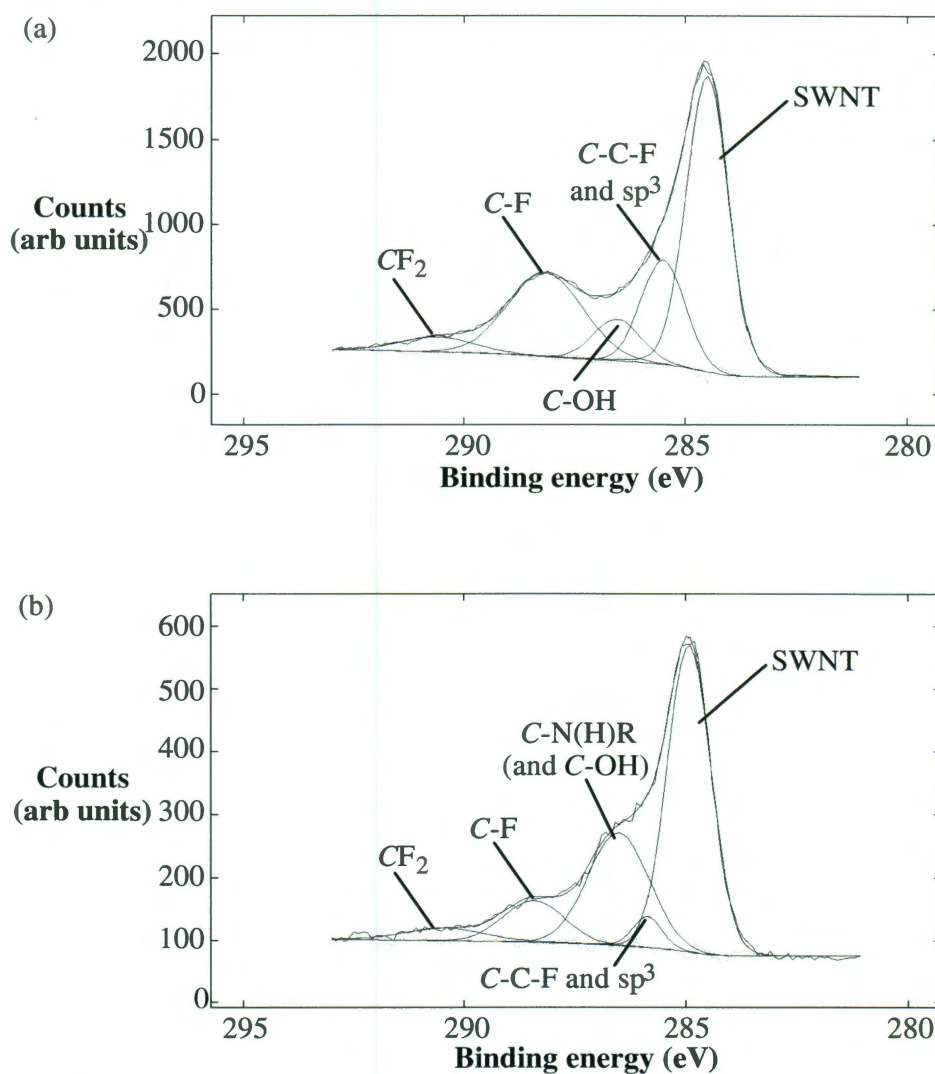


Figure 1.5. C_{1s} high-resolution XPS spectra for (a) F-SWNTs and (b) PEI(10000)-SWNTs. Peak fits and assignments are shown.

The reaction of F-SWNTs with simple amines has been shown to result in a loss of the majority of fluorine; however, the C_{1s} spectrum shows that there remains significant fluorine concentration. Another interesting observation is that the signal due to the CF_2 groups (290.62 eV) appear to be largely unaffected by the reaction of the amine, (Figure 1.5b), while the peak assigned to the sidewall C-F groups (288.61 eV) is diminished concurrently with the increase of the sidewall C-N substituents (286.35 eV). This observation suggests that the reaction of F-SWNTs with amines occurs preferentially at the sidewall C-F groups rather than the defect CF_2 moieties.

In order to evaluate the degree of functionalization the PEI: SWNT ratio was determined, with the thermogravimetric analysis (TGA), to be ~ 59 % PEI. TGA analysis of as prepared PEI-SWNTs shows a mass loss between 25 and 75 °C, consistent with desorption of water (and possibly CO_2 , see Chapter 2). The decomposition of the PEI substituents and the reformation of the parent SWNT occurs between 275 - 325 °C. As may be expected, the number of polymer molecules per SWNT carbon is larger for low molecular weight PEI ($M_w = 600$ Da) than for high molecular weight PEI ($M_w = 25,000$ Da). However, it is worth observing that above 10000 Da, the number of polymer molecules per SWNT carbon remains essentially constant (Figure 1.6).

The Raman spectrum, obtained with a 780 nm excitation laser, for the purified HiPco SWNTs (Figure 1.7a) displayed a strong tangential G mode at 1592 cm^{-1} accompanied by a small peak at 1292 cm^{-1} , corresponding to the D (disorder) mode due to sp^3 -hybridized carbons, suggesting a low degree of defect sites within the continuous graphitic sheet of the nanotubes. The presence of prominent radial breathing modes appearing at 233 and 267 cm^{-1} suggests that the nanotubes are truly single walls. Fluorination of the purified SWNTs resulted in a substantial increase in the number sp^3 -hybridized carbons with a concurrent increase in the D mode, and a decrease in the tangential G mode associated with sp^2 -hybridized carbons from the graphitic sidewalls (Figure 1.7b).

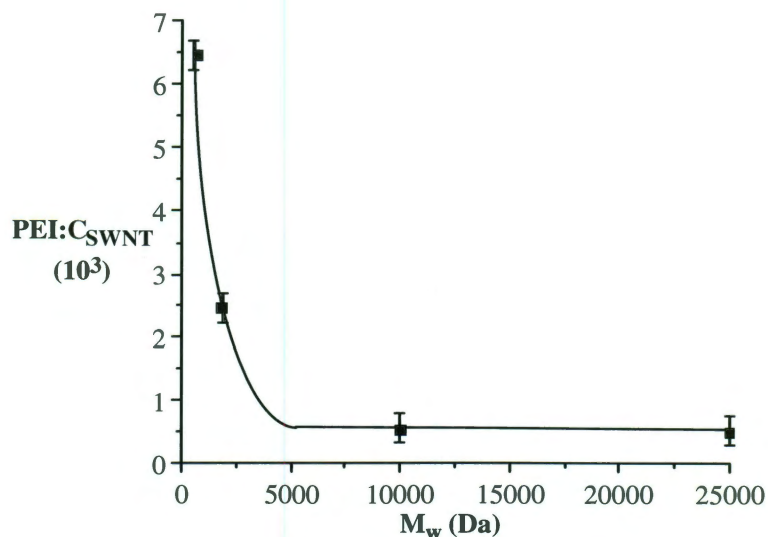


Figure 1.6. Plot of the number of PEI molecules per SWNT carbon ($\text{PEI:C}_{\text{SWNT}}$) as a function of the molecular weight (Da).

This increase in the ratio of the $\text{sp}^3:\text{sp}^2$ ratio is described by the D:G ratio. An increase in the D:G ratio is also accompanied by an almost complete loss of the radial breathing modes, suggesting that the continuous delocalization of electrons throughout the nanotubes has been highly disrupted due to covalent attachment of the fluorine atoms to the nanotubes.

As was observed in the covalent addition of diamines to the sidewalls of F-SWNTs the structural integrity of the original purified nanotubes is partially re-established by the addition of PEI to the F-SWNTs under the reaction conditions previously described. The sp^3/sp^2 ratio mode present in the PEI-SWNT spectra (e.g., Figure 1.7c) is substantially lower than that observed for the F-SWNTs, however, higher than the observed ratio for purified SWNTs without functionalization. The presence of radial breathing modes and an increase in the tangential mode suggest that portions of the original graphitic sidewall have been re-established during the reaction process. This result, accompanied by an increase in the nitrogen content of the sample and a decrease in the fluorine content as confirmed through XPS, suggests that the PEI has been covalently

attached to the sidewalls resulting in the displacement of the fluorine atoms. Table 1.1 gives an overview of physical and spectroscopic data for different molecular weight PEI-SWNTs.

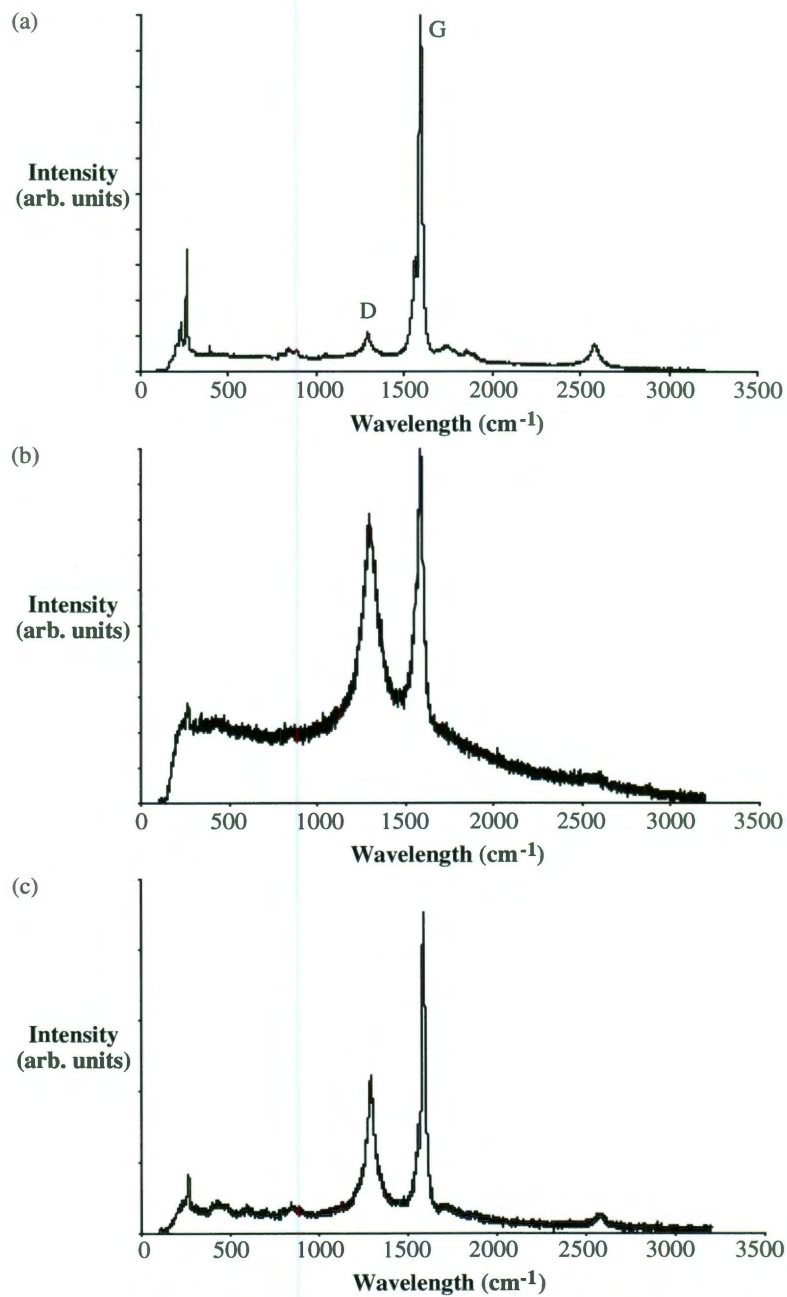
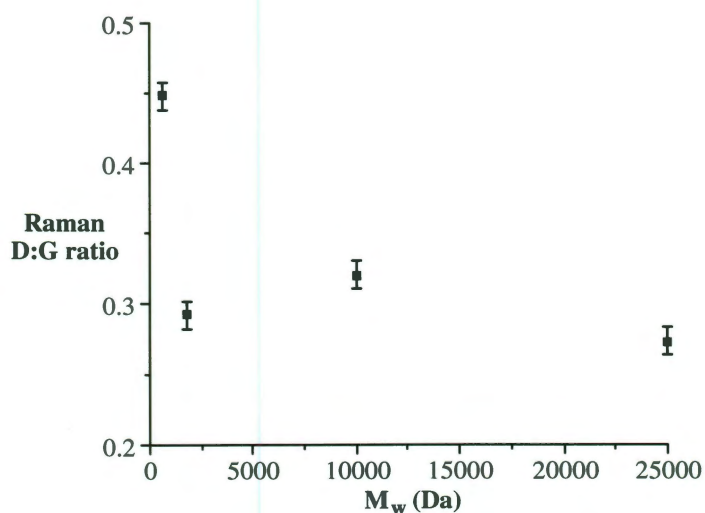


Figure 1.7. Raman spectrum (780 nm) of (a) purified SWNTs, (b) F-SWNTs, and (c) PEI-SWNTs.

Table 1.1. Selected physical and spectroscopic data for branched PEI-SWNTs.

PEI M_w (Da.)	PEI:C _{SWNT}	Raman D:G
600	1:155	0.448
1,800	1:405	0.219
10,000	1:1910	0.280
25,000	1:2065	0.273

If our model for the morphology of the PEI substituents as a function of molecular weight is correct then the number of “attachment” points (i.e., the number of sp^3 carbon per SWNT) should follow the same trend as number of PEI molecules per SWNT carbon. As may be seen from Figure 1.7, the number of sidewall sp^3 carbons is greater (i.e., large D:G ratio) for PEI with a $M_w = 600$ Da, than those with higher molecular weights. However, there appears to be no significant variation in the D:G ratio for PEI above $M_w = 1800$ Da (Figure 1.8). This is consistent with our model shown in Figure 1.9.

**Figure 1.8.** Plot of the Raman D:G ratio as a function of PEI molecular weight (Da) for PEI-SWNTs.

It may be assumed that increasing the molecular weight of the PEI allows for more attachment points via the additional NH_2 groups, and as a consequence a smaller number of PEI molecules would be required to functionalize the entire SWNT. Instead, a large increase in the molecular weight would be required to functionalize the entire SWNT. Instead, a large increase in the molecular weight (i.e., 10000 versus 25000) does not correspond to a large change in the number of PEI polymer molecules per SWNT carbon. We propose that this is due to the hydrophilic PEI being repelled away from the hydrophobic surface of the SWNT (Figure 1.9a and b) rather than wrapping around the SWNT to make additional covalent attachments (Figure 1.9c). The surface globular nature of the PEI substituents is confirmed by AFM and TEM, while the extent of functionalization is consistent with Raman spectroscopy.

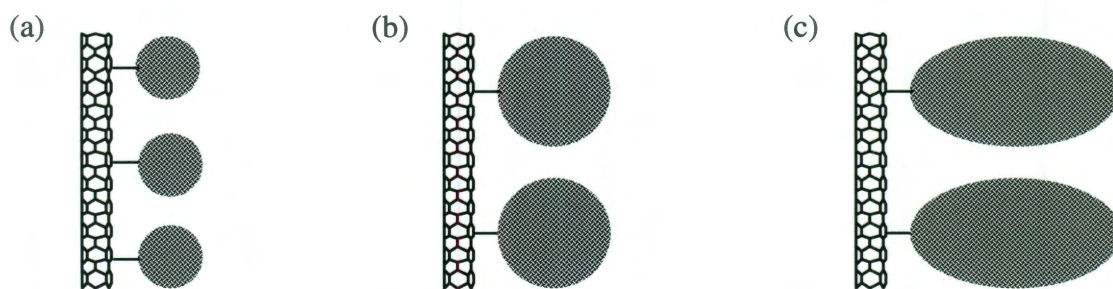


Figure 1.9. Schematic representation of PEI-SWNTs with molecular weights of (a) 600 Da, (b) 10000 Da, and (c) 25000 Da, showing the orientation of PEI which represents the results of Table 1.1, indicating why there is no substantial increase PEI:SWNT above 10,000 Da.

The UV-vis spectra (Figure 1.10) obtained for the PEI-SWNTs assists in confirming the covalent functionalization of the SWNTs through the loss in the van Hove absorbance as compared to un-functionalized SWNTs, respectively. This is due to the partial disruption in the delocalized electronic structure of the SWNTs due to the sp^3 -hybridized carbons present in the sidewall at the sites of covalent attachment to the PEI.

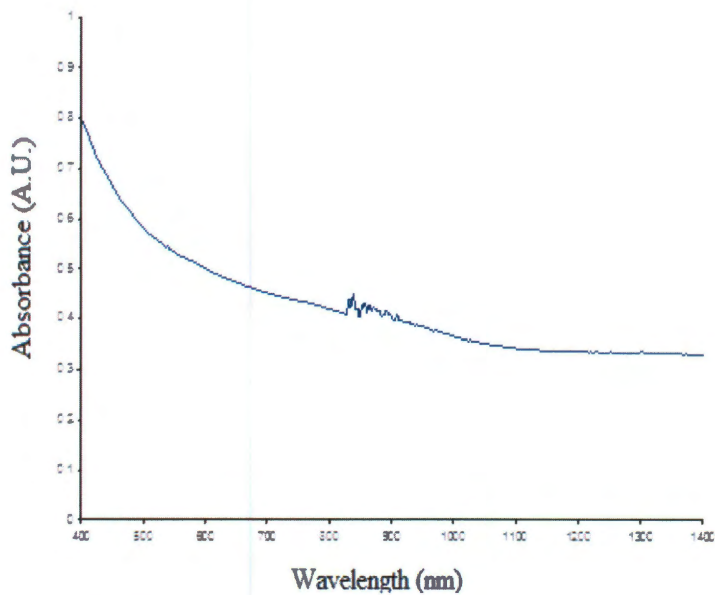


Figure 1.10. UV-Vis spectrum of PEI(600)-SWNTs.

Atomic force microscopy (AFM) and transmission electron microscopy (TEM) also confirmed the presence of PEI on the sidewalls of the tubes. Figure 1.11 shows PEI(10000)-SWNTs spin-coated on a freshly cleaved mica surface.

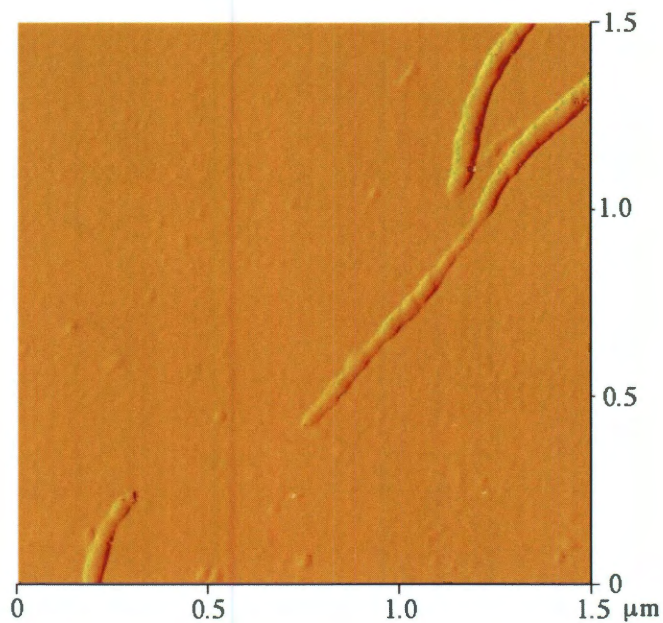


Figure 1.11. AFM image of a PEI(600)-SWNT showing the presence of PEI “globules”.

The images are typical of substituted SWNTs, and analysis of the height data along the length of the nanotubes suggests that the majority of the tubes are coated with the polymer when compared to the height data of unfunctionalized tubes. Cross sectional analysis of the data in Figure 1.11 shows a height of 7 – 10 nm compared to 2 – 5 nm for a pristine SWNT.

Figure 1.12a displays a TEM image of a single PEI(600)-SWNT protruding from a bundle of tubes. Bundling of the tubes occurs when the sample is drop-cast onto the TEM grid and the water from which the sample is contained slowly evaporates causing concentration of the solution and subsequent aggregation and bundling of the tubes.

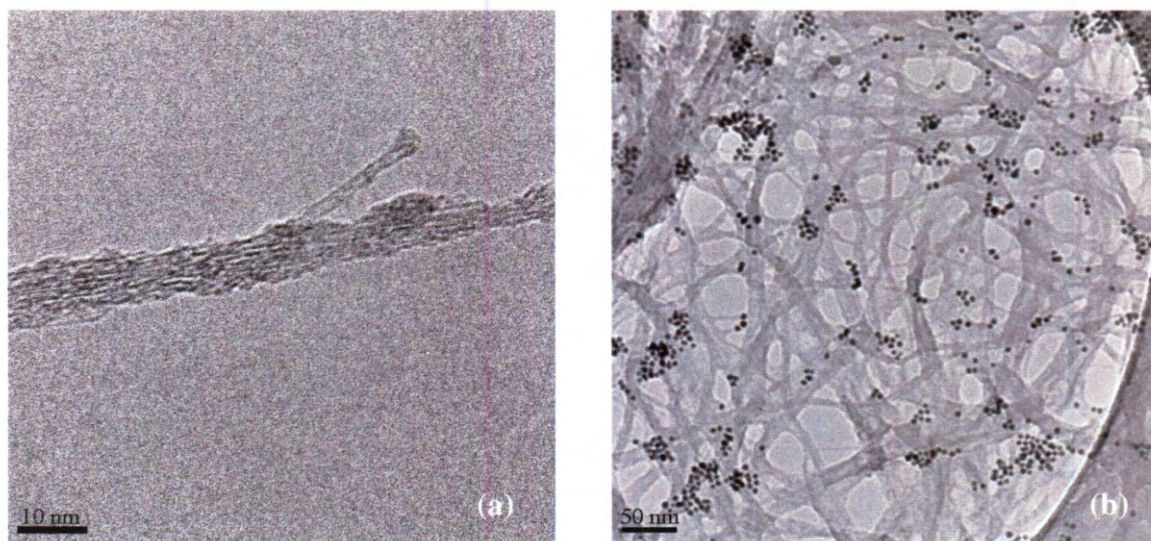


Figure 1.12. TEM images of (a) a single PEI(600)-SWNTs exposed from a bundle and (b) PEI(600)-SWNTs functionalized with gold nanoparticles formed from the reduction of HAuCl_4 by the PEI substituents.

Due to the organic nature of PEI it was difficult to obtain images of the polymer on the SWNTs with TEM as it would combust when exposed to the electron beam. It has been previously reported that linear-PEI can be used as a reducing agent in the formation of gold nanoparticles from HAuCl_4 . Extending this prior work with linear-PEI the

presence of branched-PEI on the SWNTs was indirectly confirmed by the addition of HAuCl_4 to the PEI-SWNT solution and heating the solution for 20 minutes at 70 °C. Upon completion of heating, the samples were allowed to cool and were drop-cast onto TEM grids and re-imaged. The presence of gold nanoparticles along the sidewalls of tubes (Figure 1.12b) and not in the void space demonstrates the presence of PEI on the sidewalls of the SWNTs.

Given that our efforts to functionalize SWNTs with PEI were successful, we wanted to explore other more cost-effective nanocarbons and compare their reactivities to that of SWNTs. We began our investigation with MWNTs as they have a similar surface area and reactivity to SWNTs and are significantly less expensive.

PEI-MWNT. PEI-MWNTs we prepared using the same synthesis procedure used for the PEI-SWNT's, fluorination of the nanocarbon substrate. The Raman spectra of raw MWNT's and PEI-MWNT's are shown in Figure 1.13. As can be seen from the Raman spectra, the D:G ratio actually decreases after the functionalization process, which is the opposite effect as that seen when SWNT's are modified by the same method. We speculate that the fluorination process actually "cleans" the raw MWNT's via the removal by pyrolysis of small amounts of amorphous carbon that are present in the crude raw MWNT sample. Similar to the way nanotubes can be cut via fluorination and subsequent pyrolysis.

From the Raman spectra it may appear that no reaction occurred, due to the decrease in the D:G ratio. However XPS studies indicate the presence of nitrogen, which was not present in the raw MWNT XPS spectrum. Furthermore, the presence of the C-N at 286.5 eV indicates the covalent functionalization of MWNTs with PEI (Figure 1.14).

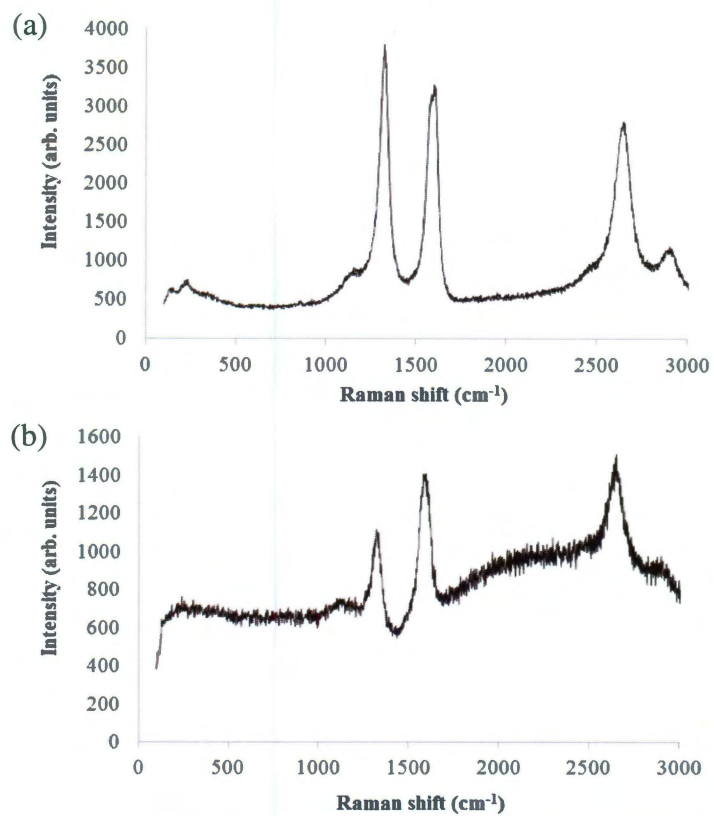


Figure 1.13. Raman spectra of (a) Bay-MWNTs and (b) PEI-MWNTs.

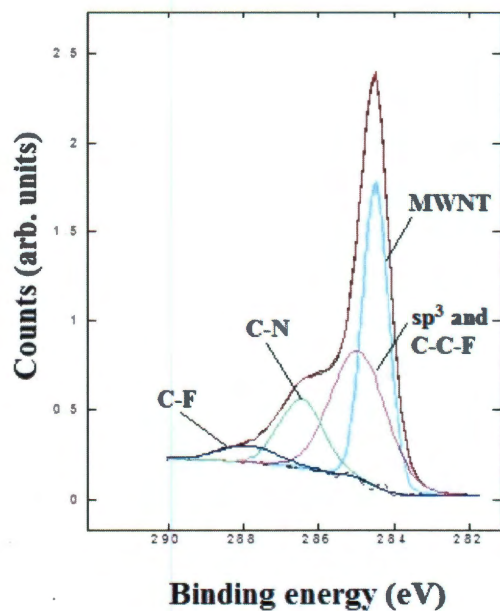


Figure 1.14. C1s spectrum of PEI-MWNT showing the presence of C-N bonding at 286.5 eV.

To visualize the surface coverage of the polymer coating, two microscopic techniques were utilized; AFM and SEM. AFM analysis allows the visualization of what the solution state structure may look like while SEM is a dry technique, with solid PEI-MWNT powder deposited on SEM stub followed by gold coating prior to imaging. AFM analysis of PEI-MWNTs (Figure 1.15 and 1.16) shows the polymer coating in patches on the MWNT, an observation also noticed in SWNTs due to the fluorination occurring in bands. Samples were prepared by spin coating from aqueous solution onto a cleaved mica substrate.

SEM analysis of the PEI-MWNTs (Figure 1.17) shows what looks like large globular aggregated structures. Closer analysis reveals that each large aggregate is composed of bundled PEI-MWNTs (Figure 1.18), which is expected if the sidewall functionalization does not cover the entire nanotube. The SEM micrographs support our observation by AFM, that the polymer is not entirely covering the tube. Sample was prepared by powder deposition of PEI-MWNTs onto SEM carbon tape.

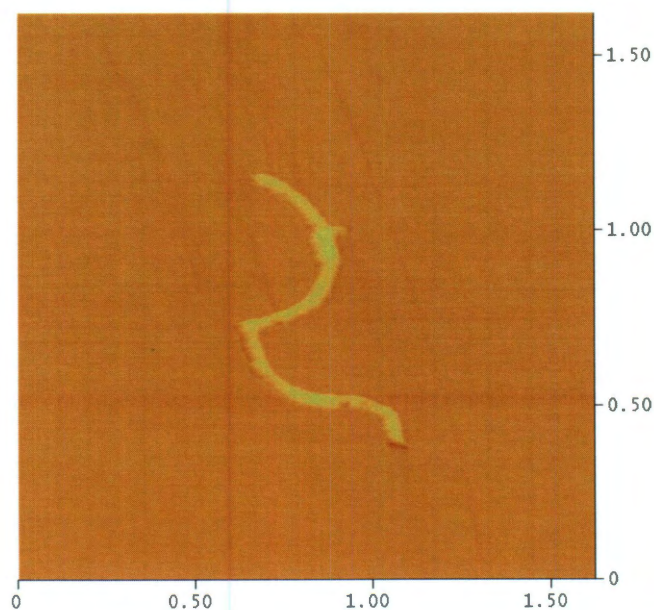


Figure 1.15. AFM image of PEI-MWNT showing polymer "globules" on MWNT.

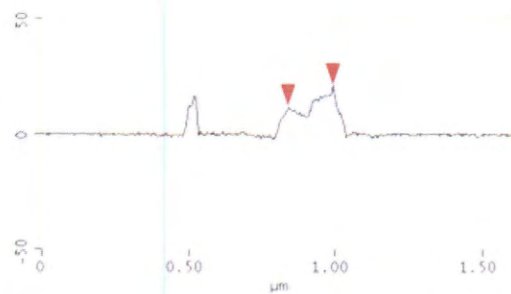


Figure 1.16. AFM sectional analysis of PEI-MWNT showing a height difference of 5.024 nm between functionalized and un-functionalized sections.

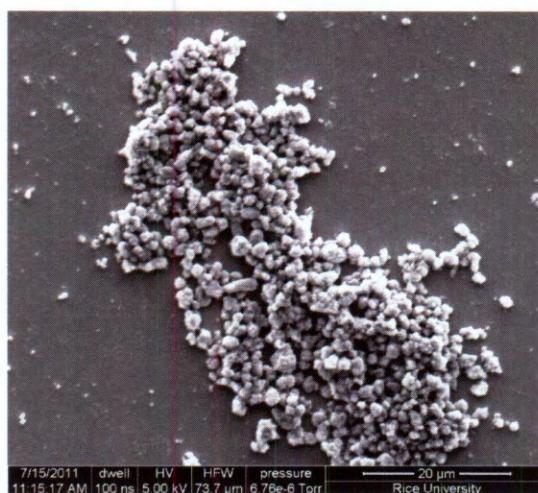


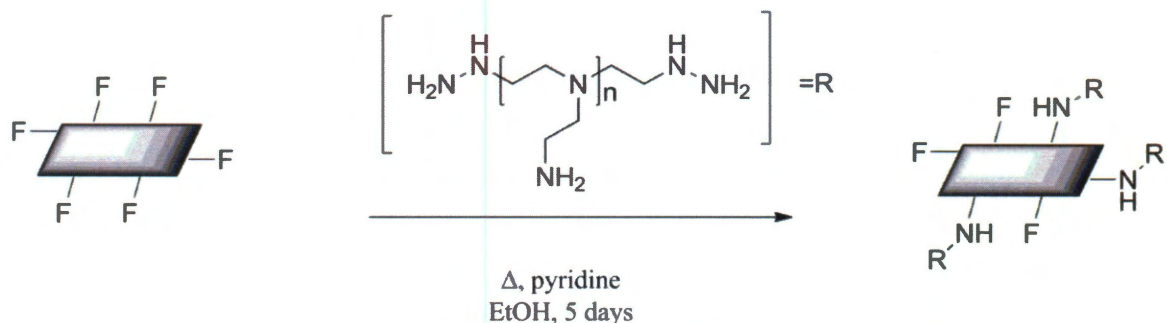
Figure 1.17. SEM analysis of PEI-MWNTs showing large aggregates.



Figure 1.18. SEM image showing the larger aggregates are composed of PEI-MWNTs.

While MWNTs are significantly cheaper than SWNTs and showed similar reactivity, MWNTs are still relatively expensive in comparison to other nanocarbon materials, such as graphite. In order to further reduce the overall cost of the system several PEI-graphite carbon materials were synthesized; PEI-GIC, PEI-GO and PEI-phenylalanine-graphite [PEI-Phe(4-N-G)].

PEI-GIC's. Our previous synthesis of PEI-SWNTs involved the reaction of fluorinated-SWNTs (F-SWNTs) in an ethanol solution of PEI in the presence of pyridine. As with PEI-SWNTs, the same approach was initially taken, i.e. fluorination and subsequent reaction with PEI (Scheme 1.1).



Scheme 1.1. Reaction of PEI with fluorinated graphite intercalation compound (GIC).

The fluorination of graphitic materials results in graphite intercalation compounds (GIC's) which are proposed to have an ionic (rather than covalent) bond between the carbon and fluorine. These ionic carbon fluorine bonds are very labile, meaning characterization and further reactions must be carried out quickly to avoid fluorine loss, evidenced by the etching of their glass containers from the HF by-product. Freshly fluorinated GICs dispersed in EtOH by sonication were added to an EtOH solution of PEI in the presence of pyridine. The reaction was refluxed for five days to yield PEI-functionalized GIC (PEI-GIC).

The Raman spectrum of pristine graphite has no D band which is indicative of a defect free graphitic starting material. The appearance of a small D peak after fluorination indicates a low degree of functionalization (Figure 1.19). The D:G ratio observed upon fluorination (0.11) does not change significantly upon reaction with PEI (0.16). Unlike GO and other functionalized graphenes, there is no loss of the 2D peak, *ca.* 2700 cm^{-1} , indicating no basal plane functionalization occurred. This should mean a low degree of functionalization, which is confirmed by TGA, 5%.

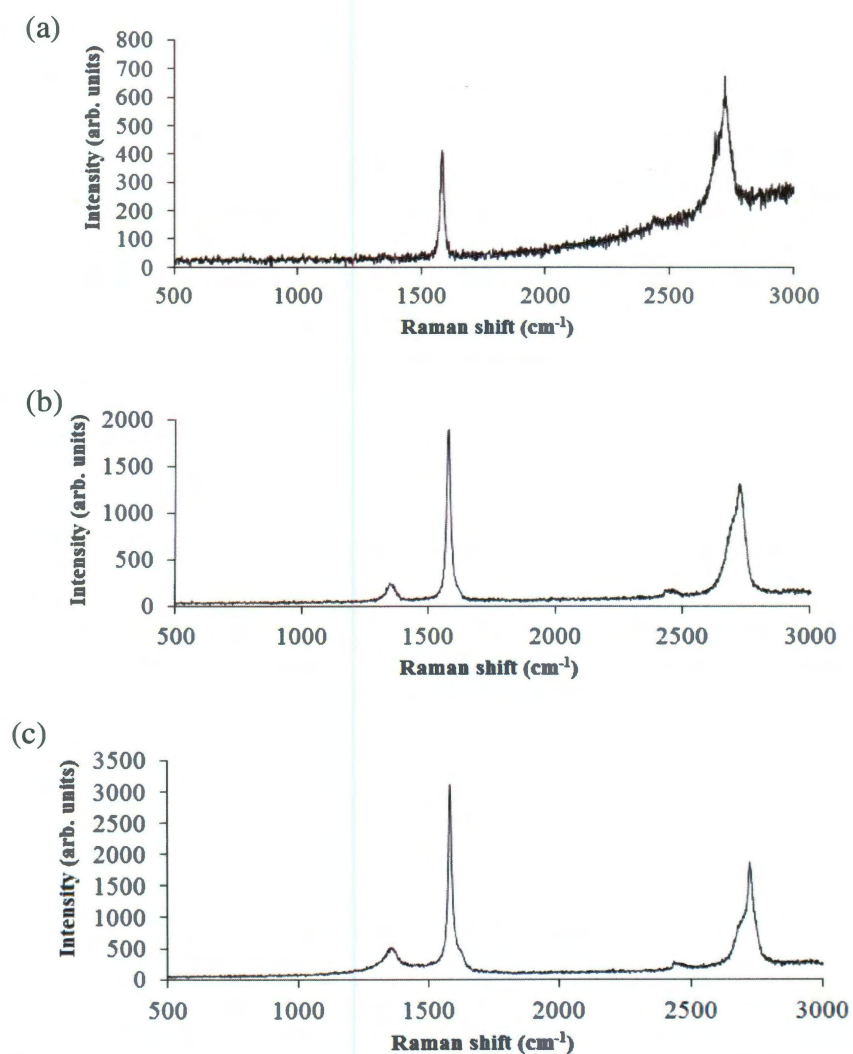


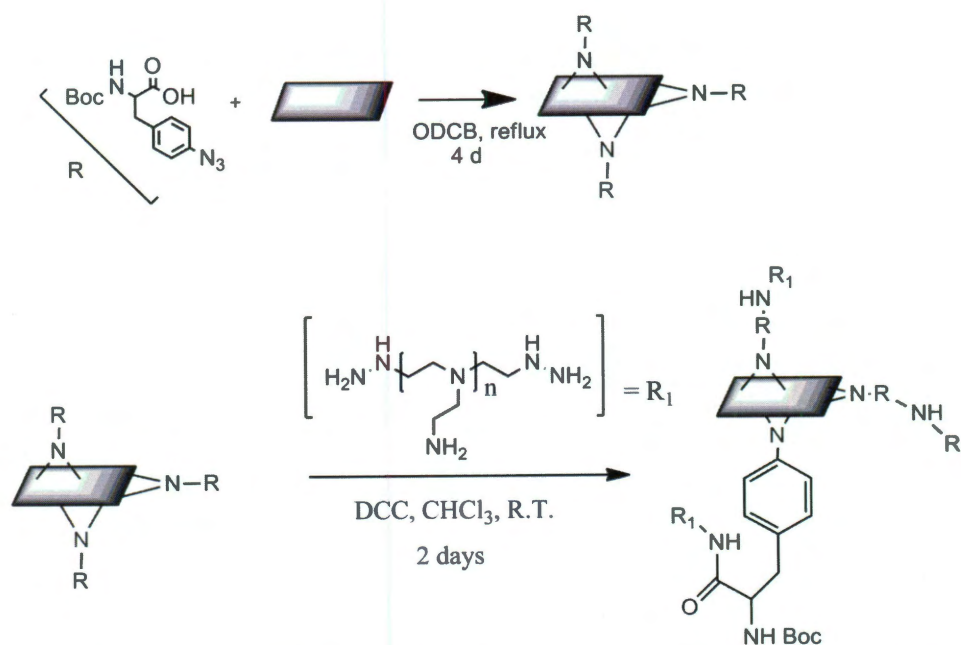
Figure 1.19. Raman spectra (514 nm excitation) of (a) graphite, (b) F-GIC and (c) PEI-GIC.

XPS (Table 1.2) indicates the removal of fluorine and the attachment of PEI, as envisaged by the appearance of a N signal and the presence of a shoulder in the C1s peak associated with the aliphatic C-N groups in the PEI (286.0eV). However the percentage of nitrogen in the sample is quite low (~ 4%) when compared to SWNTs and MWNTs.

The strain induced by the curvature in SWNTs and MWNTs is a driving force for the reaction of amines with fluorinated nanocarbons. This strain is not present in fluorinated graphitic materials and hence the reaction does not proceed to the same degree as with F-SWNTs and F-MWNTs. Another reason for the lack of functionalization is due to the difficulty in controlling the fluorination at low temperatures (<400 °C). As mentioned in the introduction, when graphite is fluorinated at low temperatures, no covalent bonds are formed between the carbon on the basal plane of graphite with fluorine. Instead, a "semi-ionic" bond is formed. This leads to a much less reactive material when compared to F-SWNTs and F-MWNTs, as in these systems covalent bonds are formed, which make neighboring carbon more electrophilic due to the electronegativity of fluorine. The increase in the D:G ratio after fluorination is probably due to covalent bonds between fluorine and the carbons on the edge of the graphite sheets. Since the entire basal plane will not be functionalized, the edges allow for attachment of PEI but in very low concentrations. This conclusion was confirmed by first synthesizing graphite epoxide³⁵ and then reacting it with PEI. Previous studies have shown when that graphite epoxide is synthesized the functionalization takes place on the edges of the sheet and not on the basal plane. The product of reactions with PEI showed a similar degree of functionalization, by TGA, to PEI-GICs indicating that PEI was only added to the edges and not the basal plane.

In order to overcome the low density functionalization, a different graphitic starting material must be used that allows for the functionalization of the entire graphite sheet rather than just the edges. Previous work in the Barron lab has shown that exfoliated graphite can be highly functionalized using azide modified phenylalanine.²³

Azido starting materials can be decomposed into highly reactive nitrenes capable of high density functionalization of the basal plane of graphite. Our initial attempt involved converting some of the amines on 25k Da. branched PEI to azides. The first step was to synthesize the diazo transfer reagent, imidazole sulfonyl azide, which allows for the conversion of primary amines to azides.³⁶ Our goal was that 10% of the primary amines would be converted to azides; however, due to the large molecular weight of the PEI this modification proved challenging. While the presence of azido moieties was detectable by FTIR (*ca.* 2100 cm^{-1}), the reaction with exfoliated graphite proved totally unsuccessful by TGA. Therefore, instead of the azido-PEI route, it was decided to use a modified version of the previously published method to functionalize graphite (G) with Boc-Phe(4-N₃)-OH. The PEI was then coupled onto the Boc-Phe(4-N-G)-OH using a DCC coupling reaction (Scheme 1.2).



Scheme 1.2. Synthesis of PEI-Phe(4-N-G) from Aza-Phe and exfoliated graphite. Phe is Boc protected at the alpha N.

As can be seen from the XPS spectra in Figure 1.20 modification of graphite with Boc-Phe-azide was successful as is evidenced by a large N1s signal and the presence of significant oxygen in the spectrum which comes from the carboxylic acid in Phe and in the Boc protecting group (Table 1.2). While TGA analysis (Table 1.2) further confirms a high degree of functionalization, 57% PEI. This figure is slightly inflated however due to Boc-Phe also decomposing in the same temperature window as PEI.

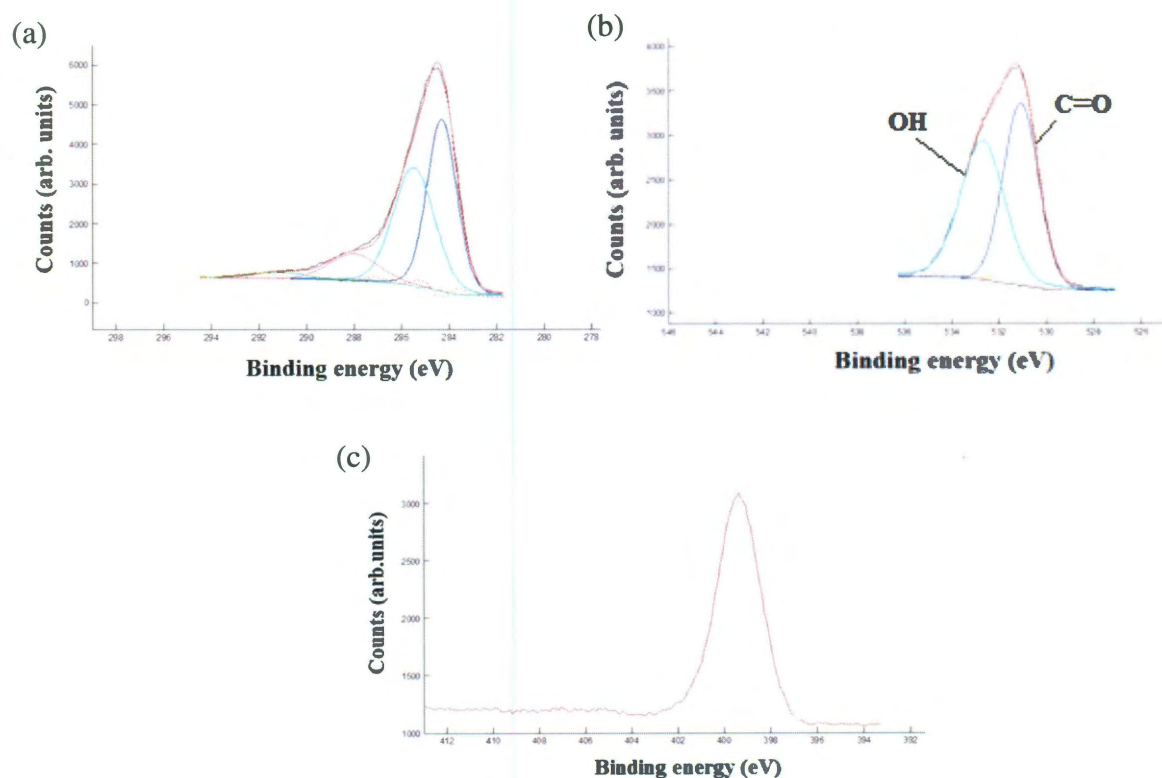


Figure 1.20. (a) C1s spectrum, (b) O1s spectrum and (c) N1s spectrum of phenylalanine modified graphite.

DCC coupling of PEI onto Boc-Phe-N-G has been achieved and can be seen in the XPS data, Figure 1.21, which shows the presence of nitrogen increases significantly from 12.8% to 24.7%, which would be expected if modification was successful.

Furthermore the signal from the hydroxyl, 533 eV, is no longer present in the O1s spectrum of PEI-Phe-N-G, indicating successful DCC coupling.

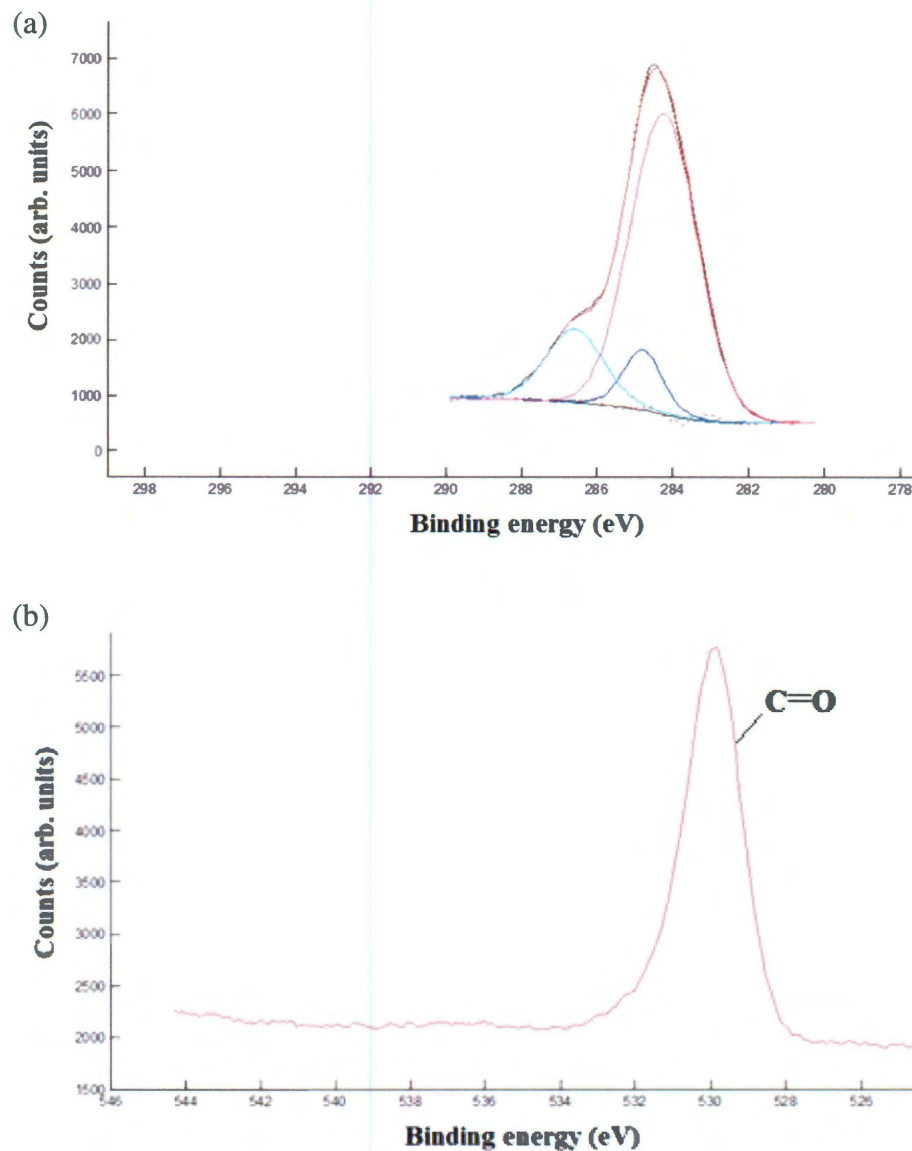
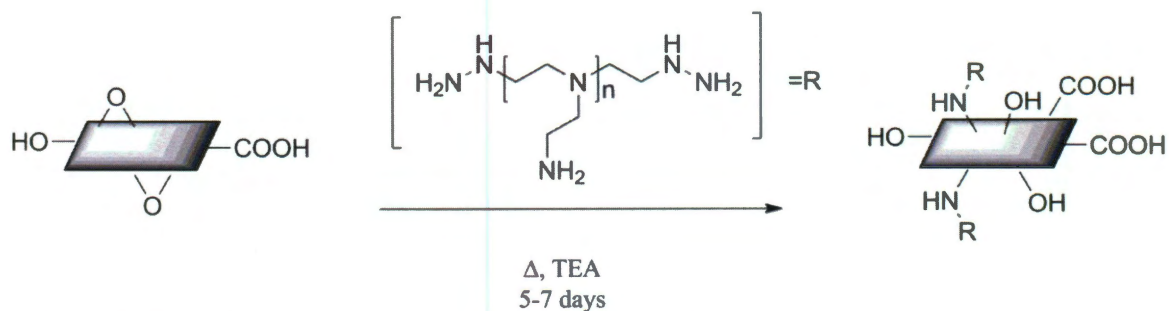


Figure 1.21. (a) C1s and (b) O1s XPS spectra of PEI-Phe-N-G.

Although the PEI coverage on Phe modified graphite is extensive, 24% nitrogen content from XPS (Table 1.2), the overall cost effectiveness of this process is

questionable as many expensive reagents, DCC and azido-Phe, are required. This makes the possible scale up of this process unrealistic. Given the low reactivity of GICs and the expensiveness of the Phe-graphite substrate, we chose to explore an inexpensive highly reactive graphite substrate, graphite oxide.

PEI-GO. The presence of epoxides and hydroxyl groups on the basal plane and carboxylic acids around the perimeter of the sheet make GO extremely hydrophilic. The sources of the GO can be various including commercial sources and those prepared by the methods of Hummer and Offeman,¹⁹ and Tour.³⁷ In these experiments, GO prepared using the Tour method was used. The reaction of graphite oxide (GO) with an appropriate molecular weight polyethyleneimine in the presence of triethylamine (to ensure the majority of the PEI is un-protonated) in ethanol yields PEI-functionalized GO (PEI-GO), Scheme 1.3.



Scheme 1.3. PEI addition to exfoliated GO in refluxing ethanol.

The Raman spectrum (Figure 1.22) of PEI(25000)-GO shows a slight increase in the D:G ratio (0.85) as compared to the GO (0.71), consistent with the proposed reaction. The re-appearance of a broad 2D peak (2700 cm^{-1}) is consistent with multilayer graphite rather than graphene sheets.

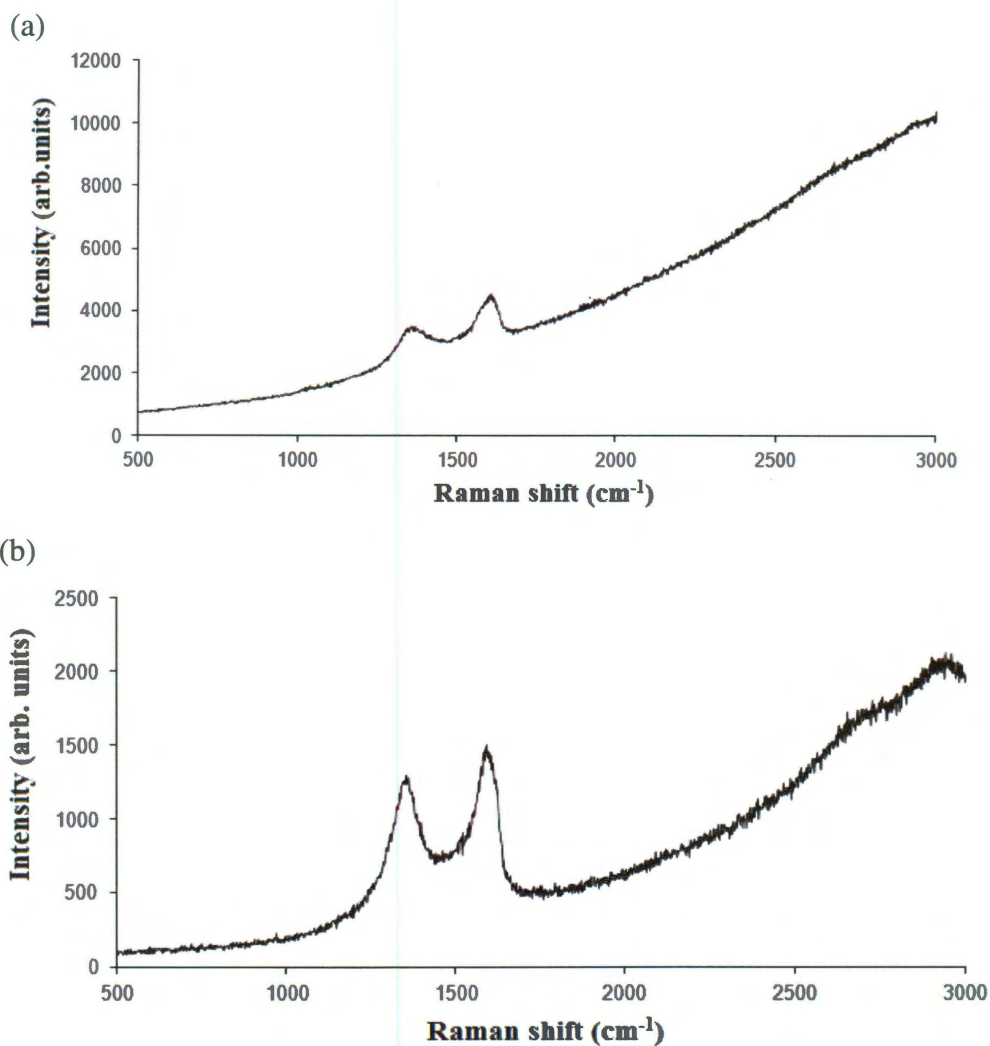


Figure 1.22. Raman spectra of (a) GO and (b) PEI-GO.

The XPS analysis of PEI-GO shows the presence of significant nitrogen (14.5%) and TGA analysis (Table 1.2) indicates a PEI content of approximately 43 wt%. This figure will, however, be slightly inflated due to the fact that some of the oxygen containing groups will burn off concurrently with PEI. The high resolution C1s spectra (Figure 1.23) show a loss of the C-O peak (282.1 eV) in the PEI-GO and the presence of a large shoulder associated with the aliphatic C-N groups in the PEI (286.0 eV).¹⁷ This indicates the covalent modification of GO with PEI. All XPS samples were prepared as a powder and deposited on indium foil for XPS analysis.

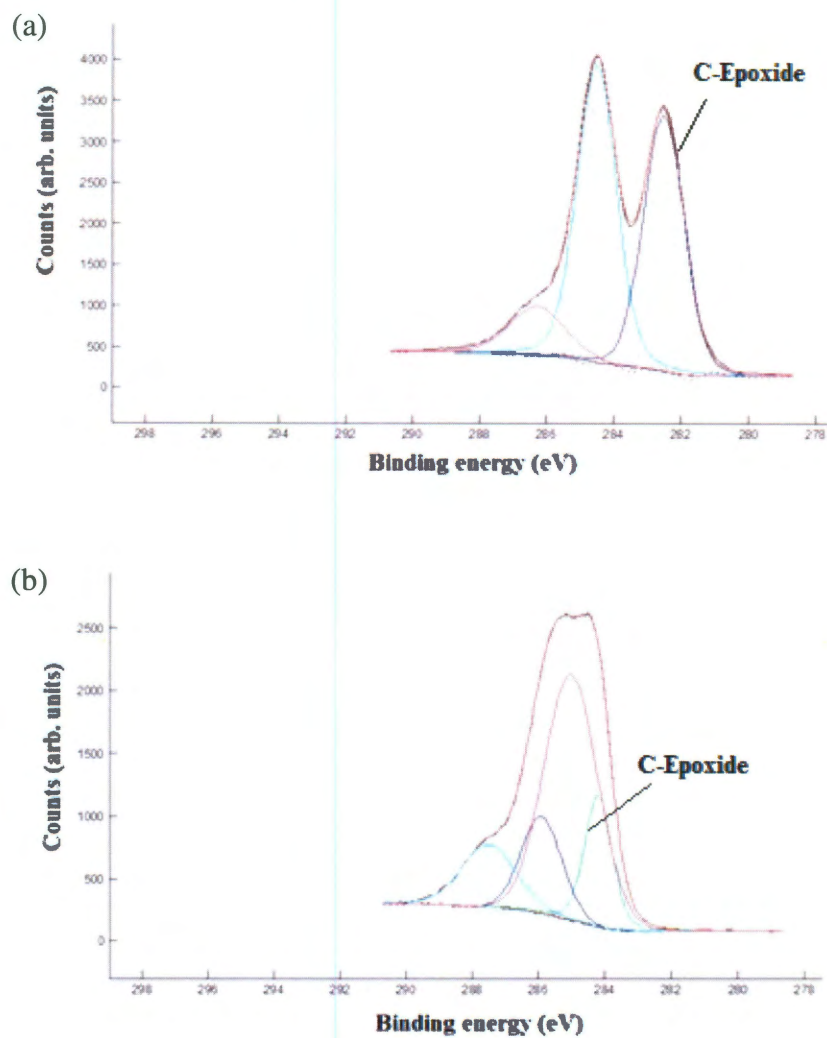


Figure 1.23. XPS C1s spectra of (a) GO and (b) PEI-GO indicating covalent functionalization of GO by PEI.

In summary Table 1.2 shows the atomic content of relevant atoms by XPS, indicating degrees of functionalization, such that PEI-GO ~ PEI-Phe(4-N-G) > PEI-GIC. This is confirmed by TGA, which is also shown in Table 1.2. The percentage of NC, by TGA, is shown rather than the percentage of PEI, due the concurrent thermal

decomposition of other organic species, carboxyls and hydroxyls in the case of PEI-GO and Boc-Phe in the case of PEI-Phe(4-N-G).

Table 1.2. Carbon, nitrogen, oxygen and fluorine content of PEI-graphites by XPS and weight percentage of NC content from TGA.

Sample	% C	% N	% O	% F	% NC
PEI-GIC	91.7	4.5	-	0	95
PEI-Phe(4-N-G)	62.9	24.7	12.4	-	43
PEI-graphite-oxide	75.1	14.5	10.4	-	57

Size analysis of PEI-graphites. Estimating the average size of the PEI-graphites proved to be difficult due to the fact that both graphene-like materials and large aggregates were produced for all the reactions performed. All of the samples were prepared in a similar fashion for imaging, solubilization in water by bath and probe sonication, followed by spin coating onto a cleaved mica substrate for AFM analysis and onto RCA cleaned silicon for SEM imaging. PEI-GICs produced the smallest overall sizes; the majority of the product was a graphene-like material which can be seen in Figure 1.24.

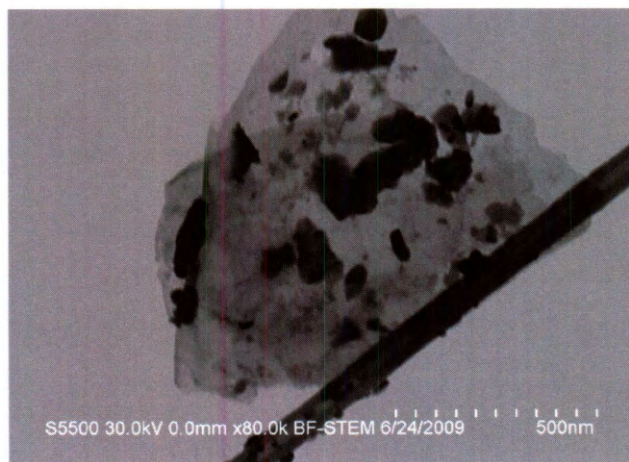


Figure 1.24. TEM image of PEI-GIC showing the presence of PEI (black).

As we can see from STEM imaging, few layer graphene has been exfoliated from the GICs with an average sheet size of 1 - 2 μm . We believe the reason for this is the minimal functionalization achieved by the GIC method, meaning PEI can only functionalized the edges of the material as previously discussed. This results in minimal coverage by PEI leading to only the smallest sizes being solubilized. Further evidence comes from AFM analysis with only small sheets being visible, (Figure 1.25). Samples were spin coated from aqueous solution onto cleaved mica.

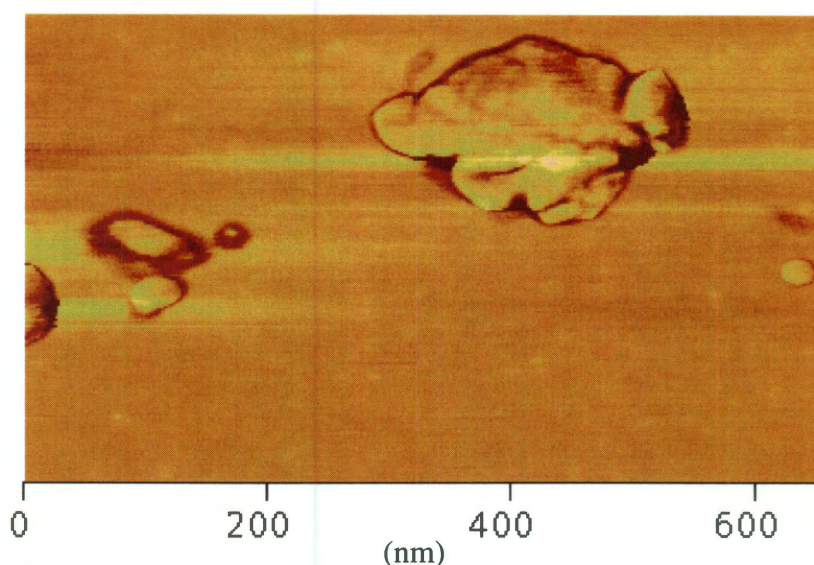


Figure 1.25. AFM image showing the polymer coating on PEI-GIC.

AFM analysis of PEI-Phe(4-N-G) (Figures 1.26 and 1.27) shows multi layer graphite like material. Sectional analysis indicates a height of ~ 150 nm which suggests graphite rather than graphene. Small aggregates were observed with X-Y dimensions ranging from 2 - 20 μm , which is larger than those observed for PEI-GICs. Our postulated reason for this is; due to the higher degree of functionalization, larger flakes can be solubilized. The AFM image also shows PEI on surface of sheets while also showing chains of PEI linking multiple sheets. SEM imaging of PEI-Phe(4-N-G) appears

to confirm the AFM results, with many large aggregates visible (Figure 1.28). The sample was prepared by spin coating on a cleaved mica surface from an aqueous solution.

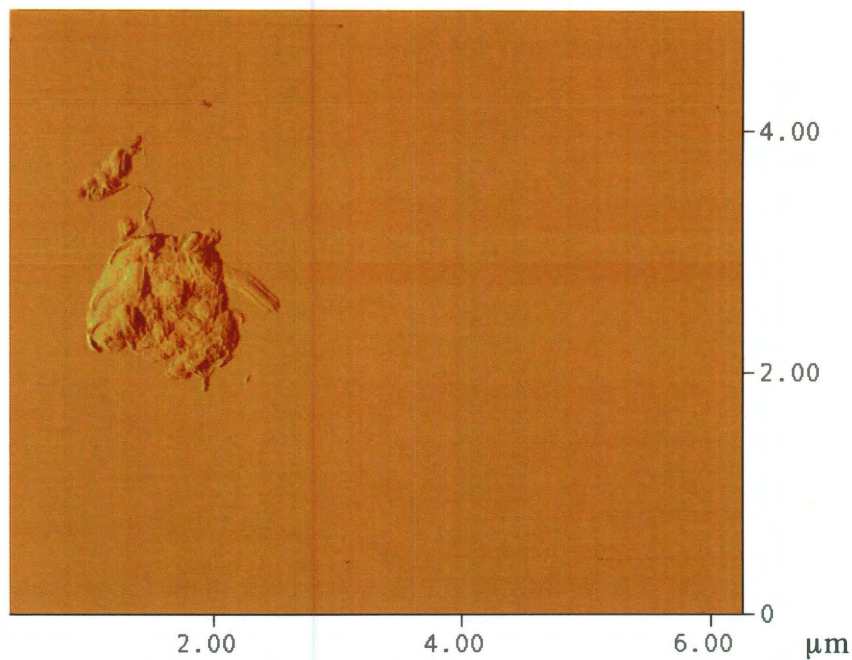


Figure 1.26. AFM image showing PEI functionalized Phe-G with PEI linkages.

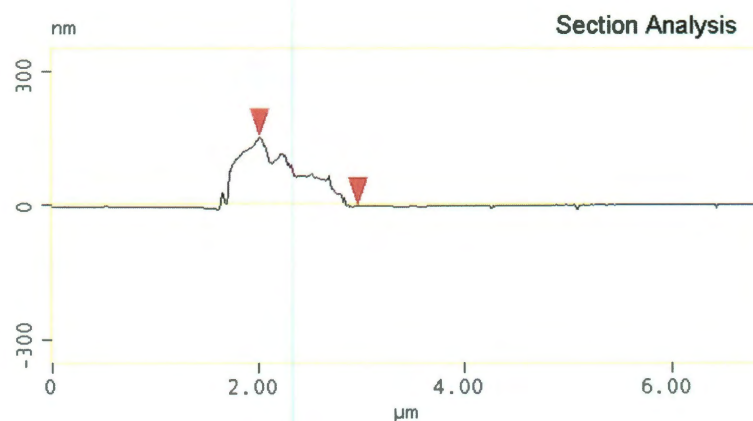


Figure 1.27. AFM sectional analysis of PEI-Phe(4-N-G) indicating a height of 156.62 nm.



Figure 1.28. SEM analysis showing large aggregates of PEI-Phe(4-N-G).

The AFM imaging of PEI-GO (Figure 1.29) shows 0.5 – 1.5 μm particles comprising of multilayer sheets of a thickness between 30 – 50 nm. As we can see from the image, functionalization occurs on the basal plane of graphite and the edges.

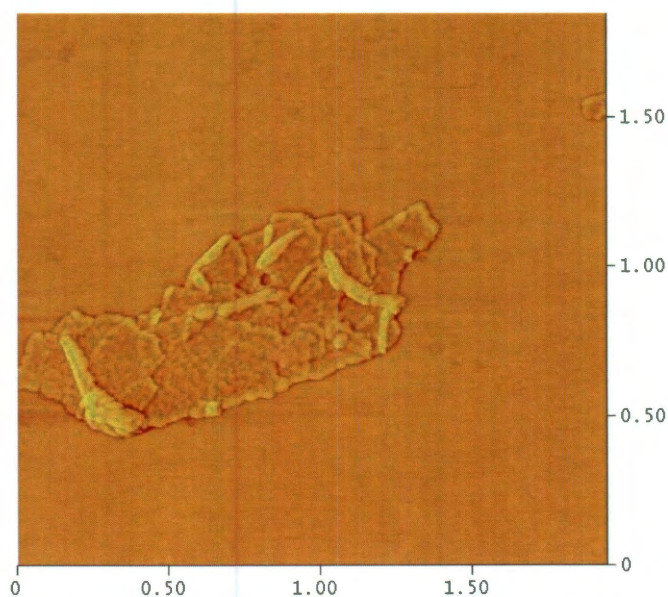


Figure 1.29. AFM image of PEI-GO showing PEI globules on the surface of GO.

SEM imaging (Figure 1.30) suggests large aggregates of graphite sheets. We surmise the reason for these large aggregates is due to the fact that as well as PEI, there are several other moieties present on GO, carboxylic acids and hydroxyls. This will impart optimum solubility on the material allowing for large aggregates to be soluble, which is in contrast to both PEI-GICs and PEI-Phe(4-N-G). Samples were spin coated from an aqueous solution onto RCA cleaned silicon.

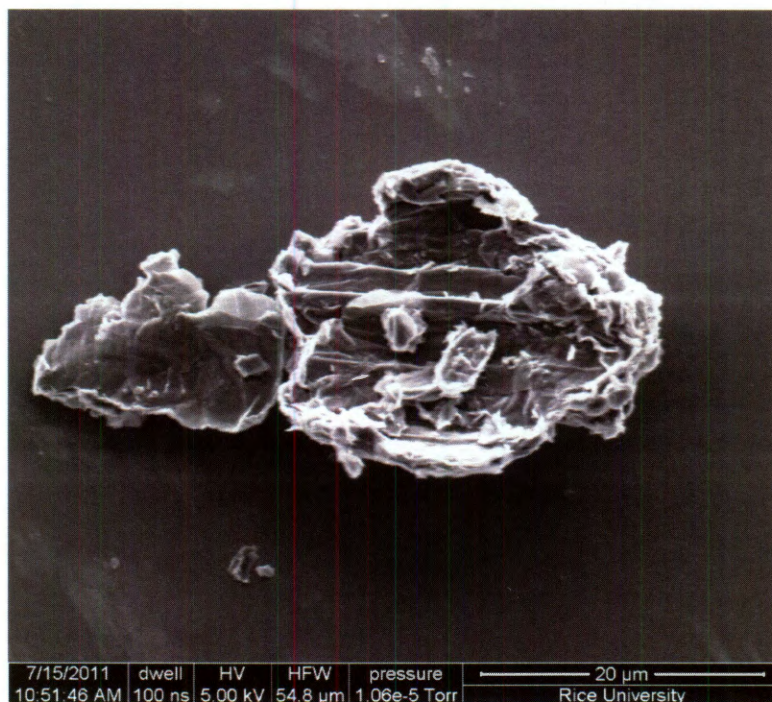


Figure 1.30. SEM image of PEI-GO showing large aggregate structures.

PEI-C₆₀. Initially, when considering a functional material to tether amine groups to, one of the main concerns is that of surface area. Which is why high surface area materials, such as mesoporous silica and carbon nanomaterials are used for many absorption applications. The carbon nanomaterial with the highest surface area is the fullerene with a diameter of approximately 1 nm. After our initial experiments with PEI-SWNTs, fullerene seemed like the next logical material as a substrate for amines.

Toluene is a typical solvent for fullerene, which results in a purpled colored solution, while ethanol was chosen to solubilize the PEI component. When fullerenes react and their conjugation is broken, their optical properties and the color of the solution changes depending on the structure formed. In our initial experiments with fullerenes, the reaction was allowed to proceed until a brown precipitate fell out of solution. The precipitate was collected and characterized by TGA to determine the degree of polymer functionalization, which was low, ~7%. In subsequent experiments, the precipitate was allowed to stir in solution for one week or until the solution was clear and all the material was aggregated on the sidewalls of the flask. The precipitate, PEI-C₆₀, was filtered out of solution and washed copiously with ethanol and toluene and was further characterized in detail. PEI-C₆₀ was insoluble in several solvents, ethanol, water and chloroform. The solubility was still negligible even after the use of a wig-L-bug to break up large aggregates and probe sonication for more than 30 mins.

XPS analysis (Figure 1.31) indicates a large degree of functionalization with the nitrogen content of PEI-C₆₀ measured to be ~13%. Furthermore, the presence of a C-N peak at ~286.5 eV indicates the covalent attachment of PEI to C₆₀. This is shown in the high resolution C1s spectrum which is shown in Figure 1.32. TGA analysis of PEI-C₆₀ confirmed the high degree of functionalization with ~60% of the mass attributed to PEI (Table 1.3).

For AFM analysis the material was probe sonicated in water and drop cast on a cleaved mica substrate as a suspension, due to the insolubility of PEI-C₆₀ in solvents. As can be seen from Figure 1.33 the core of a large aggregate in the center of the image is composed of several small particles that are 1 nm in height (Figure 1.34), indicating that the C₆₀ has been internalized and the PEI externalized in a micellular structure. The PEI spreads out on the surface due to the hydrophilicity of mica.

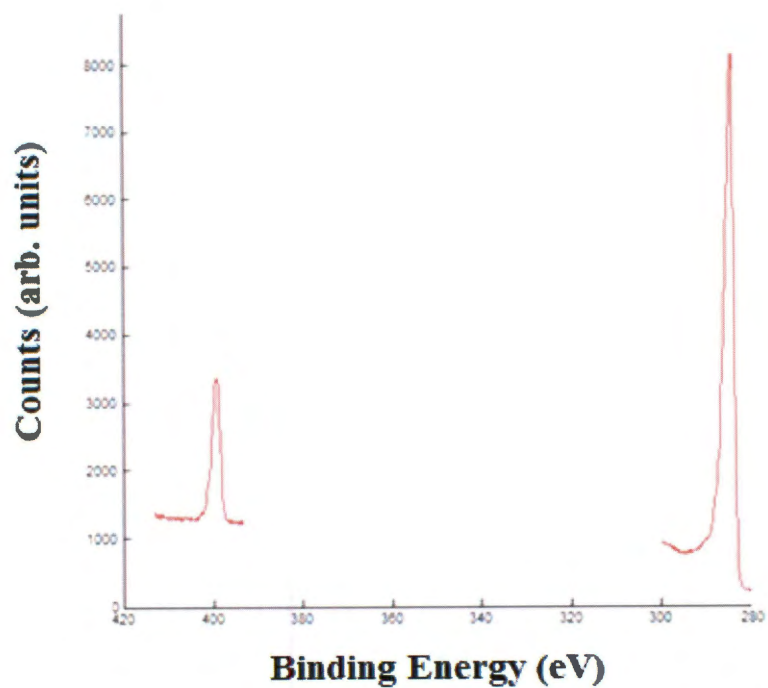


Figure 1.31. XPS survey analysis showing C1s and N1s peaks of PEI-C₆₀.

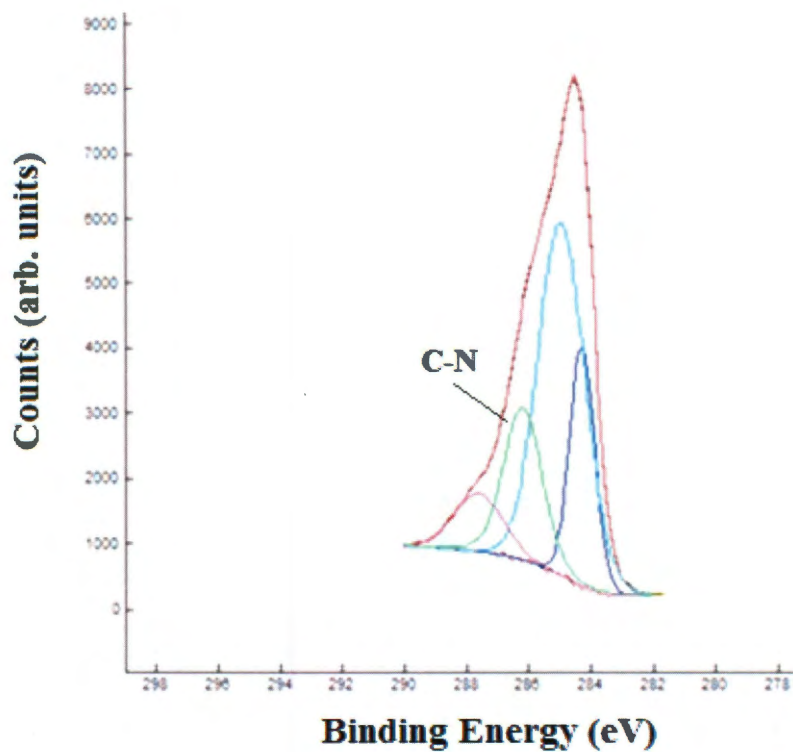


Figure 1.32. C1s XPS spectrum of PEI-C₆₀ showing the presence of C-N bonds at ~286.5 eV.

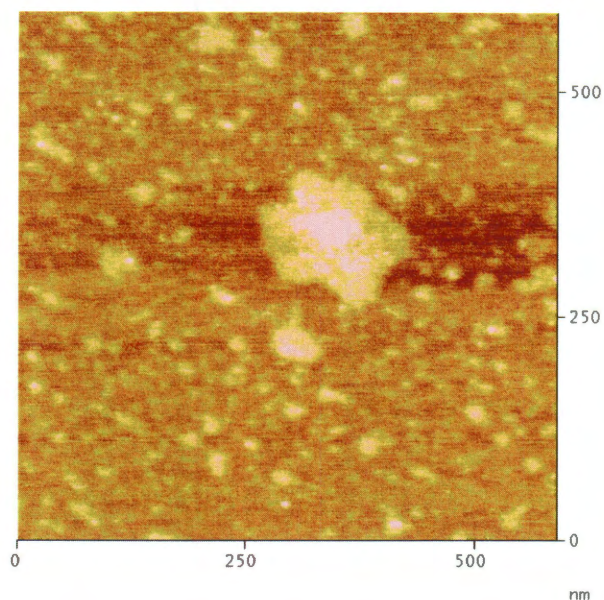


Figure 1.33. AFM image of PEI-C₆₀ showing internalized C₆₀.

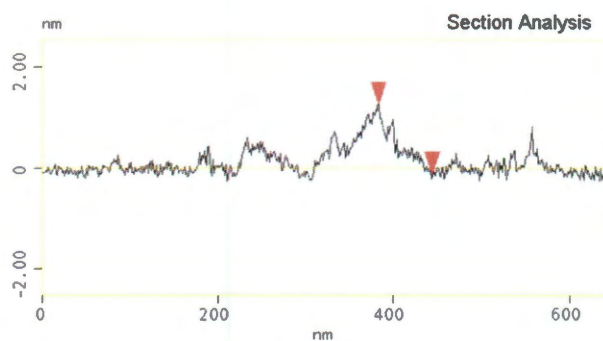


Figure 1.34. AFM sectional analysis of PEI-C₆₀ indicating a height of ~ 2 nm.

Further evidence for the externalization of PEI comes from the SEM image of PEI-C₆₀ (Figure 1.35) imaged as a powder. As can be seen the entire external shell of the PEI-C₆₀ is comprised of nodules of polymer. This made image collection difficult as any long term beam exposure resulted in polymer melting. Gold coating, a short dwell time and a beam voltage of 15 kV were eventually used in image capture. The SEM micrograph reveals a highly interconnected network of polymer nodules that was consistent with PEI-MWNT samples imaged as dry powders. However, in the case of the

PEI-MWNTs, the large aggregates were bundled MWNTs. From this we can surmise that the nanocarbons may serve as nucleation points for the polymer to react with and wrap around. Given that we used branched PEI with many primary amines, one can expect that one PEI chain would react with several nanocarbon molecules resulting in the highly interconnected network that we see.

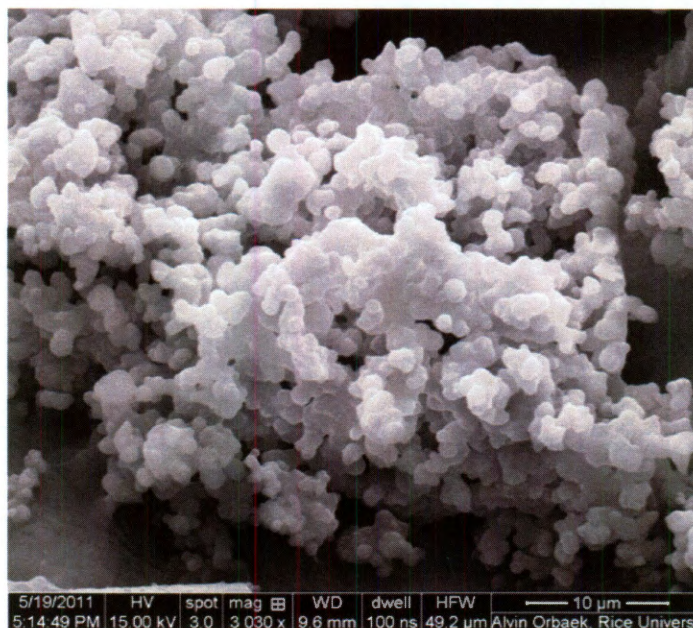


Figure 1.35. SEM image of PEI-C₆₀ in powdered form.

Conclusions

The results of the differing extents of functionalization of all the materials is shown in Table 1.3. In summary, several polyethylenimine-nanocarbons have been synthesized by a variety of different methods with the goal of maximum polymer functionalization. Initially PEI-SWNTs of varying molecular weights (600 - 25k Da.) of branched PEI, were formed by the reaction of PEI with fluorinated SWNTs in the presence of pyridine. PEI-SWNTs were fully characterized which led to the discovery of possible CO₂ absorption qualities (Chapter 2) in addition to the potential biological applications.

Table 1.3. Summary of physical properties of synthesized materials.

Sample	% C	% N	% O	% F	% NC
PEI-SWNT	85	12	-	3	42
PEI-MWNT	90	9	-	1	60
F-graphite	95.6	-	-	2.4	
PEI-GIC	91.7	4.5	-	0	95
Phe-graphite	72.8	12.8	14.3	-	-
PEI-Phe(4-N-G)	62.9	24.7	12.4	-	43
graphite oxide (GO)	52.8	-	47.2	-	
PEI-GO	75.1	14.5	10.4	-	57
PEI-C ₆₀	87	13	-	-	40

Given PEI-SWNTs potential as a capture agent, it was decided that several other PEI-nanocarbons would be synthesized to see if these absorption properties could be utilized in a more cost effective way. To that end MWNTs were functionalized utilizing the same method of fluorinated nanocarbon starting materials. This resulted in a product similar to PEI-SWNTs, PEI-MWNTs, with PEI coverage in bands along the tube, similar to SWNTs. The degree of functionalization was less than that of SWNTs due to the interior layers of MWNT not being functionalized.

Several PEI-graphite compounds were also synthesized, PEI-GICs, PEI-Phe-G and PEI-GO. PEI-GICs were synthesized using fluorine chemistry, at low temperature which results in fluorine intercalated graphite rather than covalent fluorine-carbon bonds. This method resulted in a low degree of polymer functionalization probably due to edge only functionalization. To achieve a higher degree of surface coverage, a previously published method from the Barron lab was used to synthesize Phe-G. PEI was then coupled to Phe using a DCC coupling reaction, resulting in PEI-Phe-G. The degree of

functionalization was comparable to that of SWNT and MWNT (Table 1.3); however, the cost effectiveness of this process is questionable due to the use of coupling reagents and azido chemistry. As an alternative, PEI-GO was then synthesized by using the known reaction of amines with epoxides through backside attack. The degree of functionalization was once again comparable to that of SWNTs and MWNTs (Table 1.3). Graphitic materials ranged in size with PEI-GO and PEI-Phe(4-N-G) being similar with sizes ranging from 100 nm to 50 μm , while PEI-GICs showed smaller aggregates, 1 - 2 μm .

Initially after synthesizing PEI-SWNTs, fullerenes were the next logical step due to their high surface area. Our initial experiments with C_{60} resulted in minimally functionalized fullerenes. However, a change in the reaction method led to a highly functionalized PEI- C_{60} conjugate. Imaging analysis from water indicated that the PEI- C_{60} was forming micellular structures in water, which is to be expected. The CO_2 absorption potential of these PEI-nanocarbons will be examined in Chapter 2 as well as their potential as drug delivery vehicles.

In conclusion, a variety of PEI-nanocarbons were synthesized and fully characterized in an attempt to find a synthetic route leading to maximal polymer coverage of the nanocarbon with PEI. In that regard, the polymer coverage exhibited the following trend: $\text{C}_{60} > \text{SWNT} > \text{graphites}$. The trend is reasonable when considering the reactivities of the various nanocarbon structures. The highest polymer functionalization with the lowest overall cost was achieved with PEI-SWNTs, PEI- C_{60} and PEI-GO. Future experiments regarding capture and release of small molecules will utilize these constructs and will be discussed in Chapters 2 and 3.

Experimental

Pristine HiPco SWNTs were obtained through the Carbon Nanotube Laboratory (CNL) at Rice University and were purified by the wet-air oxidation procedure at 250 $^{\circ}\text{C}$

for 24 hours to remove any iron and carbon impurities.¹ The degree of purification was determined using TGA analysis in air and showed that the purified SWNTs contained less than 3% iron content after purification. Fluorination of the purified nanotubes was achieved using a previously reported procedure²⁷ and yielded a stoichiometry of $C_{2.7}F$ as determined by the difference in mass and was confirmed XPS analysis. Branched polyethyleneimine ($M_w = 600, 1800, 10000$ and 25000 Da) and linear polyethyleneimine ($M_w 25000$ Da) (Alfa Aesar) EtOH (AAPER Alcohol) and pyridine (Aldrich) were used as received. All water was ultra pure (UP), obtained from a Millipore Milli-Q UV water filtration system.

Characterization was performed using a FEI XL30 Schottky field-emission environmental scanning electron microscope (ESEM) with EDAX energy dispersive spectroscopy capability and a JEOL 6500F thermal field-emission scanning electron microscope. These were used at accelerating voltages of 30 and 15 kV respectively. Samples were mounted with carbon tape onto aluminum microscopy specimen mounts (Electron Microscopy Sciences). Before imaging, insulating samples were sputter coated (Plasma Sciences CRC 100 sputter coater) with a thin layer of gold or chromium to prevent charging. X-ray photoelectron spectra (XPS) were acquired on a PHI 5700 ESCA system (Physical Electronics) at 15 kV, using an aluminum target and an 800 μm aperture. Samples were pressed into indium metal. Transmission electron microscopy was performed with a JEOL 2010 instrument at 100 kV utilizing a JEOL FasTEM system. Samples were dropped onto Cu grids with lacey carbon film (Electron Microscopy Sciences) and allowed to dry thoroughly before imaging. Raman spectroscopy on solids (both 785 and 532 nm excitation) was performed using a Renishaw Raman microscope. Samples were mounted on double sided tape. Attenuated total reflectance infrared spectroscopy (ATR-IR, $4000 - 600 \text{ cm}^{-1}$) of solids was obtained using a Nicolet Nexus 670 FT-IR with a diamond window. UV/vis spectra (200 – 1400

nm) were collected using a Cary 5000 UV/Vis-NIR spectrometer using quartz cuvettes. Thermal analysis was performed on a Seiko TG/DTA 200 using aluminum pans.

PEI-SWNT. Covalent functionalization of SWNTs was achieved through the reaction of branched and linear PEI with F-SWNTs by dispersing F-SWNTs (20 mg) in EtOH (25 mL) by the use of probe sonication for 20 minutes. This was combined with 25 mL of a 0.1 M branched-PEI (M_w 600) solution in EtOH into a 100 mL round bottomed flask fitted with a condenser and a magnetic stir bar. Pyridine (1 mL) was added to the reaction mixture and the reaction was brought to reflux, ca. 24 hours, with continuous stirring. Upon completion of the reaction, SWNT recovery was achieved by filtration of the reaction mixture through a 0.2 μ m membrane PTFE filter (Cole Parmer). The filtrate was washed with copious amounts of absolute EtOH followed by de-ionized water to remove pyridine and any unreacted polymer. The PEI(600)-SWNT product was then removed from the filter paper without drying and transferred to a plastic centrifuge tube and was dispersed in de-ionized water via probe sonication, ~15 minutes. The suspended PEI-SWNTs were then centrifuged at 4400 rpm for 15 minutes. The PEI-SWNT decant was removed and stored at room temperature in a plastic centrifuge tube. This same procedure was also repeated for the preparation of PEI(1800)-SWNT and PEI(10000)-SWNT using 0.04 M and 0.008 M solutions of branched-PEI (M_w = 1800 and 10000 Da) in EtOH, respectively. The linear-PEI(25000)-SWNT was prepared using the above procedure with 25 mL of 0.003 M linear-PEI (M_w = 25000 Da) in EtOH.

PEI(600)/SWNT. Physical adsorption of PEI to the sidewalls of SWNTs was achieved by dispersing purified SWNTs (20 mg) into EtOH (25 mL) by probe sonication for 20 minutes. This was combined with 25 mL of a 0.1 M PEI (M_w = 600 Da) solution in EtOH in a 100 mL round bottomed flask fitted with a condenser and a magnetic stir bar. The reaction mixture was brought to reflux, ca. 24 hours, with continuous stirring.

Upon completion the recovery, purification, and storage of the PEI adsorbed SWNT was achieved using the method previously described for the covalently attached PEI-SWNTs. A similar reaction is used to prepare PEI(600)/F-SWNT physical absorbed conjugates.

pH solubility studies. Solutions of pH 1.7, 3.25, 5.7, 8.31, 11.21 and 13.28 were prepared. De-ionized water with a measured pH of 5.7 was also used for all samples. The acidic solutions (pH 1.7 and 3.25) were prepared by the dilution of 1 M HCl with water. The pH of each solution was constantly monitored using a pH probe. Two sets of basic pH solutions (pH 11.21 and 13.28) were prepared by the addition of dilution of NaHCO₃ and NaOH, respectively. An aqueous solution containing the PEI-SWNT's (2 mL of 4 mg.mL⁻¹) was then added to each solution.

Synthesis of PEI-MWNT. Covalent functionalization of MWNTs was achieved through the reaction of branched 25000 Da.PEI with F-MWNTs by dispersing F-MWNTs (20 mg) in EtOH (25 mL) by the use of probe sonication for 20 minutes. Concurrently 500 mg of PEI was dispersed in EtOH. These solutions were combined in a 100 mL round bottomed flask fitted with a condenser and a magnetic stir bar. Pyridine, (1 mL), was added to the reaction mixture and the reaction was brought to reflux, ca. 24 hours, with continuous stirring. Upon completion of the reaction, MWNT recovery was achieved by filtration of the reaction mixture through a 0.2 μm membrane PTFE filter (Cole Parmer). The filtrate was washed with copious amounts of absolute EtOH followed by de-ionized water to remove pyridine and any unreacted polymer.

Reaction of PEI with fluorinated graphite. Natural graphite powder (99.999% pure) was fluorinated in a custom built fluorination reactor, using a flow gas of 10% fluorine in nitrogen¹⁵. The flow rate was set to 15 sccm. Additionally a flow of 2% H₂ in nitrogen was flowed into the reactor at a flow rate of 10 sccm. Once the reaction was

complete, the F_2 and H_2 were turned off and the reactor was then purged with Ar at 1000 sccm for a period of about 15 min. Vacuum was then pulled on the system for a period of 15 min. Argon was then flowed back into the reactor and the reactor is opened and the sample was removed. Freshly fluorinated graphite intercalation compounds (GICs) (100 mg) were dispersed in EtOH (100 mL) via bath sonication. PEI (500 mg) of a chosen molecular weight was dispersed in EtOH via bath sonication. The two solutions were combined and pyridine (*ca.* 1 mL) was added to the reaction. The reaction was heated to reflux temperature with constant stirring for 5 days. After vacuum filtration through a 200 nm pore size PTFE filter and washing with EtOH and DI H_2O the sample was oven dried at ~ 120 °C.

Synthesis of PEI-Phe(4-N-G)raphite. Initially natural graphite powder (100 mg, 99.999 % pure) was exfoliated into ortho-dichlorobenzene (~ 50 mL) via probe sonication for approximately 2 hours. Boc-Phe(4- N_3)-OH (100 mg) was added with vigorous stirring and the solution was brought to reflux for a period of 4 days. The product was recovered via filtration through a 200 nm pore size PTFE filter. The Phe modified graphite was then dispersed in chloroform (50 mL), to this solution 100 mg of N,N'-Dicyclohexylcarbodiimide (DCC) was added and allowed to stir for approximately 2 hours. Concurrently PEI (~ 1 g) was solubilized in chloroform. These two solutions were then combined and vigorously stirred for a period of 24 hours at room temperature. The product was recovered via vacuum filtration through a 200 nm PTFE filter and washed with copious amounts of chloroform to remove any unreacted DCC or PEI.

Reaction of PEI with graphite oxide. A branched PEI (25 kDa) is dispersed in EtOH (100 mL) via bath sonication. To this solution is added triethylamine (200 μ L). Concurrently, graphite oxide (GO) (100 mg) is dispersed in water (100 mL). The two solutions are added together and heated to reflux for a period of 5 – 7 days with constant

stirring. Recovery of the PEI-GO is achieved by filtering the product solution through a 0.2 μm PTFE filter paper and washed with copious amounts of EtOH and H₂O. For CO₂ absorption experiments, the recovered PEI-GO was allowed to dry in an oven at 120 °C for a period of 1 hr to remove any water or residual CO₂.

References

1. S. Ramesh, L. M. Ericson, V. A. Davis, R. K. Saini, C. Kittrell, M. Pasquali, W. E. Billups, W. W. Adams, R. H. Hauge and R. E. Smalley, *J. Phys. Chem. B*, 2004, **108**, 8794.
2. C. Hu, Y. Zhang, G. Bao, Y. Zhang, M. Liu and Z. L. Wang, *J. Phys. Chem. B*, 2005, **109**, 20072.
3. M. J. O'Connell, P. Boul, L. M. Ericson, C. Huffman, Y. Wang, E. Haroz, C. Kuper, J. Tour, K. D. Ausman and R. E. Smalley, *Chem. Phys. Lett.*, 2001, **342**, 265.
4. P. Cherukuri, S. M. Bachilo, S. H. Litovsky and R. B. Weisman, *J. Am. Chem. Soc.*, 2004, **126**, 15638.
5. Y. Xu, P. E. Pehrsson, L. Chen, R. Zhang and W. Zhao, *J. Phys. Chem. C*, 2007, **111**, 8638.
6. H. Peng, L. B. Alemany, J. L. Margrave and V. N. Khabashesku, *J. Am. Chem. Soc.*, 2003, **125**, 15174.
7. J. M. Berlin, A. D. Leonard, T. T. Pham, D. Sano, D. C. Marcano, S. Yan, S. Fiorentino, Z. L. Milas, D. V. Kosynkin, B. K. Price, R. M. Lucente-Schultz, X. Wen, M. G. Raso, S. L. Craig, H. T. Tran, J. N. Myers and J. M. Tour, *ACS Nano*, 2010, **4**, 4621.

8. J. J. Stephenson, A. K. Sadana, A. L. Higginbotham and J. M. Tour, *Chem. Mater.*, 2006, **18**, 4658.
9. J. L. Bahr and J. M. Tour, *Chem. Mater.*, 2001, **13**, 3823.
10. M. Holzinger, J. Abraham, P. Whelan, R. Graupner, L. Ley, F. Hennrich, M. Kappes and A. Hirsch, *J. Am. Chem. Soc.*, 2003, **125**, 8566.
11. Y. Chen, R. C. Haddon, S. Fang, A. M. Rao, P. C. Eklund, W. H. Lee, E. C. Dickey, E. A. Grulke, J. C. Pendergrass, A. Chavan, B. E. Haley and R. E. Smalley, *Journal of Materials Research*, 1998, **13**, 2423.
12. K. J. Ziegler, Z. Gu, H. Peng, E. L. Flor, R. H. Hauge and R. E. Smalley, *J. Am. Chem. Soc.*, 2005, **127**, 1541.
13. T. Ramanathan, F. T. Fisher, R. S. Ruoff and L. C. Brinson, *Chem. Mater.*, 2005, **17**, 1290.
14. B. K. Price, J. R. Lomeda and J. M. Tour, *Chem. Mater.*, 2009, **21**, 3917.
15. E. T. Mickelson, C. B. Huffman, A. G. Rinzler, R. E. Smalley, R. H. Hauge and J. L. Margrave, *Chem. Phys. Lett.*, 1998, **296**, 188.
16. K. F. Kelly, I. W. Chiang, E. T. Mickelson, R. H. Hauge, J. L. Margrave, X. Wang, G. E. Scuseria, C. Radloff and N. J. Halas, *Chem. Phys. Lett.*, 1999, **313**, 445.
17. E. P. Dillon, C. A. Crouse and A. R. Barron, *ACS Nano*, 2008, **2**, 156.
18. Z. Gu, H. Peng, R. H. Hauge, R. E. Smalley and J. L. Margrave, *Nano Lett.*, 2002, **2**, 1009.
19. W. S. Hummers and R. E. Offeman, *J. Am. Chem. Soc.*, 1958, **80**, 1339.
20. S. Park and R. S. Ruoff, *Nat Nano*, 2010, **5**, 309.
21. A. B. Bourlinos, D. Gournis, D. Petridis, T. Szabó, A. Szeri and I. Dékány, *Langmuir*, 2003, **19**, 6050.
22. C. E. Hamilton, J. R. Lomeda, Z. Sun, J. M. Tour and A. R. Barron, *Nano Lett.*, 2009, **9**, 3460.

23. T. A. Strom, E. P. Dillon, C. E. Hamilton and A. R. Barron, *Chem. Commun.*, 2010, **46**, 4097.
24. C. Hamilton, J. Lomeda, Z. Sun, J. Tour and A. Barron, *Nano Res.*, 2010, **3**, 138.
25. I. Palchan, M. Crespin, H. Estrade-Szwarckopf and B. Rousseau, *Chem. Phys. Lett.*, 1989, **157**, 321.
26. T. Mallouk and N. Bartlett, *Chem. Commun.*, 1983, 103.
27. T. Nakajima, *J. Fluorine Chem.*, 1999, **100**, 57.
28. K. E. Geckeler and A. Hirsch, *J. Am. Chem. Society*, 1993, **115**, 3850.
29. S. H. Friedman, D. L. DeCamp, R. P. Sijbesma, G. Srdanov, F. Wudl and G. L. Kenyon, *J. Am. Chem. Soc.*, 1993, **115**, 6506.
30. M. Prato and M. Maggini, *Acc. Chem. Res.*, 1998, **31**, 519.
31. J. Yang and A. R. Barron, *Chem. Commun.*, 2004, 2884.
32. M. Hashiguchi, K. Watanabe and Y. Matsuo, *Organic & Biomolecular Chemistry*, 2011, **9**, 6417.
33. W.-B. Zhang, J. He, X. Dong, C.-L. Wang, H. Li, F. Teng, X. Li, C. Wesdemiotis, R. P. Quirk and S. Z. D. Cheng, *Polymer*, 2011, **52**, 4221.
34. J. Wang, G.-X. Chen, J. Sun and Q. Li, *J. Phys. Chem. B*, 2011, **115**, 2824.
35. J. Chattopadhyay, A. Mukherjee, C. E. Hamilton, J. Kang, S. Chakraborty, W. Guo, K. F. Kelly, A. R. Barron and W. E. Billups, *J. Am. Chem. Soc.*, 2008, **130**, 5414.
36. E. D. Goddard-Borger and R. V. Stick, *Org. Lett.*, 2007, **9**, 3797.
37. D. C. Marcano, D. V. Kosynkin, J. M. Berlin, A. Sinitskii, Z. Sun, A. Slesarev, L. B. Alemany, W. Lu and J. M. Tour, *ACS Nano*, 2010, **4**, 4806.

Chapter 2

Carbon Dioxide Absorption Potential of Polyethylenimine Functionalized Carbon Nanomaterials

Introduction

In recent years the debate about climate change has come to the forefront of society. In 1997 the United Nations framework convention on climate change introduced the Kyoto protocol in Kyoto, Japan. The goal of the Kyoto protocol was to mandate the largest greenhouse gas emitters in the world to reduce their emissions of the four main gasses responsible for an increase in the greenhouse effect: carbon dioxide (CO_2), methane (CH_4), nitrous oxide (N_2O) and sulfur hexafluoride (SF_6).¹ It is worth noting that the greenhouse effect is not hazardous to life on Earth, in fact, if it wasn't for the greenhouse effect there would be no life on the planet. The greenhouse effect serves to warm the planet by retaining some of the radiation that is re-emitted by the earth after being absorbed from the sun. The heating phenomena is due to the scattering of infrared radiation as it passes through the greenhouse gasses, which absorb and re-emit some of that energy back down to the Earth's surface.² As the concentrations of these greenhouse gasses increase so too does the amount of heat that is retained, leading to an overall increase in global temperatures and subsequent climate change. However, this final conclusion is a source of debate.

Among the greenhouse gasses, carbon dioxide is not the most damaging of the greenhouse gases when compared in equal concentrations. However the concentration of CO_2 in the atmosphere is the highest of the greenhouse gasses, excluding water vapor which cannot be readily controlled. There are several ways that CO_2 is emitted into our atmosphere, including the burning of fossil fuels, chemical reactions (manufacture of cement), and other natural sources such as volcanic eruptions.

The longest constant record of the CO₂ concentration in our atmosphere comes from the Mauna Loa observatory in Hawaii (Figure 2.1).³ These measurements were started in March of 1958 by C. David Keeling of the Scripps Institution of Oceanography.

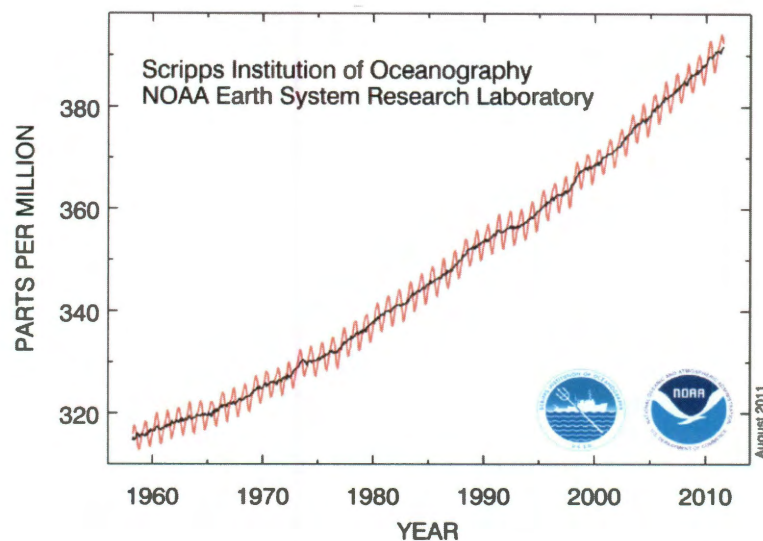


Figure 2.1. Measured CO₂ concentration in the atmosphere at Mauna Loa observatory. Earth System research Laboratory, <http://www.esrl.noaa.gov/gmd/ccgg/trends/>, Accessed 5/15/11, 2011.

As the diagram illustrates, the CO₂ concentration in the atmosphere has been increasing at a steady rate since the study began in 1958, with no signs of slowing. As of the year 2000, the amount of CO₂ emitted annually, on a global scale is ~ 23.5 GtCO₂.yr⁻¹.¹ Of this figure, approximately 60% comes from large stationary emitters that produce a minimum of greater than 0.1 MtCO₂ yr⁻¹.⁴ Because of this dramatic upward trend and its possible ramifications, the scientific community began to look for ways to reduce the amount of CO₂ in our atmosphere. There are several different ways to achieve this reduction, from converting cars to be powered by electricity or hydrogen and converting power supplies to clean energy alternatives such and wind and solar, to capturing CO₂ as

it is emitted from fossil fuel burning power plants, i.e., CO₂ scrubbing. The typical flue gas composition from gas and coal fired power plants are shown in Table 2.1.

Table 2.1. Typical flue gas composition from gas and coal fired power plants.⁵

	CO ₂	H ₂ O	N ₂	O ₂	CO	NO _x	SO _x
	%	%	%	%	ppm	ppm	ppm
Gas	7.4 - 7.7	14.6	73 - 74	~4.45	200 - 300	60 - 70	-
Coal	12.5 - 12.8	6.2	76 - 77	~ 4.4	50	420	420

Carbon capture and sequestration (CCS) refers to technologies to both capture CO₂ from a point source and store it, thereby preventing it from entering the atmosphere. There are several possibilities for storage of CO₂. Un-minable coal fields are one option for storage; however, there are several requirements that must first be met.⁴ The CO₂ must be adsorbed onto the coal, therefore the coal must have a certain degree of permeability to the gas. Furthermore, there must be a cap rock (impermeable top layer) on the formation to ensure the CO₂ remains trapped. In addition to coal fields, deep saline formations such as the Sleipner project in the North Sea are another option for CO₂ sequestration. In this case, CO₂ is injected into a saline aquifer and entrapped as a liquid due to the high pressure.⁴

But CCS is not only of environmental value; it can also be a profitable venture. As an alternative to storage, if the CO₂ is sequestered reversibly, it can be released on demand for various applications. For example, several chemical processes require CO₂ as a starting material, such as methanol and urea production. Another option for the use of

captured CO₂ is in the area of enhanced oil recovery (EOR). CO₂ pumped down-well can dissolve into the remaining oil making it less viscous and thus easier to extract.⁴

There are several different types of CCS techniques under investigation. These systems utilize absorption, adsorption, membrane diffusion and cryogenic distillation as their mechanism of action. However, each system type has several drawbacks. Some parameters, such as optimal operation temperature, must be considered in the design of a successful system for CO₂ capture. Ideally, the regeneration temperature of the system should be as low as possible to avoid energy penalties associated with regeneration. Furthermore, the loading capacity should be at least comparable to the current industrial standard monoethanol amine (MEA), ~7%,⁶ which will be discussed in detail in the section on absorbents.

Adsorption processes. The adsorption process for the capture of CO₂ is based upon the ability of CO₂ to adsorb into pores and small cracks or onto the surface of the particular sorbent. Simple materials with high surface area such as coal can be used in this process, as is the case when CO₂ is sequestered into un-minable coal fields as previously mentioned. There are two main techniques for CO₂ adsorption, temperature swing adsorption (TSA) and pressure swing adsorption (PSA).⁷ Several factors govern the adsorption rate onto a material: 1) the available surface area of the material; 2) partial pressures of CO₂; and 3) temperature.⁸

As previously mentioned CO₂ can be adsorbed onto coal however, more complex man-made systems such as zeolites, molecular sieves or activated carbons have garnered the attention of researchers due to their high surface areas. There are, however, several drawbacks to an adsorption based system. Primarily is the fact that adsorption processes generally can only handle low concentrations of CO₂ (~ 1% by vol. in gas stream).⁸

Furthermore, water can have a dramatic influence on the adsorption capacities due to competitive adsorption between water and CO₂.⁹

Zeolite based CO₂ scrubbers suffer from many of the same handicaps that have been previously mentioned for the category of adsorption based scrubbers. For example, the presence of even a small amount of moisture in the system can also greatly reduce the CO₂ uptake capacity for zeolite materials. For example, CaX is a class of one of the best performing calcium based zeolites, where X is a ratio of silica to alumina. Its CO₂ uptake capacity is greatly reduced, from 2.5 mmol to 0.1 mmol of CO₂ per gram of adsorbent, with a H₂O concentration change from 1 wt% to 16 wt% respectively.⁹ As previously mentioned, the concentration of water in a flue gas stream is between 6% - 15%.

The adsorption capacities of activated carbons are similar to those of zeolites, but with rapidly decreasing capacities occurring with slight temperature increases. An example is the decrease in CO₂ capacity from 0.75 to 0.1 mmol of CO₂ per gram of adsorbent with only a slight increase in temperature, approximately 80 °C using Ajax activated carbon as the test scrubber.¹⁰ Also in common with zeolites, the adsorption capacities of activated carbons are greatly affected by the presence of water in the system. In one example dry coconut shell carbon was wet during an absorption experiment, leading to a 75% decrease in CO₂ uptake per gram of adsorbent. The reduction due to moisture is only observed at relatively low pressures (< 25 bar), however pressurizing the activated carbon bed to ~25 bar adds a large energy penalty thus increasing operating costs.¹¹

Membrane Separation. There are several different types of membranes in development for the capture of CO₂ utilizing organic, polymeric, solid-liquid, inorganic and metallic materials. The principal governing the function of these membranes is based on size exclusion. The pores can be tailored to the desired size, i.e. just large enough to

allow a CO₂ molecule to diffuse through the membrane. In general, the membrane system is based on a pressure gradient, with low pressure being used to pull the CO₂ through the membrane.⁸

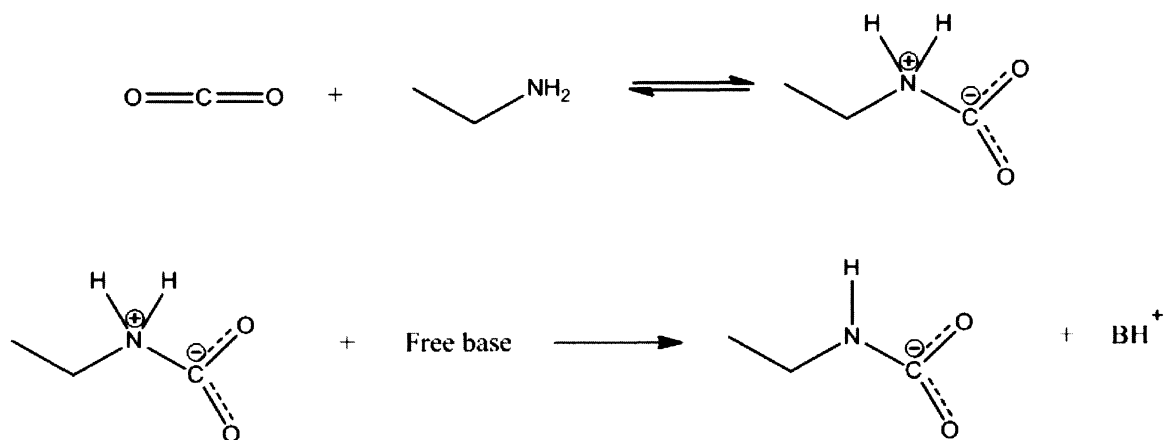
There are some advantages to the membrane system, primarily the simplicity of the system. However there are also several disadvantages, namely the selectivity of the membranes to CO₂. The more selective the membrane is to CO₂, the less permeable it becomes as it eventually becomes saturated and clogged. However, a membrane designed to be more permeable results in a material with less CO₂ selectivity. Furthermore, the membrane material must be strong enough to withstand the pressure gradient across the membrane, which is not the case with many organic membranes. As was discussed for the adsorption system, water can have a large negative effect on the system. Much like zeolites, the concern with water in these membrane systems is that it can clog the pores in the membranes and thus make them less permeable to CO₂.¹² This will be a problem for the large scale separation of CO₂ from a flue gas stream as there is a large amount of water present in the flue gas stream.

Cryogenic Distillation. Another method for the capture of CO₂ from a flue gas stream is based on cryogenic distillation. In order for the cryogenic distillation process to be successful, all of the trace gasses except for N₂ and CO₂ must be removed prior to the start of the process. Once these gasses are removed the N₂ and CO₂ are pumped into a cryogenic chamber. Pressure and temperature manipulation are used to liquefy CO₂ while keeping nitrogen in the gaseous phase. The nitrogen can then be pumped out of the chamber leaving liquefied CO₂.⁴

One big advantage of this process is the form of the CO₂ recovered. The liquefaction makes transport of the CO₂ very simple, it can be pumped through pipelines or loaded into tankers for transportation. Furthermore, the purity of the CO₂ recovered is

usually very high. However, the system has several large drawbacks. Mainly, as is expected the cryogenic distillation is an energy intensive process. The energy required to keep the system cool, usually done with liquid nitrogen makes the overall cost of the system very high and impractical for large scale use. Similar to the other system, water can have a detrimental effect on the process. If any water is present in the stream as it is loaded into the cryogenic chamber it can freeze, which will result in clogging of the lines.¹²

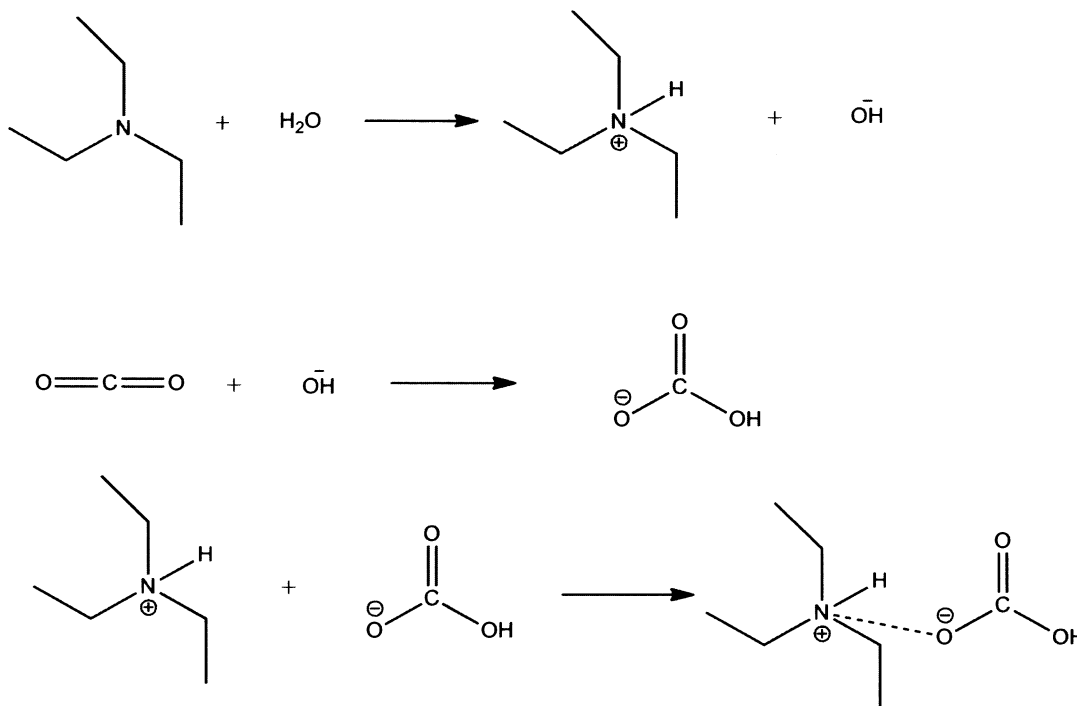
Absorption Processes. The absorption process is based on the interaction of CO₂ with amines by two different reaction pathways. Primary (1°) and secondary (2°) amines react by the same mechanism with CO₂; however, the reaction between tertiary (3°) amines and CO₂ is postulated to be slightly different. Scheme 2.1. illustrates the reaction mechanism between 1° and 2° amines and CO₂.⁸



Scheme 2.1. CO₂ capture mechanism of 1° and 2° amines.

Water also plays an important role in the absorption mechanism of tertiary amines. The mechanism was first proposed by Donaldson and Nguyen in 1980.¹³ In this mechanism the water is dissociated by tertiary amines to form positively charge

quaternary amines. The free hydroxyl then reacts with CO_2 forming a bicarbonate. The bicarbonate then absorbs onto PEI- C_{60} through an ionic bond with the protonated tertiary amine (Scheme 2.2.).



Scheme 2.2. CO_2 absorption mechanism of 3° amines.

Regardless of the types of amines used, there are two main implementation methods for absorption based scrubbers, aqueous deployment and tethering amines to a solid support.⁸ Both systems are based on the reaction schemes shown in Schemes 2.1 and 2.3. In an aqueous scrubber system the free base is H_2O or OH^- or another amine. The function of water as a free base further clarifies the shortcomings of the scrubber systems already mentioned.

In summary, water plays an important role in the absorption of CO_2 by 1° , 2° , and 3° amines in aqueous based and solid phase scrubbers. However, most current technologies other than absorption are negatively affected by the presence of water in the

system making them ill-suited materials for flue gas applications. In the adsorption system, H₂O competes with the CO₂ to be adsorbed, greatly reducing the capacity of the scrubber. The cryogenic process cannot have any water in the system due to the possibility of it freezing and blocking the lines. And in the membrane system it can also clog the pores and reduce the permeability of the membrane. When the overall cost of CO₂ capture is measured as dollars per ton of CO₂ (\$/ton CO₂) captured. In the cryogenic distillation method this cost is \$32.7/ton. When this is compared to the adsorption (\$27.8/ton) and absorption (\$13.9/ton) methods, the cost effectiveness of the cryogenic distillation process is very poor.⁴ There are several different ways to deploy amines for the capture of CO₂, the two most common being tethering them to a solid supports and dispersions in solvents. The current industrial standard involves the dispersion of monoethanol amine (Figure 2.2) in an aqueous solution.

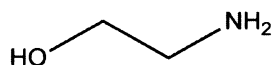


Figure 2.2. Structure of monoethanol amine (MEA).

The gold standard for the large scale capture of CO₂ is monoethanol amine (MEA). MEA is an aqueous based capture technique generally comprised of a 30% solution of MEA in water. While there are advantages to this method, such as scalability, there are also several drawbacks. The CO₂ loading capacity of a general MEA scrubber system is ~7%. While an increase in the concentration of MEA does lead to a higher gravimetric capacity, it also causes the system to become corrosive. The temperature manipulation required for the regeneration of the scrubber system is responsible for up to 70 – 80% of the operating cost of the scrubber system.⁶ Furthermore, as it is a solvent based system, the solution has to be constantly pumped from one tower to another for absorption and regeneration. The solvent used also has to be constantly replaced due to

evaporation, as the system has to be heated to high temperatures ~ 120 °C to regenerate the scrubber. In addition to the cost, solution-based technologies have a high density preventing their use in certain applications such as deployment in aeronautical applications. Current research is focused on finding a more efficient material or process for the large scale capture of CO₂.

The second option for the deployment of amines for CO₂ capture is to tether them to a solid support. There are several different materials that can support amine based sorbents, ranging from mesoporous silica (MPS) to the approach that is taken in this research, tethering to nano-carbon materials. The ideal materials for the anchoring of amines have a large surface area indicating why mesoporous silica and carbon nanomaterials are good candidates.

A variety of amine types have been grafted onto solid supports, these groups include DEA, DETA, TEPA, but the most commonly used is polyethyleneimine (PEI).¹⁴ PEI can be a linear or branched polymer of molecular weights varying from < 600 Da. to $> 800,000$ Da. In the linear form, PEI is terminated with a primary amine group at each end and a chain consisting of secondary amines with ethylene bridges. The branched polymer (Figure 2.3.) can have varying degrees of primary, secondary and tertiary amines depending on synthesis techniques. The general consensus is that the ratio between them is 1:1:1; however, ratios for low molecular weight, commercially available PEI have been reported as 44:33:23 by Jones⁸ and 42:33:25 by Kissel.¹⁵

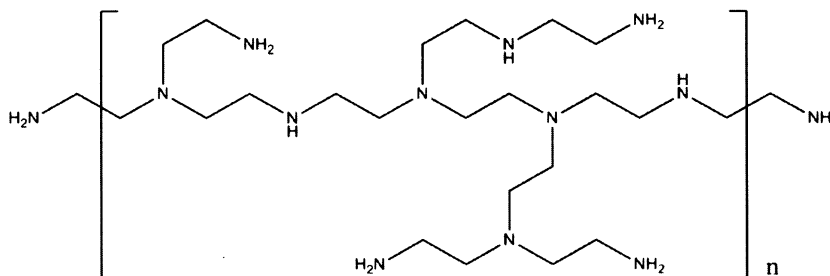


Figure 2.3. Structure of branched PEI.

Regarding MPS specifically, Ahn et al. tethered polyethyleneimine onto a several different silica supports. The highest reported CO₂ capture capacity was for the MPS material KIT-6 impregnated with PEI, at 135 mg CO₂ per gram absorbent. Overall the authors noted that the CO₂ capture capacity of the MPS's was mainly governed by the pore size with the material with the largest pore size (KIT-6) having the highest capacity. Overall the authors graded the capacities of some commonly used MPSs in the following order: KIT-6 > SBA-16 ~ SBA-15 > MCM-48 > MCM-41.¹⁶ Similar to Ahn's work, several other groups have used mesoporous silica, MCM-48, MCM-41, SBA-15, HMS, CMK-5, as a substrate for the tethering of amines.¹⁶⁻¹⁹ The absorption capacities of these are summarized in Table 2.2.

Table 2.2. Summary of the CO₂ capacity of PEI modified mesoporous silica's.

Substrate	CO ₂ capacity mmol CO ₂ /g absorbant
MCM-41	2.52
MCM-48	0.3
SBA-15	2.88
SBA-16	2.93
KIT-6	3.06

In the current work we propose the use of carbon nanomaterials such as SWNT, MWNT, graphitic materials and fullerenes as the solid support for amine-based capture of CO₂. The primary reasons for the choice of these supports are the light weight, large surface areas and reactivity exhibited by carbon nanomaterials. As a result of the larger surface area, larger molecular weights of PEI can be used as compared to MPS's. In the

MSP's, the large surface area is due to a pore system that runs throughout the silica. This pore system means that large molecular weight PEI cannot be used as it will clog the pores. In Ahn's study the highest molecular weight of PEI used was 600 Da. In the current work, because the utilized surface area of the nanomaterials is on the exterior of the structure, large molecular weight (25 kDa.) PEI is not sterically hindered by channels and pores and can access the reactive points on the support structure. We hypothesized that by increasing the molecular weight and branching structure of the polymeric amines on nanocarbon supports we could increase our CO₂ absorbing capacity without greatly increasing the overall mass of the sorbent material. The following is an evaluation of our PEI-nano-carbon systems as CO₂ scrubbers designed for use in a flue gas stream. We will compare CO₂ capacity, regeneration temperatures, scalability, and operational costs of our materials to current technologies.

Results and Discussion

As mentioned in Chapter 1, the branched PEI-SWNT's showed good solubility between the pH ranges 1.7 to 8.31. At any pH above these values aggregation was observed. However, the rate of aggregation was dependent on the source of the basicity. Addition of NaOH solution resulted in aggregate over a period of about 6 hours, whereas addition of NaHCO₃ solution resulted in instantaneous aggregation. This observation is consistent with the CO₂ absorbing qualities of the PEI-SWNT's.

The direct pulse ¹³C MAS NMR spectrum of a sample of PEI(600)-SWNTs (Figure 2.4(a)) shows three signals that can be assigned to the sidewall sp² carbon ($\delta = 122.4$), the aliphatic CH₂ groups of the PEI ($\delta = 47.7$), and a small shoulder at ca. 160 ppm consistent with a carbonyl group. The ¹H-¹³C CPMAS spectrum (Figure 2.4b) suppresses the SWNT sp² signal and allows for the clearer observation of the carbonyl ($\delta = 160.0$). The presence of the carbonyl signal was originally assumed to be due to

residual carboxylate groups on the SWNT, however, several observations suggested otherwise.

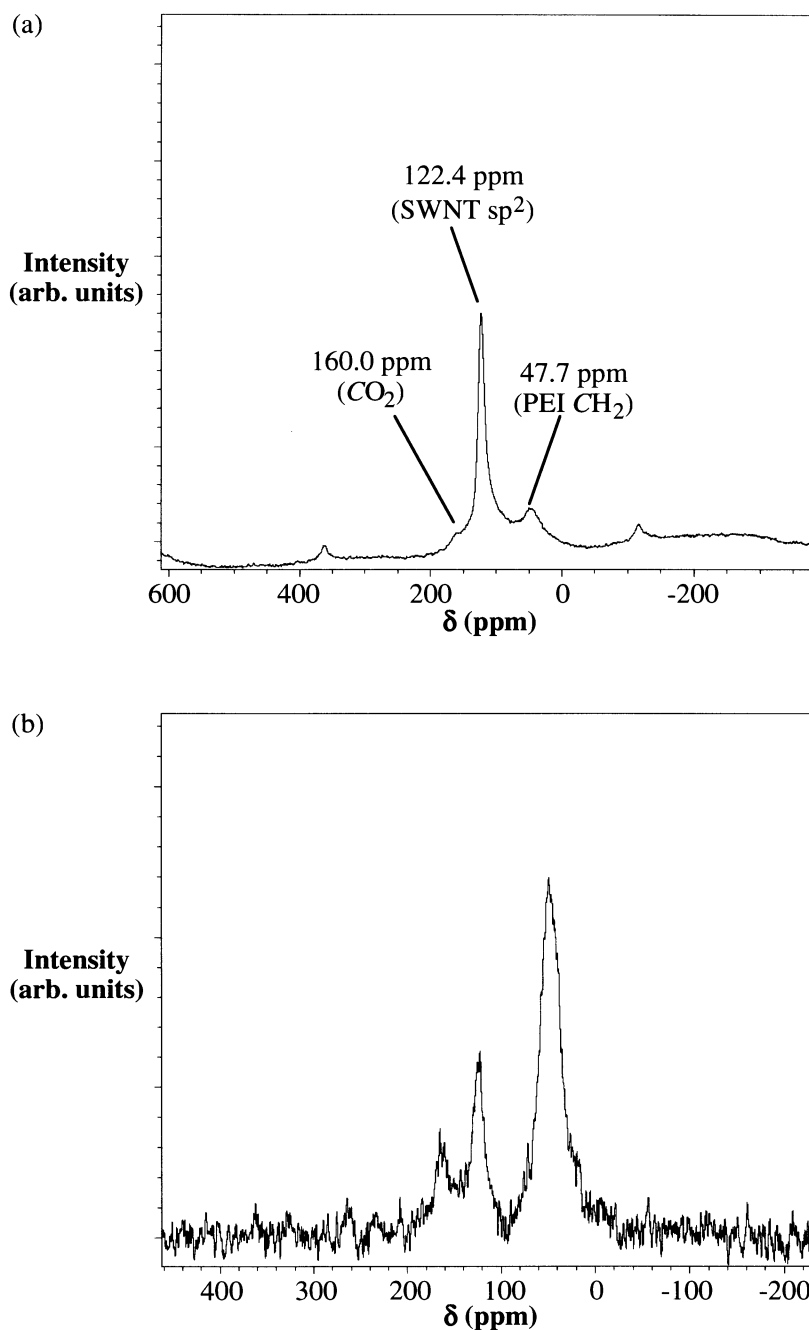
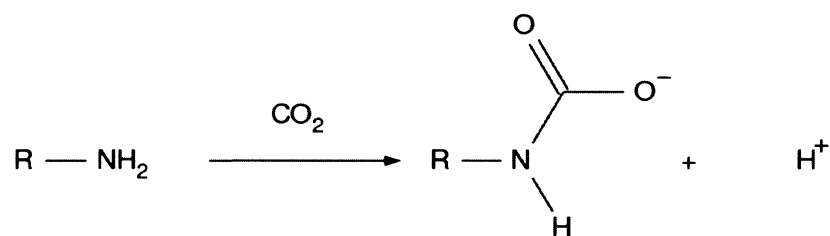


Figure 2.4. Solid state NMR spectra of PEI(600)-SWNTs. (a) ^{13}C MAS NMR spectrum with a 12 kHz spinning speed, and (b) 1H - ^{13}C CPMAS spectrum with a 7 kHz spinning speed.

First, the relative intensity of the peak in comparison with the PEI aliphatic signal suggested a much higher concentration than would be expected. Second, the carbonyl content appeared to be dependent on the age of the sample. Third, the sensitivity to bicarbonate (as compared to hydroxide) suggested a reaction with CO₂. Lastly, PEI is known to react with CO₂ by means of the amines to form a carbamate (Scheme 2.3.).



Scheme 2.3. Reaction of primary amines with CO₂ via carbamate formation.

CO₂ absorption. Due to the results of both the solubility experiments and the ¹³C NMR, we came to the conclusion that PEI-SWNT conjugates are extremely active CO₂ absorbers. Based on that conclusion, the potential absorption of carbon dioxide by the PEI-SWNTs was investigated by TGA. The general method for calculating the CO₂ absorption capacities of the PEI-NC involved heating samples to 75 °C under argon, which resulted in an initial decrease in mass is due the presence of moisture (and ambient CO₂ absorption) in the sample, which will be referred to as the burn-off phase. Once a constant mass was achieved, after the burn-off, the flow gas was switched to CO₂ and the temperature reduced to a set level. As illustrated in Figure 2.5, once CO₂ is introduced, the mass increases significantly until it reaches a stable maximum. When the carrier gas is switched back to argon, a mass loss occurs back to the original mass for the PEI-NC. As is shown in Table 2.3, for a particular experimental temperature, 25 °C, the percentage increase in mass is dependent on the molecular weight of the PEI (in the PEI-SWNT).

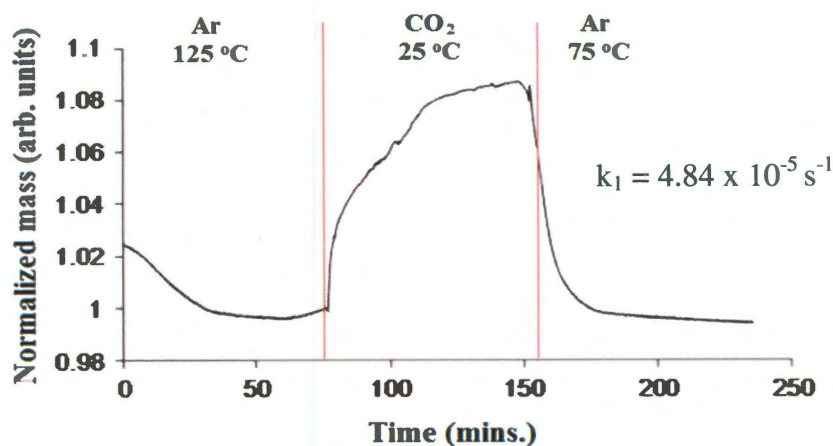


Figure 2.5. TGA of PEI(25000)-SWNT showing the mass change associated with the adsorption and desorption of CO₂.

Table 2.3. Selected physical and spectroscopic data for branched PEI-SWNTs.

PEI M _w (Da)	PEI:C _{swnt}	Raman D:G	CO ₂ absorption mmol CO ₂ /g absorbantt
600	1:155	0.448	0.93
1800	1:405	0.291	1.09
10,000	1:1910	0.281	1.18
25,000	1:2065	0.273	1.93

The ability of the PEI-SWNT to absorb CO₂ should be related to the number and availability of NH₂ groups for reaction. Since the percentage PEI in each PEI-SWNT is known, the efficiency of absorption at a particular temperature can be calculated, i.e., the mass of CO₂ per mass of PEI. Assuming an average molecular weight of each polymer, then a molar efficiency can be estimated that provides an indication of the number of CO₂ molecules adsorbed per polymer unit. Figure 2.6. shows a plot of efficiency as a function of molecular weight of the PEI.

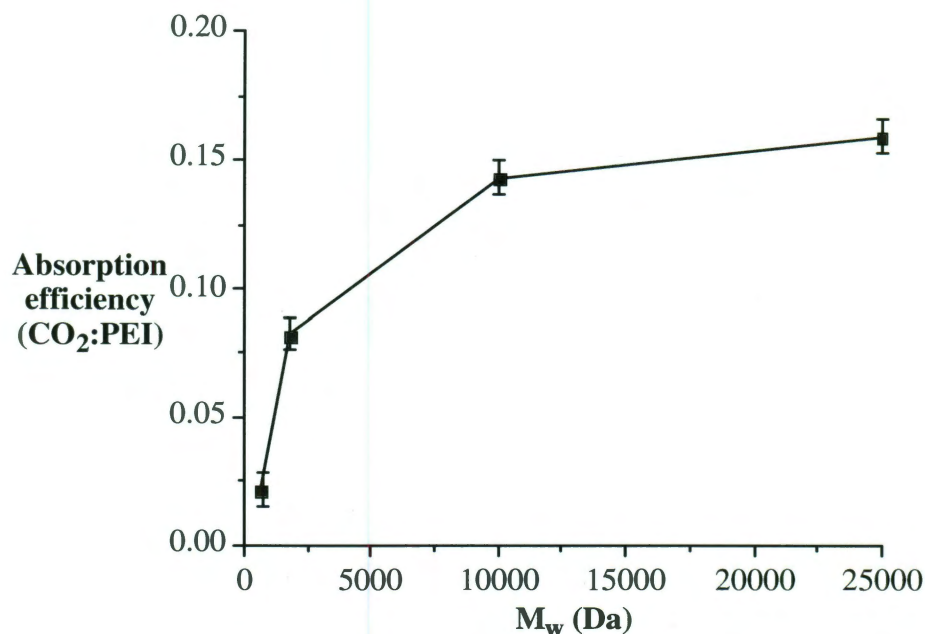


Figure 2.6. A plot of CO₂ adsorption efficiency as a function of molecular weight of the PEI for PEI-SWNTs.

The ability to reversibly absorb CO₂ is an important property for any CO₂ sequestration system. In order to determine the stability of the PEI-SWNTs to absorption/desorption and thermal cycling, samples were repeatedly heated to 75 °C under argon, then cooled to ambient under CO₂. In each case the final mass for both PEI-SWNT and CO₂-PEI-SWNT is within 2% of the previous value showing the stability of the PEI-SWNTs. Furthermore, when the PEI-SWNTs were exposed to CO₂ for extended periods (at a constant temperature) there is no further increase in adsorption (Figure 2.7).

In these experiments the PEI-SWNTs were exposed to 1 atmosphere CO₂ at 75 °C, however, the equilibrium absorption is dependent on the temperature. Figure 2.8. shows the TGA for PEI(10000)-SWNT heated to 110 °C under argon, followed by exposure to CO₂ at a range of temperatures between 75 °C and 25 °C. Clearly as the temperature is decreased the mass reached a new equilibrium.

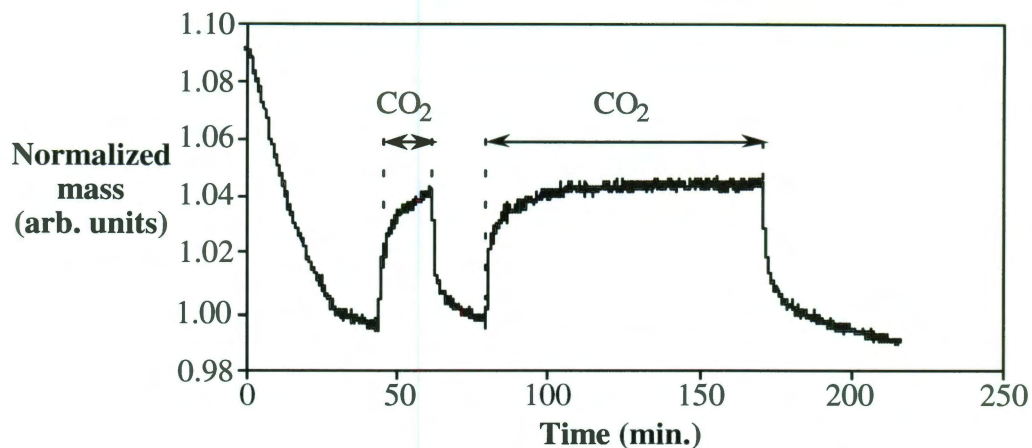


Figure 2.7. TGA of PEI(600)-SWNT showing the mass change associated with the repeated adsorption and desorption of CO₂ irrespective of exposure times. The mass has been normalized to the lowest mass recorded, which is equivalent to PEI(600)-SWNT.

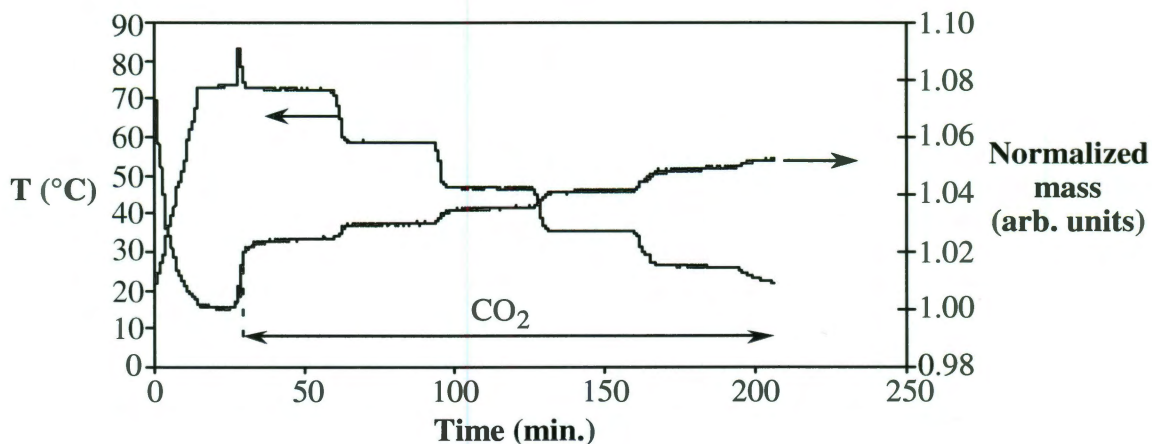


Figure 2.8. TGA for PEI(10000)-SWNT heated to 110 °C under argon, followed by exposure to CO₂ at a range of temperatures showing the increase in CO₂ adsorption with decrease in temperature.

A plot of equilibrium CO₂ adsorption versus temperature is given in Figure 2.9. Based on the data in Figure 2.8. it can be determined that for PEI(10000)-SWNTs complete dissociation of CO₂ occurs at 115 °C even under a CO₂ atmosphere. Investigation of the temperature dependence of the other M_w PEI-SWNTs suggest that

the zero point temperature (i.e., the temperature at which no CO₂ is absorbed) is essentially constant but that as shown above the absolute efficiency is dependent on the M_w.

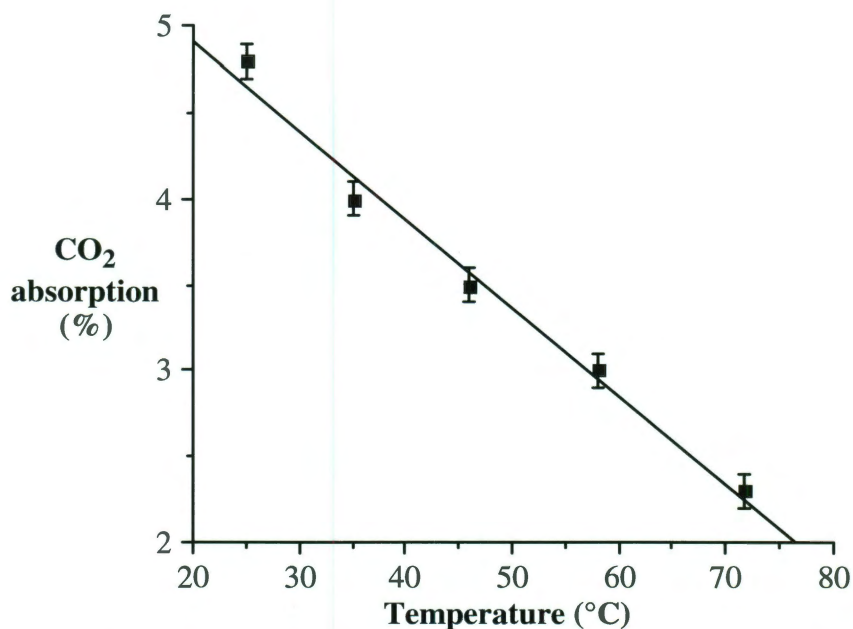


Figure 2.9. A plot of CO₂ adsorption efficiency as a function of temperature for PEI(10000)-SWNT.

These initial studies developed an initial understanding for optimizing the experimental conditions to be used in future experiments (25 kDa.) Furthermore it showed that nanocarbons could be used as a viable substrate for the tethering of PEI for CO₂ capture purposes.

PEI-MWNT. Given the success of PEI-SWNTs as efficient CO₂ absorbers, we wanted to explore other nano-carbons, with a lower cost, as the potential framework of the system. One option to consider as a base carbon material is multi walled carbon nanotubes (MWNT's), as they can be modified in the same way as SWNT's, are produced

in much larger quantities and at a significantly lower cost in comparison to SWNT's. To that end, PEI-MWNTs were prepared using the same synthesis procedure used for the PEI-SWNT's as outlined in Chapter 1.

The CO₂ capacity of the PEI functionalized MWNT's (Bay) is shown below in Figure 2.10. As can be seen from the TGA curve the absorption capacity of PEI-MWNT's is ~ 5%, lower than the capacity achieved with SWNT's. The reason for this is that all the interior layers of the MWNTs are not functionalized and hence add weight to the base nanocarbon without adding functionality. This is not the case with SWNTs as there is only one layer. In addition to the added weight of to the nanocarbon, MWNTs also have a lower surface area in comparison to SWNTs.

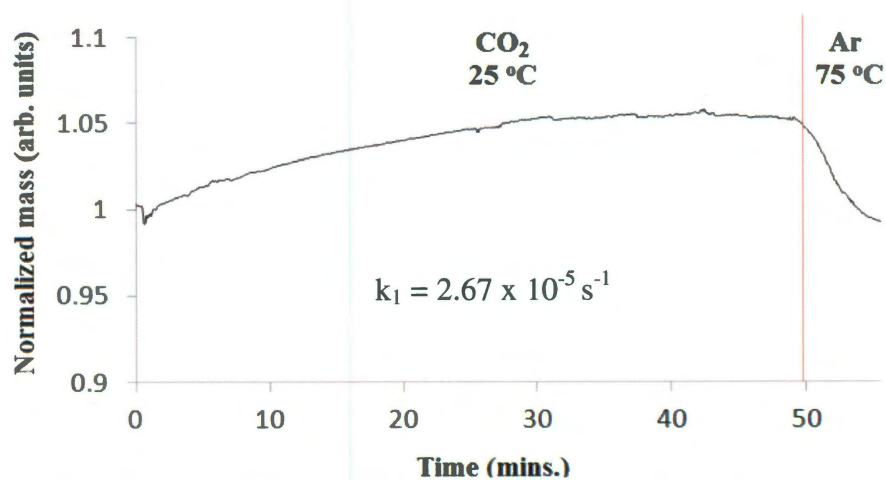


Figure 2.10. TGA showing CO₂ absorption capacity of PEI-MWNT, (~ 5%).

PEI-GIC. Although the PEI-GICs do show uptake of CO₂ (Figure 2.11) the amount is very low (~1%). We believe this is due to the reactivity of the F-GIC and difficulties in controlling the fluorination reaction (discussed in Chapter 1) and hence the PEI content.

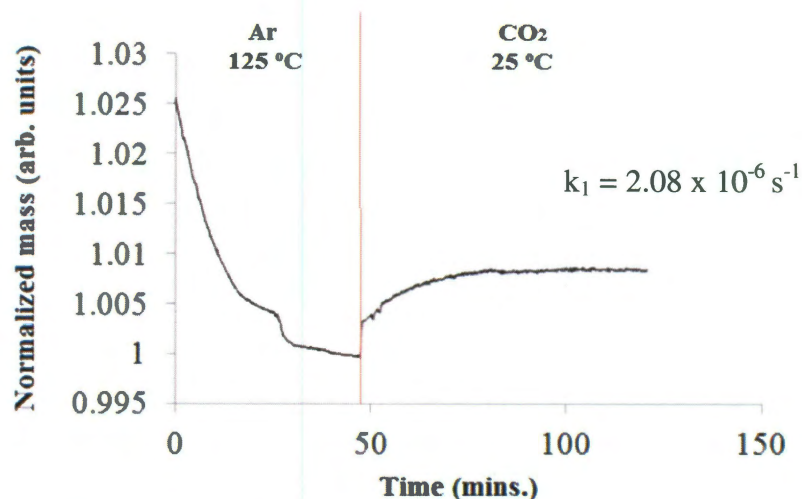


Figure 2.11. CO₂ absorption capacity of PEI-GIC (~ 1 %).

PEI-Phe-(4-N-G). As can be seen from the TGA in Figure 2.12 the absorption capacity is ~ 6%. The CO₂ capacity of PEI-GIC is on the scale of what was achieved with PEI-SWNTs and at least confirmed that graphitic structures could be promising as the scaffold for functional polymers. However, the cost effectiveness of this process is questionable, as several reagents are required to make azido-Phe and to subsequently couple PEI to the carboxylic acid of Phe .

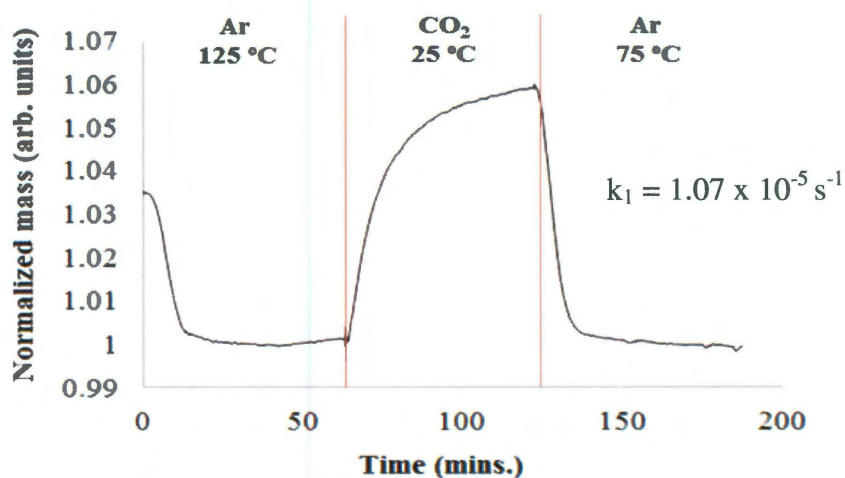


Figure 2.12. TGA curve of PEI-Phe-(4-N-G) showing the CO₂ absorption potential of PEI-Phe-(4-N-G) (~ 6%).

PEI-GO. The potential absorption of carbon dioxide by the 25000 Da. PEI-GO was investigated by TGA. As can be seen from Figure 2.13, once CO₂ is introduced the mass increases significantly until a stable maximum is reached (~8 wt.%). Once the carrier gas is switched back to argon, a mass loss occurs back to the original mass for the PEI-GO. Furthermore, when the PEI-GO was exposed to CO₂ for extended periods (at a constant temperature) there is no further increase in adsorption. In the above experiments the PEI-GO was exposed to 1 atm. CO₂ at 25 °C, however, the equilibrium absorption is dependent on the temperature and pressure, with higher pressure leading to higher uptake.

However, the rate of absorption is slower and the shape of the PEI-GO absorption curve is different to all other absorption runs. This is believed to be caused by the free amines on PEI hydrogen bonding with remaining oxygen containing groups on GO, meaning the breaking of additional hydrogen bonds is required before absorption can occur.

The CO₂ capacity of PEI-GO was very similar to that of PEI-SWNTs (9 wt%) and could be achieved at a significantly lower cost than SWNTs. Although some reagents and processing are required to generate the reactive GO material, the starting materials are of an overall low cost.

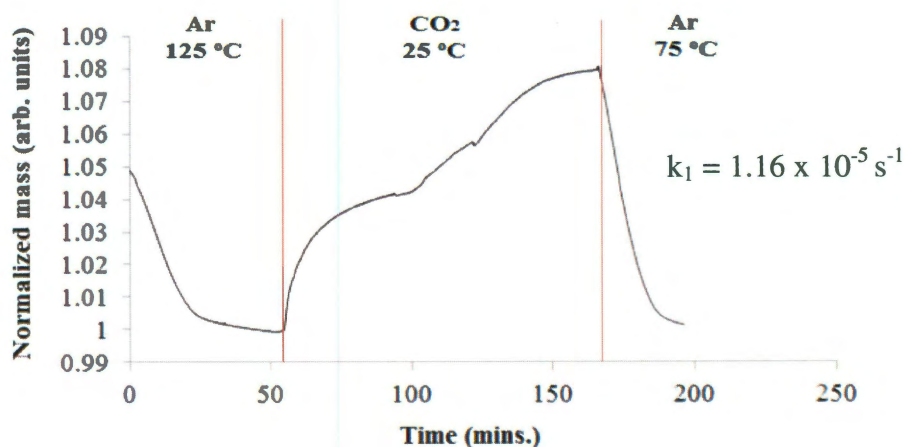


Figure 2.13. CO₂ absorption capacity of PEI functionalized graphite oxide, ~ 8%.

PEI-C₆₀. Figure 2.14 shows the CO₂ absorption capacity of the produced PEI-C₆₀. As can be seen from the graph below, the maximum capacity achieved is ~32% by weight. The curve shows the maximum absorption capacity of PEI-C₆₀, however this experiment was performed using wet CO₂. When the same experiment is done using dry CO₂ the results are markedly different. The dry results are shown below in Figure 2.15.

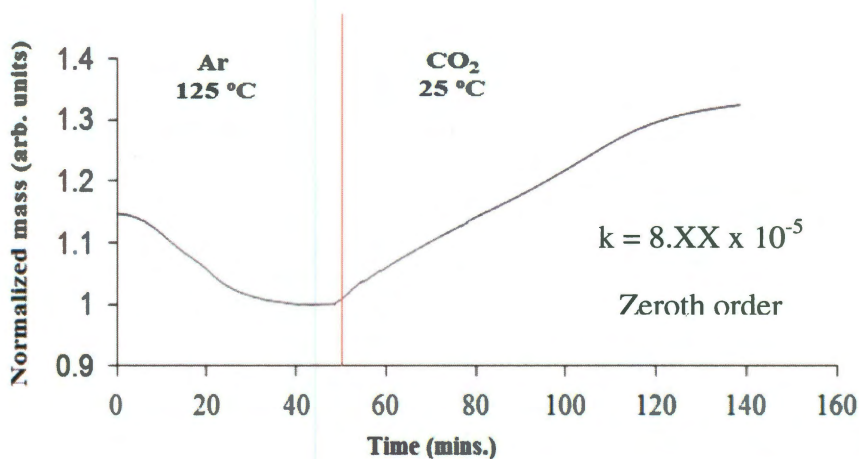


Figure 2.14. TGA curve showing maximum absorption capacity of PEI-C₆₀ (~32%).

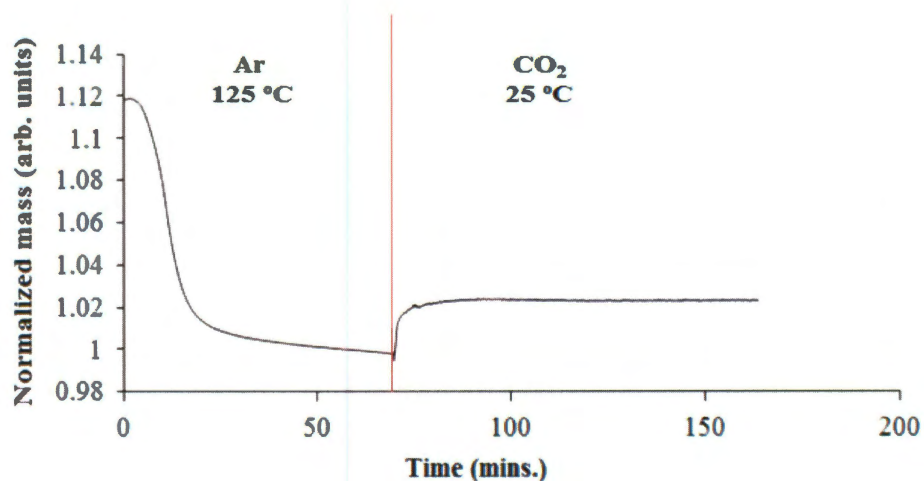
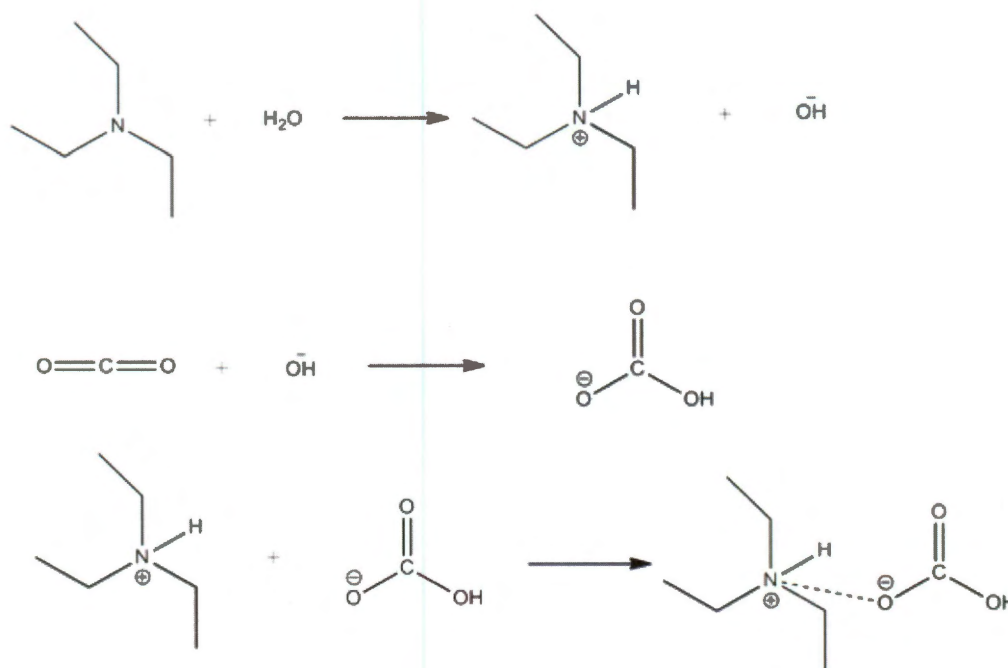


Figure 2.15. TGA curve showing dry CO₂ absorption capacity of PEI-C₆₀ (~3%).

As can be seen from Figure 2.15, the dry absorption capacity of PEI-C₆₀ is ~3%, significantly different to the wet CO₂ absorption capacity. This would indicate that a large amount of the 32% maximum achieved may be due to water absorption. The dramatic water effect makes sense as tertiary amines will absorb CO₂ by first dissociating water and becoming protonated, the hydroxide then reacts with CO₂ to form a bicarb, finally capturing the bicarbonate through an ionic interaction. Primary and secondary amines can also utilize water in their absorption mechanism. The reaction scheme for 3° amines is shown in Scheme 2.4. Interestingly, PEI-MWNTs showed only a small increase of ~ 1% when the absorption conditions were wet. In contrast, the absorption capacity of PEI-C₆₀ increased by ~30%.



Scheme 2.4. Tertiary amine CO₂ absorption mechanism.

In order to determine the true amount of CO₂ captured by the PEI-C₆₀ the amount of water absorbed must be determined. To that end, an argon line attached to a water

bubbler was fed into the absorption chamber without CO₂, however the water was not degassed prior to use. The results of the water absorption experiment are shown in Figure 2.16 indicating that the PEI-C₆₀ absorbs 16% water without the presence of CO₂.

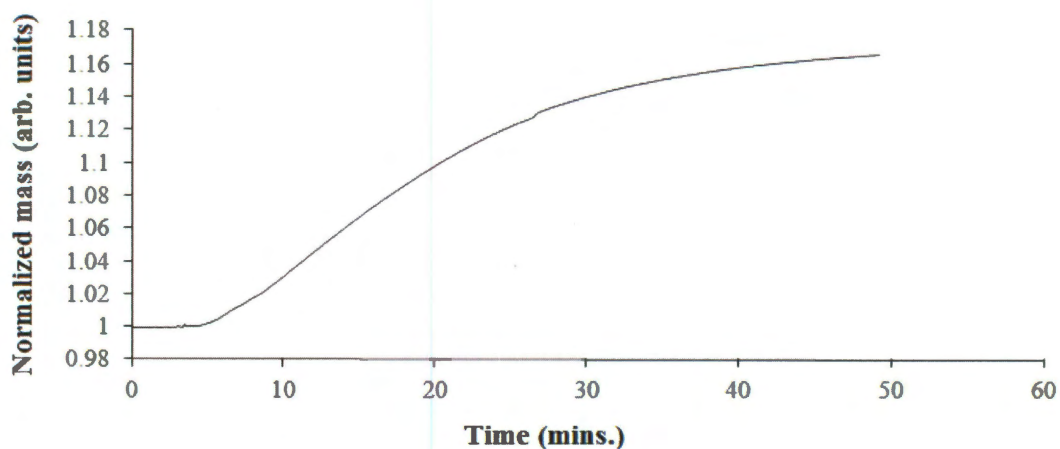


Figure 2.16. TGA curve indicating absorption capacity of water by PEI-C₆₀ (~ 16%).

During CO₂ absorption experiments (wet), the maximum absorption of PEI-C₆₀ peaked at 32%. If 16% of that mass gain was due to water, then 16% was attributable to CO₂. However, the wet argon run, illustrated in Figure 2.16, was performed with water that was not degassed and hence a certain percentage of the mass gain was still due to CO₂. To get a true representation of the amount of water captured, the bubbler water was first degassed using the freeze-pump-thaw method a total of 7 times to ensure all CO₂ was removed from the water prior to the absorption run.

The results illustrated in Figure 2.17 (degassed) indicate that the PEI-C₆₀ absorbs 9% by weight of pure water, with possible CO₂ on the chamber walls of the bubbler. In regards to the CO₂ absorption by PEI-C₆₀, the results indicate that at least 23% of the maximum capacity achieved is CO₂.

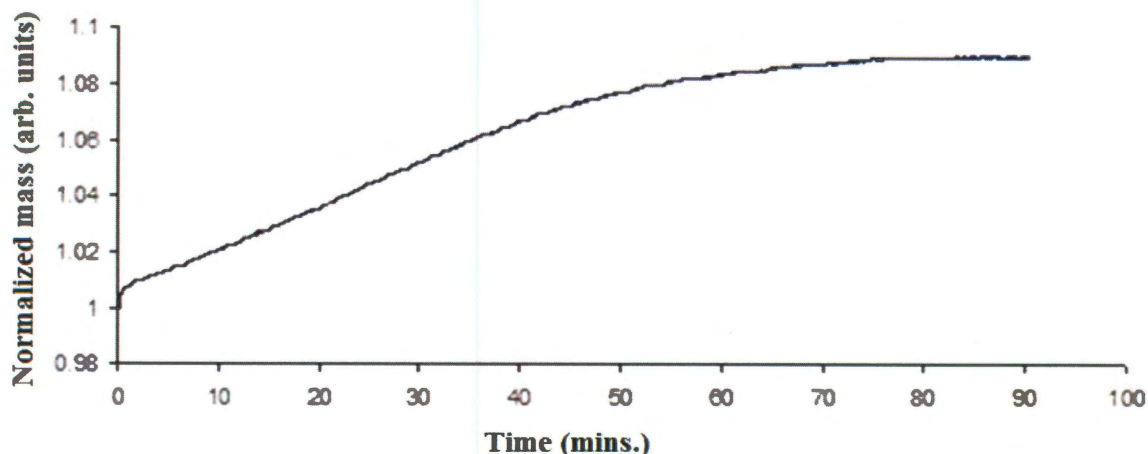


Figure 2.17. TGA curve showing capacity of water absorbed on PEI-C₆₀ using argon with degassed water in a bubbler, (~ 9%).

When these percentages of CO₂ (23%) and water (9%) are taken as a percentage ratio (28.1:71.9 = 2.55) and compared to the molar mass ratio of H₂O and CO₂ (18.01:44.01 = 2.44) we can see that the results are quite similar. This indicates that the possible primary mechanism for absorption on PEI-C₆₀ is via ionic interaction as for each CO₂ molecule captured a water molecule is also captured. The additional mass of CO₂ in the experimental value can be attributed to CO₂ absorption through carbamate formation as water is not necessary for capture by that mechanism, however it can be beneficial as a free base. In keeping with the bicarbonate mechanism where one molecule of water is absorbed per molecule of CO₂ and 32% total absorption, C₆₀-PEI absorbs 5 mmols CO₂/g sorbent. In contrast MEA and MPS absorb 2 and 3 mmol CO₂/g sorbent respectively.⁸

The CO₂ absorption experiments are confirmed by solid state NMR (Figure 2.18.). This experiment was set up such that there was no relative change in intensity between the peaks, therefore relative ratios of PEI and CO₂ could be obtained from the area under the curve. Using this method the absorption capacity of CO₂ on PEI-C₆₀ was calculated to be ~29%, which is similar to that measured by TGA, 23% - 32%,

depending on how much water is captured. The position of the CO_2 peak in the NMR (~ 164.4 ppm) spectrum is shifted when compared to the same CO_2 peak in NMR of PEI-SWNTs (~ 160.0 ppm) by ~ 4 ppm. The cause in this shift could be due to the composition of the substrate, SWNTs versus C_{60} , or the type of capture mechanism, carbamate versus bicarbonate.

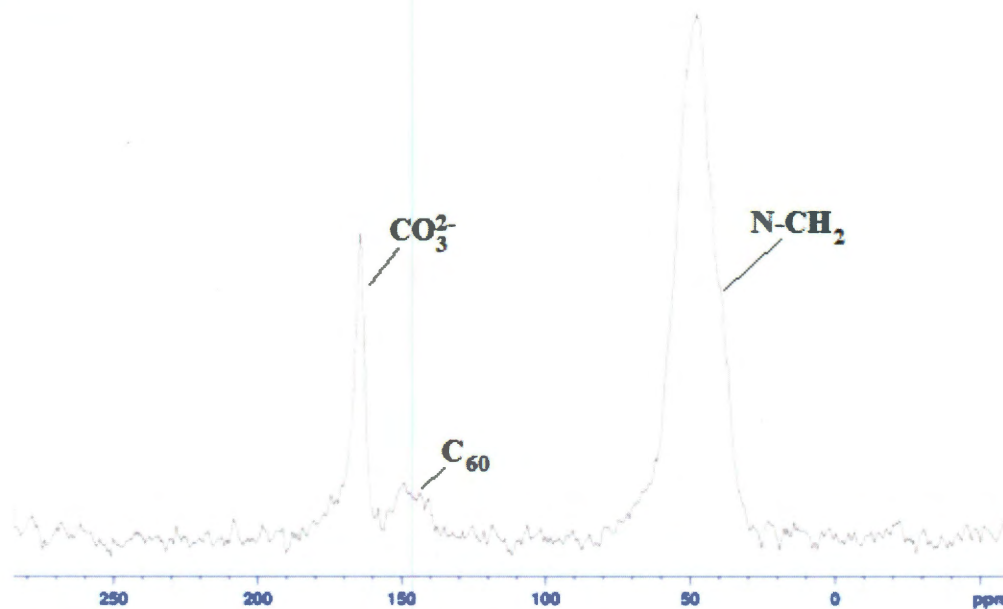


Figure 2.18. Solid state ^{13}C NMR showing the PEI signal at 47 ppm, the fullerene signal 149 ppm and CO_3^{2-} 164 ppm.

In order to determine if it is possible that CO_2 is absorbed by the ionic capture mechanism (Scheme 2.4), ammonium bicarbonate was examined due to the similar bonding interaction. Figure 2.19 shows the solid state ^{13}C NMR of ammonium bicarbonate with the carbonyl peak position measured at 163.48 ppm. This data indicates that the ionic mechanism may be responsible for absorption in PEI- C_{60} , however the carbamate mechanism cannot be ruled out due to possible overlapping of carbamate and bicarbonate peaks.

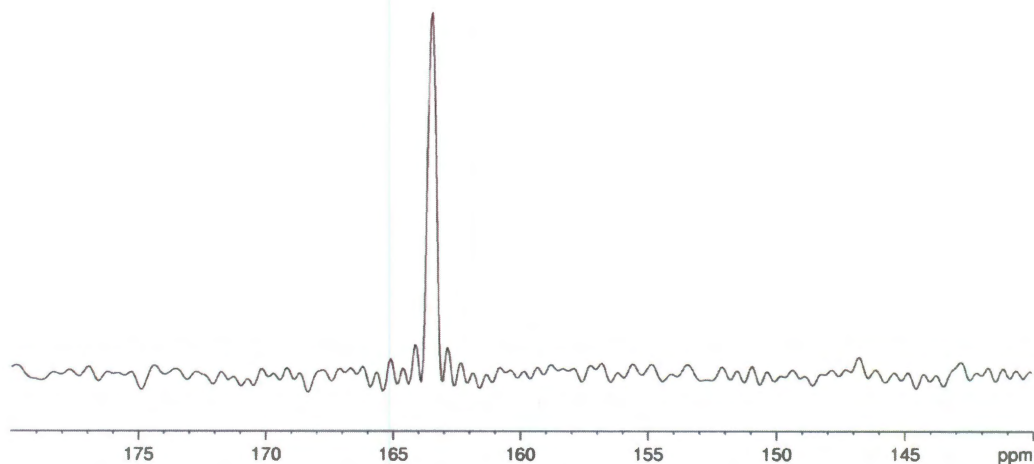


Figure 2.19. Solid state ^{13}C NMR of ammonium bicarbonate with carbonyl peak at 163.48 ppm

Temperature regeneration. The temperature of regeneration for the PEI-GO (75 °C) is significantly lower than we have previously observed for PEI-SWNTs (115 °C) or the MEA process (120 °C). This is an important issue with regard to the economic recovery of the CO_2 . A large energy cost in the MEA process is in heating the water during regeneration. The much lower heat capacity of graphite ($0.71 \text{ kJ}\cdot\text{kg}^{-1}\text{K}^{-1}$) as compared to water ($4.2 \text{ kJ}\cdot\text{kg}^{-1}\text{K}^{-1}$) should further lower the energy cost of regeneration,⁸ and also suggest that other high surface area carbon/graphitic materials should make good substrates. The ability to reversibly absorb CO_2 is an important property for any CO_2 capture system.

An additional advantage of the PEI nanocarbon (PEI-NC) system is that while the regeneration of a MEA system requires temperatures of 120 °C, the regeneration of the PEI-NC systems is 75 °C, significantly reducing the energy burden of the system.

Furthermore, the PEI-C₆₀ can be partially regenerated, ~ 50%, with a simple gas flow, while heating to 75 °C is required for full regeneration of the scrubber. Also of importance is that heating MEA repeatedly causes degradation to the scrubber and thus corrosion of the reaction vessel. We have shown that there is little measurable degradation of the PEI-NC during absorption/thermal desorption cycles. These factors show the ability of the PEI-NC scrubber to overcome the disadvantages associated with solvent based scrubbers while still further decreasing the energy penalty associated with a CO₂ capture system.

Conclusion

In conclusion, the CO₂ absorption capacities of all the PEI-NCs discussed in Chapter 1 were evaluated using TGA. These CO₂ absorption capacities are ranked in the following order, PEI-C₆₀ > PEI-SWNTs > PEI-GO > PEI-Phe(4-N-G) > PEI-MWNTs > PEI-GICs. With PEI-C₆₀ have an absorption capacity of ~ 5.22 mmol CO₂/g absorbent, a value higher than any values reported in the literature for absorption at ambient pressures and temperatures. The overall cost effectiveness for using PEI-NCs make them ideal candidates for use in CO₂ capture projects due to the fact that fullerenes are now produced in large quantities and the regeneration temperatures are lower than those of the current industrial standard.

The rate of absorption, (Table 2.4), of each of the PEI-NCs seems to suggest that the rate may be dependent on the curvature of the NC substrate, with the highest curvature having the fastest rate. Furthermore, PEI-C₆₀ displays a zeroth order absorption rate, meaning both reactants, CO₂ and amines, are in saturation. This is in contrast to all the other PEI-NCs, which display a pseudo first order rate, with CO₂ always being at saturation levels.

Table 2.4. Summary of PEI functionalized NCs properties.

Sample	% NC	% CO ₂	k ₁ (s ⁻¹)
PEI-C ₆₀	40	23	8.12 x 10 ⁻⁵
PEI-SWNT	42	9	4.84 x 10 ⁻⁵
PEI-MWNT	60	5	2.67 x 10 ⁻⁵
PEI-Phe(4-N-G)	43	6	1.07 x 10 ⁻⁵
PEI-GO	57	8	1.16 x 10 ⁻⁵
PEI-GIC	95	1	2.08 x 10 ⁻⁶

Table 2.5. CO₂ capacities of PEI-NCs compared to other amine tethered substrates.

Substrate	CO ₂ capacity mmol CO ₂ /g absorbant
MCM-41	2.52
MCM-48	0.3
SBA-15	2.88
SBA-16	2.93
KIT-6	3.06
PEI-SWNT	1.93
PEI-GO	1.81
PEI-C ₆₀	5.22

In summary PEI-NC display excellent potential for use in the carbon capture field, with PEI-C₆₀ being the best. As can be seen from Table 2.5, PEI-C₆₀ far outperforms any other material for CO₂ capture using tethered amines. Other NCs offer similar capacities to mesoporous silica particles.

Experimental

CO₂ absorption. CO₂ absorption experiments were carried out on a Seiko TG/DTA 200. The general procedure for the absorption experiments is shown below. PEI functionalized NC's (5 – 10 mg) were loaded into an aluminum TGA pan and placed on the balance arm of the TGA. The chamber was sealed and purged with a steady flow of argon (80 sccm). The temperature of the system was ramped from room temperature to 110 °C at a rate of 5 °C.min⁻¹ in order to de-gas and dehydrate the sample. After the mass decrease stabilized to a constant mass the gas in the system was changed to CO₂ (20 sccm). Upon changing gases an immediate increase in weight was observed indicating that the PEI-SWNT's are absorbing the CO₂. The CO₂ flow was continued until constant weight was attained. In order to determine the effects of sample temperature, the sample temperature was adjusted to the desired measurement temperature after a constant weight had been reached. Experiments involving moist CO₂ were performed in the same manner as discussed above, with a stainless steel water bubbler attached between the CO₂ tank and the TGA in experiments involving moist CO₂ capture, and between the argon and TGA in experiments to determine the effects of moisture alone on PEI-C₆₀.

References

1. *United Nations Framework Convention on Climate Change*, http://unfccc.int/kyoto_protocol/items/2830.php, Accessed 5/15/11, 2011.

2. M. S. M. Halmann, ed., *Greenhouse Gas Carbon Dioxide Mitigation Science and Technology*, Lewis Publishers, 1999.
3. *Earth System research Laboratory*, <http://www.esrl.noaa.gov/gmd/ccgg/trends/>, Accessed 5/15/11, 2011.
4. O. D. B. Metz, H. de Coninck, M. Loos, and L. Meyer, ed., *Carbon Dioxide Capture and Storage*, Cambridge University Press, 2005.
5. X. Xu, C. Song, J. M. Andrésen, B. G. Miller, and A. W. Scaroni, *Microporous Mesoporous Mater.*, 2003, **62**, 29.
6. A. B. Rao and E. S. Rubin, *Ind. Eng. Chem. Res.*, 2006, **45**, 2421.
7. A. D. Ebner, M. L. Gray, N. G. Chisholm, Q. T. Black, D. D. Mumford, M. A. Nicholson, and J. A. Ritter, *Ind. Eng. Chem. Res.*, 2011, **50**, 5634.
8. S. Choi, J. H. Drese, and C. W. Jones, *Chem. Sus. Chem*, 2009, **2**, 796.
9. F. Brandani and D. M. Ruthven, *Ind. Eng. Chem. Res.*, 2004, **43**, 8339.
10. D. D. Do and K. Wang, *Carbon*, 1998, **36**, 1539.
11. Y. Wang, Y. Zhou, C. Liu, and L. Zhou, *Colloids Surf. A*, 2008, **322**, 14.
12. D. Aaron and C. Tsouris, *Sep. Sci. Technol.*, 2005, **40**, 321.
13. T. L. Donaldson and Y. N. Nguyen, *Ind. Eng. Chem. Fundam.*, 1980, **19**, 260.
14. D. M. D'Alessandro and T. McDonald, *Pure and Appl. Chem.*, 2011, **83**, 57.
15. A. von Harpe, H. Petersen, Y. Li, and T. Kissel, *J. Controlled Release*, 2000, **69**, 309.
16. W.-J. Son, J.-S. Choi, and W.-S. Ahn, *Microporous Mesoporous Mater.*, 2008, **113**, 31.
17. R. Sanz, G. Calleja, A. Arencibia, and E. S. Sanz-Pérez, *Appl. Surf. Sci.*, 2010, **256**, 5323.
18. M. R. Mello, D. Phanon, G. Q. Silveira, P. L. Llewellyn, and C. M. Ronconi, *Microporous and Mesoporous Mater.*, 2011, **143**, 174.

19. G. Chandrasekar, W.-J. Son, and W.-S. Ahn, *J. Porous Mater.*, 2009, **16**, 545.

Chapter 3

Small Molecule Capture and Release from PEI-SWNTs

Introduction

Pancreatic cancer is one of the most deadly forms of cancer, with a projected survival rate over five years of 5%.¹ The high mortality rate is due mostly to the difficulty in diagnosing pancreatic cancer because the symptoms, such as nausea, and upper abdomen and back pain, are common to many less severe illnesses.² The average survival time after diagnosis with pancreatic cancer is between 3 – 6 months.¹ For this reason, any possible treatments for pancreatic cancer with even moderate success, in animal models, are subject to minimal pre-clinical trials.

The use of percutaneous ethanol injection therapy (PEIT) has been well documented in the successful treatment of hepatic tumors;³⁻⁵ however, there is little precedent for the use of PEIT in the treatment of pancreatic tumors due to the technological limitations of direct injection. Endoscopic ultrasound (EUS) has only become widely used as a therapeutic tool in the past 10 years. Prior to the development of EUS, imaging of the pancreas using external ultrasound was impossible due to fact that the pancreas is buried deep within our digestive system and surrounded by several larger organs such as the liver and stomach. Doctor Manoop Bhutani of U.T. M.D. Anderson Cancer Center, our collaborator, has investigated the feasibility of using an EUS guided probe for the treatment of pancreatic cancer.^{6, 7} The probe allows for ultrasound guided, direct injection of therapeutic agents into the pancreatic tumor.⁸ The pathway for direct injection into the pancreas is shown in Figure 3.1.

The frequency of the sono-endoscope, used for needle placement, can be increased from five megahertz (MHz) for imaging to twelve MHz and focused around the injection site for therapeutic purposes.^{6, 7} A radio frequency probe can also be passed down the instrument channel allowing for ablation of tumor cells, a process that is

already well documented.⁷⁻⁹ Liver cancer is often the result of chronic cirrhosis, or hardening of the liver, which actually seems to protect surrounding hepatic tissue, during PEIT, from the effects of relatively large volume ethanol injections. The tumorous mass is softer than the surrounding cirrhotic liver tissue and the alcohol cannot easily penetrate beyond the malignancy. However, despite the hardening of the surrounding liver tissue, one drawback of PEIT is painful ulcer formation at the injection site.^{10, 11}

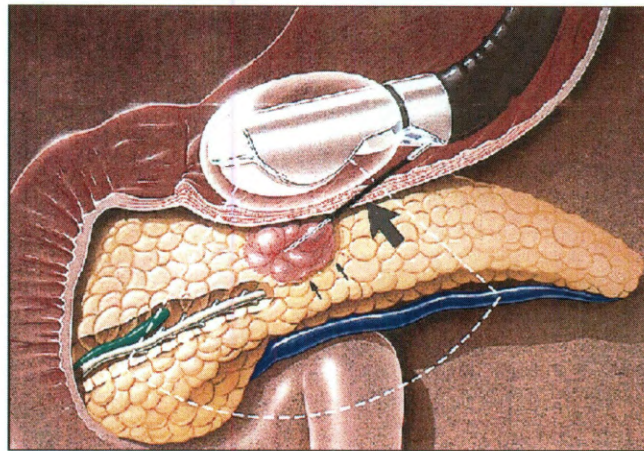


Figure 3.1. Diagram of the pathway of EUS through gastrointestinal tract, for direct injection to the pancreas. Large black arrow shows needle pathway through gastrointestinal tract to pancreas. Small arrows indicate tumorous mass. S. N. Goldberg, S. Mallery, G. S. Gazelle, and W. R. Brugge, *Gastrointest. endosc.*, 1999, **50**, 392.

Since pancreatic cancer is not generally accompanied by hardening of the tissue, large volume injections could be problematic due to the diffusion of alcohol to healthy surrounding tissue. In a 2003 case study reported by Dr. Erwin Gunter et al., a 59 year old man with a gastrointestinal stromal tumor (GIST) was injected with 95% ethanol *via* EUS guided injection. A single injection of 1.5 mL of ethanol was administered directly into the tumor. The patient experienced severe abdominal pain post treatment, and 7

weeks later an endoscopic procedure revealed that a 1.5 cm diameter ulcer (Figure 3.2) had formed at the injection site.¹¹



Figure 3.2. Ulcer formation at ethanol injection site. Ulcer is circled in red. E. Günter, T. Lingenfeller, F. Eitelbach, H. Müller, and C. Ell, *Gastrointestinal endoscopy*, 2003, **57**, 113.

However, there was no longer any sign of the tumor. In the conclusions of the case study, Gunter et al. suggest that if treatment were given in smaller volumes and in multiple sessions, unwanted side effects such as ulcer formation could be avoided.¹¹ Another potential tactic to minimize the unwanted side effects according to Dr. M. Buhtani is to control the release of the alcohol at the tumor site to eliminate the effect of direct injection of large volumes.

The current drug of choice for the treatment of pancreatic cancer is the chemotherapeutic drug Gemcitabine. In the studies conducted gemcitabine was not used as it is and expensive, instead, and analogue for gemcitabine was used, 2-deoxycytidine. The structures of deoxycytidine and gemcitabine differ at the 2' position, with both hydrogens replaced with fluorines, Figure 3.3.

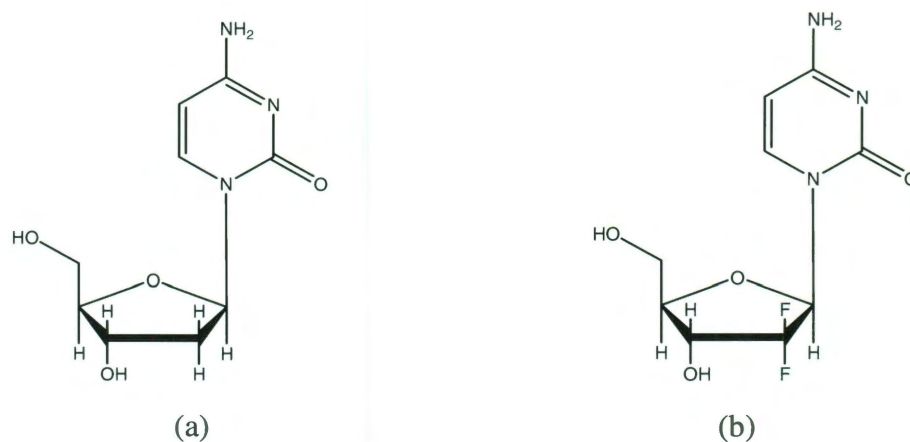


Figure 3.3. Structure of (a) deoxycytidine and (b) Gemcitabine

The function of gemcitabine is to take the place of cytidine during DNA replication in the cancerous cells. When gemcitabine is incorporated to a sequence the next nucleoside will recognize gemcitabine as a faulty residue due to the presence of the fluorine atoms on the sugar ring. The result is termination of DNA replication and therefore cellular apoptosis. Currently gemcitabine is the “drug of choice” in the treatment of pancreatic cancer and administered to the patient intravenously. When a drug is given intravenously a first order kinetic release profile is observed. A first order release profile is not desirable for drug release, as the amount of drug throughout the body varies with the concentration of drug left in the delivery device. In other words, the concentration in the body spikes initially then trails off quickly.

The concentration of Gemcitabine required for the effective treatment of a pancreatic tumor varies depending on the cell line in question and the concentration of a protein called Bcl-2.¹² Figure 3.4. shows the effective concentrations of gemcitabine required to result in the apoptosis of a variety of different pancreatic cancer cell lines.

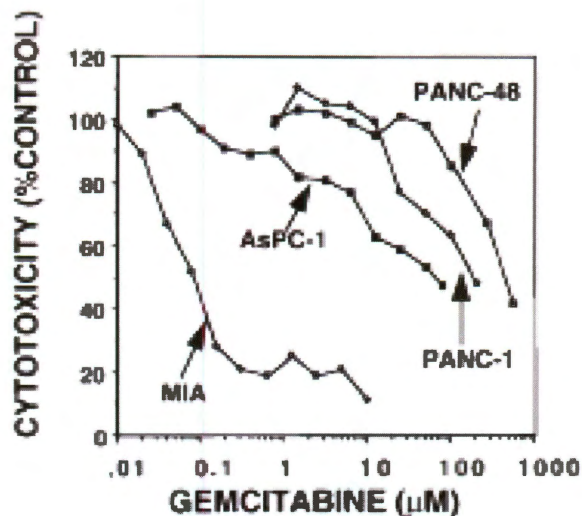
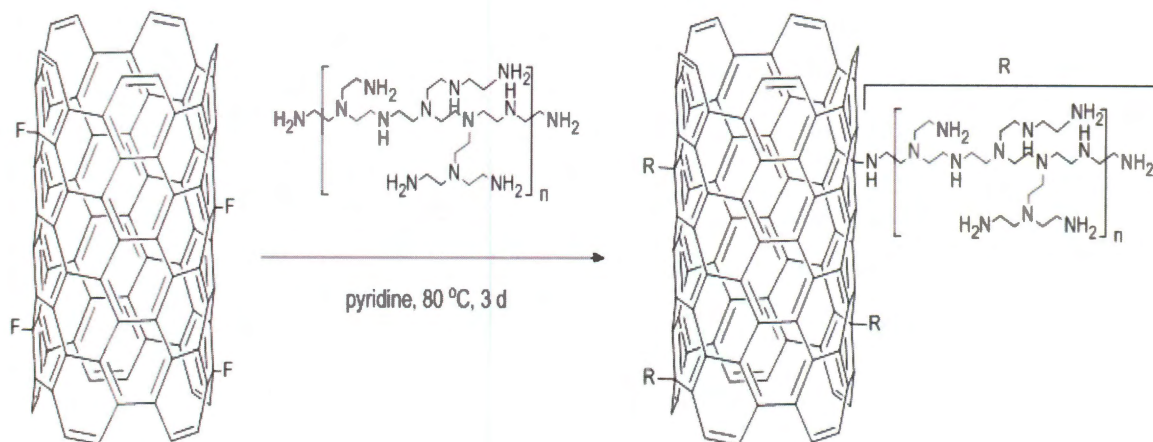


Figure 3.4. Cytotoxicity of various concentrations of gemcitabine against MIA, As-PC-1, PANC-1 and PANC-48 pancreatic cancer cell lines. R. Bold, J. Chandra, and D. McConkey, *Annals of Surgical Oncology*, 1999, **6**, 279.

As can be seen from Figure 3.4 a low concentration of gemcitabine, < 100 μM , is required to achieve a cytotoxic response in three of the four cell lines tested, although the volume is not given. As such a low concentration of gemcitabine is required, it is feasible that this amount of drug could be loaded into PEI-SWNTs and released by sonication. The current work shows the use of polyethyleneimine (PEI) functionalized single wall carbon nanotubes (SWNTs) for the loading of a therapeutic agent within the branched structure of PEI *via* hydrogen bonding. The research will determine the feasibility of gemcitabine and acetic acid release through the use of bath sonication and high intensity focused sonication from the EUS probe at the site of the tumor.

Results and Discussion

Polyethyleneimine functionalized SWNTs were prepared using the method discussed in Chapter 1,¹¹ the reaction scheme for which is shown below in Scheme 3.1.



Scheme 3.1. Reaction mechanism for formation of PEI-SWNTs.

Acetic acid (AcOH) was initially chosen as a test molecule to be loaded into the PEI-SWNTs due to its prior use as a therapeutic to treat cancer.¹³ Additionally, each oxygen atom provides two hydrogen-bonding sites, which makes it an ideal molecule to be encapsulated within the branched amine structure of the polymer. PEI-SWNTs were probe sonicated in glacial acetic acid for a variety of times (5 - 15 min) and allowed to rest in solution post sonication. Loading of acetic acid into PEI-SWNTs was characterized using TGA on the filtered and air-dried loaded SWNTs. The mass loss from the 5 min. sample represents 30% of the overall mass while the loss from the 15 min. sample represents 55% of the total mass. This indicates that the time of sonication is critical to achieve maximum loading of agent into PEI-SWNTs.

Once loaded the PEI-SWNTs were dispersed in water using light bath sonication. The aqueous samples were then brought to our collaborators at M.D. Anderson who allowed us access to an endoscopic ultrasound. The EUS was submerged in the aqueous PEI-SWNT solution for a variety of times (5 - 30 mins) and at two different operating frequencies. The pH of each solution was monitored and as can be seen from Figure 3.5 the pH decreases with sonication time indicating the acetic acid was released with time.

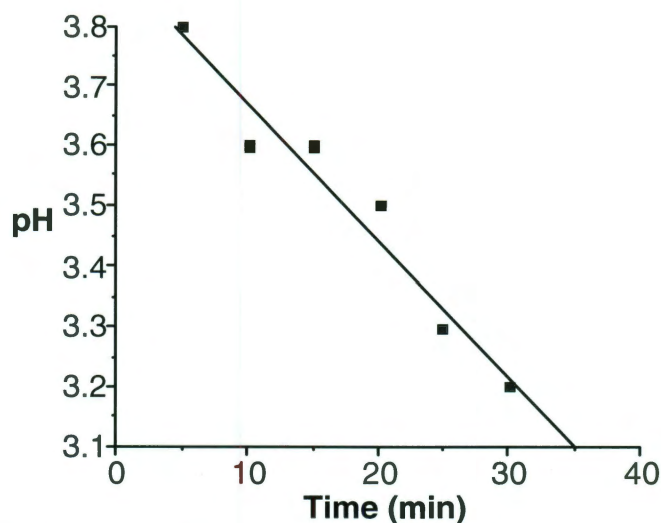


Figure 3.5. Plot of change in pH as a function of EUS exposure time for AcOH-PEI-SWNTs.

The above experiment shows a proof-of-concept of controlled release from PEI-SWNTs using an endoscopic ultrasound. In order to further develop this system deoxycytidine was loaded into the PEI-SWNTs. As mentioned in the introduction, gemcitabine is the current drug of choice for the treatment of pancreatic cancer; however, the drug itself is expensive to test with. As a result, a gemcitabine analogue, deoxycytidine (dC, Figure 3.3a), was used.

Initially, the same loading procedure used for the loading of acetic acid was performed with the dC, however, sonication of dC into the PEI-SWNTs resulted in the PEI-SWNTs crashing out of solution. In order to overcome this problem it was decided that the drug delivery system be modified to deliver the drug as a suspension, again as a proof-of-concept that the drug release from the polymeric support can be controlled through sonication. Given the solubility issue, this specific PEI construct could not be used in biological applications. The alternate loading method for PEI-SWNTs is explained in the Experimental. To that end, PEI-SWNTs were loaded with deoxycytidine, such that the concentration of deoxycytidine will be 100 μM in the release vessel

assuming 100% loading. Once loaded the PEI-SWNTs were recovered via vacuum filtration through a 200 nm pore size PTFE filter. The product was not washed, as washing could remove some of the loaded drug. One mL of deionized water was added to the solid product (~ 4 mg) forming a dilute suspension and transferred to a dialysis membrane. The membrane will allow the drug to pass through but not the PEI-SWNTs. The release of dC can be monitored using ultra violet spectroscopy with the peaks from dC appearing at 196 nm and 271 nm. During our release experiments the UV peak of deoxycytidine at 271 nm was monitored. Figure 3.6 shows the release profile of deoxycytidine from PEI-SWNTs.

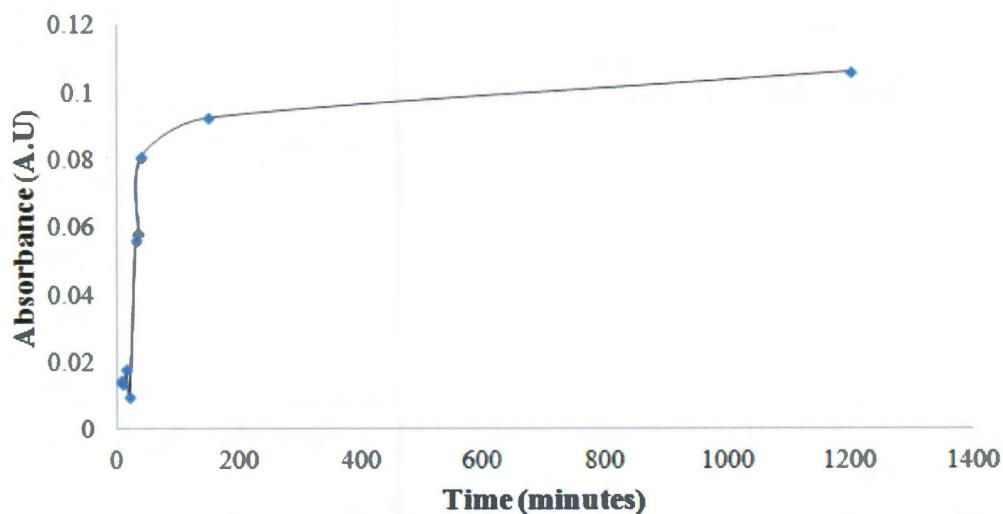


Figure 3.6. Release of deoxycytidine monitored by UV-vis spectroscopy (271 nm).

Sonication was started at $t=20$ min in the above curve.

During the initial portion of the release, the dC/PEI-SWNT suspension in the dialysis membrane was submerged in the release solution for a period of time before stirring began, 10 minutes. Samples were collected for analysis before and after stirring began, before and after sonication began, and after 20 hours of prolonged sonication.

Care was taken to maintain a constant volume of water throughout the release experiment. As can be seen from the release curve, there was a large burst release within the first hour after sonication. However, even at the last time point the concentration of dC was still increasing, albeit at a much slower rate than the initial portion. This indicates that the polymer was able to form a strong enough interaction with the drug to contain it to a degree despite constant sonication. When we look in more detail at the results of the release experiments it can be seen that the sonication has a large effect on the release of dC (Figure 3.6), sonication began after the third time-point and was continued throughout. This is what is expected as the sonication will cause swelling of the polymer and provide enough energy to break any hydrogen bonds that have been formed between deoxycytidine and PEI.

As stated previously the PEI-SWNTs were loaded with deoxycytidine so that a maximum release would be $\sim 100 \mu\text{M}$ in the 300 mL release vessel. However the maximum concentration released has an absorbance of 0.105, when this is compared to our calibration curve the maximum concentration released is $\sim 10 \mu\text{M}$. This indicates that only about 10% of the added deoxycytidine was loaded into the PEI-SWNTs. The actual mass of dC loaded into the tubes was $\sim 680 \mu\text{g}$, resulting in a loading of $\sim 18\%$.

Conclusions

In conclusion, it has been shown that PEI-SWNTs can be loaded with therapeutic agents such as acetic acid and the Gemcitabine analogue, deoxycytidine. The amount of loading of acetic acid is based on initial sonication time, with a longer sonication time leading to a higher degree of loading. It has also been shown that sonication can release the therapeutic from within the branched network of PEI-SWNTs. Two different types of sonication were effective for release, sonication from the focused ultrasound in aqueous solution and bath sonication for release from a suspension in a membrane. The drug

loading of PEI-SWNTs was ~18% by mass, a potentially effective therapeutic does based on *in vitro* studies.¹²

The overall conclusion is that, due to their solubility issues, PEI-SWNTs cannot be utilized in biological applications. Despite their water solubility, they eventually crash out of PBS solutions. However, given our ability to initiate the drug release with sonication from a polymeric-NC material, we do believe that the polymer-nanotube conjugate still has potential as a drug delivery vector. However, once the polymer chain “opens” there is no way to stop the release. Replacing PEI with a water soluble thermo-responsive polymer may make the ideal vector for the controlled release by endoscopic ultrasound.

Experimental

Acetic acid and deoxycytidine were purchased from Sigma Aldrich, Inc., and were used as received. The AcOH release was monitored with a pH meter and the dC release was monitored by UV with a Agilent Ultraviolet-Visible spectrophotometer. The release of AcOH was achieved with Dr. Manoop Bhutani’s EUS instrument at M. D. Anderson while dC release was achieved with an bath sonicator.

AcOH loading. Glacial acetic acid was loaded into PEI-SWNTs by the sonication of PEI-SWNTs in a solution of glacial acetic acid. The product was recovered *via* filtration through a 0.2 μm PTFE filter. Product was added to water (mg/mL), followed by light bath sonication in water for solubilization. Degree of loading was calculated by TGA with a ramp to 200 °C at 5 °C per minute, mass loss was attributed to acetic acid.

AcOH release. The release of acetic acid by EUS stimulation was performed at M. D. Anderson Cancer Center under the supervision of collaborator Dr. Manoop Bhutani. The head of the EUS was submerged in a 10 mL solution of loaded PEI-

SWNTs. At time intervals of 5 minutes the pH of the solution was analyzed with a pH probe and the results recorded.

Deoxycytidine Release. Deoxycytidine was loaded into PEI-SWNTs by the addition of deoxycytidine to 10 ml of PEI-SWNT followed by bath sonication for 30 minutes. Following sonication the samples were placed in the fridge, resulting in precipitation of PEI-SWNTs from solution. Sample was then filtered through a 0.2 μm pore size PTFE filter, the sample was not washed. The powdered sample was added to a dialysis bag as a suspension, with 1 ml of water for release.

References

1. R. M. Lag, D.; Krapcho, M.; Mariotto, A.; Miller, B. A.; Feuer, E.J.; Clegg, L.; Horner, M.J.; Howlader, N.; Eisner, M. P.; Reichman, M.; Edwards, B. K. (eds). "SEER Cancer Statistics Review, 1975-2004" National Cancer Institute. Bethesda, MD, http://seer.cancer.gov/csr/1975_2004/, based on November 2006 SEER data submission, posted to the SEER web site, 2007., 1975-2004.
2. H. E. Adamek, J. Albert, H. Breer, M. Weitz, D. Schilling and J. F. Riemann, *The Lancet*, 2000, **356**, 190-193.
3. T. Livraghi, *Journal of Hepato-Biliary-Pancreatic Surgery*, 2003, **10**, 67-76.
4. T. Livraghi, A. Giorgio, G. Marin, A. Salmi, I. de Sio, L. Bolondi, M. Pompili, F. Brunello, S. Lazzaroni and G. Torzilli, *Radiology*, 1995, **197**, 101-108.
5. P. J. Johnson, *HPB: The Official Journal of the International Hepato Pacreato Biliary Association*, 2005, **7**, 50-55.
6. M. S. Bhutani, *Endoscopy*, 2003, **35**, S45,S48.
7. M. S. Bhutani, *Endoscopy*, 2003, **35**, S54,S56.
8. S. N. Goldberg, S. Mallery, G. S. Gazelle and W. R. Brugge, *Gastrointestinal endoscopy*, 1999, **50**, 392-401.
9. S. Curley, *Annals of Surgical Oncology*, 2003, **10**, 338-347.

10. H. Aslanian, R. R. Salem, C. Marginean, M. Robert, J. H. Lee and M. Topazian, *Gastrointestinal endoscopy*, 2005, **62**, 723-727.
11. E. Günter, T. Lingenfelser, F. Eitelbach, H. Müller and C. Ell, *Gastrointestinal endoscopy*, 2003, **57**, 113-115.
12. R. Bold, J. Chandra and D. McConkey, *Annals of Surgical Oncology*, 1999, **6**, 279-285.
13. K. Ohnishi, H. Yoshioka, S. Ito and K. Fujiwara, *Hepatology*, 1998, **27**, 67-72.

Appendix A

T. A. Strom, E. P. Dillon, C. E. Hamilton, and A. R. Barron, *Chem. Comm.* 2010, **46**, 4097-4099 .

Nitrene addition to exfoliated graphene: a one-step route to highly functionalized graphene†

T. Amanda Strom, Eoghan P. Dillon, Christopher E. Hamilton and Andrew R. Barron*

Received 22nd January 2010, Accepted 22nd April 2010

First published as an Advance Article on the web 10th May 2010

DOI: 10.1039/c001488e

We demonstrate a high yield method of functionalizing graphene nanosheets through nitrene addition of azido-phenylalanine [Phe(N₃)] to exfoliated micro-crystalline graphite (μG). This method provides a direct route to highly functionalized graphene sheets. TEM analysis of the product shows few layer ($n < 5$) graphene sheets. The product was determined to have 1 phenylalanine substituent per 13 carbons.

Recent years have brought about a renewed interest in graphite or specifically individual or few-layer ($n < 5$) sheets of graphite called graphene. The unique physical and electronic properties of graphene make it attractive as a substitute for other more costly carbon nanostructures.¹ Due to its similarities and differences with other carbon nanostructures, graphene (2 dimensional, 2D) is no longer the underappreciated parent of fullerenes (0D) and carbon nanotubes (1D). The ability to individualize sheets of graphene has brought the material to the forefront of carbon research.² And while graphene does provide similar scale, properties, and reaction pathways as fullerenes and CNTs, it does so at a fraction of the cost. Regardless of the novel electronic properties of graphene, it also presents an inexpensive, large surface area scaffold for the covalent attachment of organic molecules. Covalent functionalization provides a robust material for use as a scaffold and as a means of incorporating additional functionality. Incorporation of functionalized graphene sheets into composite materials may enhance mechanical and electronic properties. The majority of reports of covalently functionalized graphene use graphene oxide (GO) as the starting material.³ While the structure of GO has been shown to include regions of unoxidized benzene rings, the presence of islands of epoxides and hydroxyl groups on the basal plane and carboxylic acids around the perimeter of the sheet make GO extremely hydrophilic. In addition, graphene oxide contains a large percentage of water requiring more than four weeks to dry post synthesis.⁴ While this method does result in highly functionalized graphene sheets, the drawbacks are that reactions using GO as the starting material are limited to aqueous or polar conditions and more important a second reduction step is necessary to remove the excess oxides still present.³ A simpler route to widespread functionalization is therefore

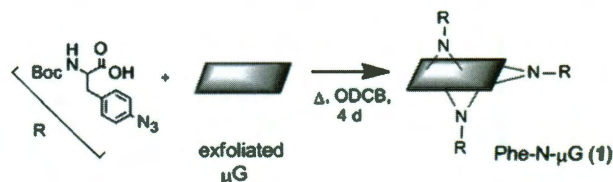
desirable. In this regard, we report a new, high yield method of covalently functionalizing graphene sheets.

It has been shown that both CNTs and fullerenes are easily functionalized by nitrene addition, generated *in situ* by thermal decomposition of azido starting materials.⁵ The result is high density functionalization of the nanostructure surface through a [2+1] cycloaddition to the C–C double bonds forming an aziridino-ring linkage, however; this methodology has only been applied to curved or strained (*i.e.* reactive) carbon nanostructures. The alkyl and aryl azido starting materials are easily synthesized on the gram scale and azides offer a wide range of functional group tolerance.⁶ For our purposes, the azido moiety resides on the R side chain of the amino acid phenylalanine (Phe) allowing incorporation of two new chemical handles on the graphene scaffold for subsequent reaction. In this regard, the graphene sheet could be used as a solid support for solid phase peptide synthesis (SPPS) of a sequence on the graphene surface. The addition of sequences of amino acids to the graphene surface should impart water solubility and some level of biocompatibility.

In a typical reaction,‡ microcrystalline graphite (μG, <20 μm, 50 mg) was exfoliated without homogenization in *o*-dichlorobenzene (ODCB, 20 mL) to make a clear gray solution of graphene sheets without the use of harsh oxidizing conditions.⁷ It is worth noting that this reaction was not reproducible using thermally expanded graphite intercalation compounds (GIC)⁸ as the starting material. Given that GICs use a variety of reactive molecules to intercalate between graphene layers,⁴ side reactions with reactants are inevitable, thus limiting their use as graphitic starting materials as well. The exfoliated μG was reacted with Boc-Phe(4-N₃)-OH§ at refluxing temperatures. The reaction was filtered over a 0.2 μm PTFE filter paper, and washed to remove any unreacted Phe(N₃) (Scheme 1, yield 1 110 mg). The product 1 was found to make an amber colored solution in DMSO, averaging 0.06 mg mL⁻¹ after 10 min of probe sonication and centrifugation (3400 rpms for 15 min). The product also proved sparingly soluble in other organic solvents such as DMF, toluene, and chloroform in comparison to the μG starting material. To confirm the chemical modification FTIR spectroscopy, Raman spectroscopy, and XPS were utilized.

Richard E. Smalley Institute for Nanoscale Science and Technology, Center for Biological and Environmental Nanotechnology, and Department of Chemistry, Rice University, Houston, Texas 77005, USA. E-mail: arb@rice.edu; Web: www.rice.edu/barron; Tel: +1-713-348-5610

† Electronic supplementary information (ESI) available: Details of the synthesis; XPS, IR, TGA, and additional TEM, AFM, and STEM images. See DOI: 10.1039/c001488e



Scheme 1 Nitrene addition to exfoliated μG in refluxing ODCB.

The elemental composition of **1** was determined by XPS, confirming the presence of the phenylalanine (Fig. S1, ESI†). The oxygen (16.1%) and nitrogen (13.5%) content are consistent with the presence of the phenylalanine substituent with the expected loss of the Boc protecting group which can occur at 180 °C.⁹ However, the FTIR of **1** (Fig. S3, ESI†) showed the characteristic absorption of a secondary carbamate carbonyl stretch at 1655 cm⁻¹, indicating there was only partial loss of the Boc protecting group. In addition, the spectrum shows absorption in the carboxylic acid (~3200 cm⁻¹ stretch and 1438 cm⁻¹ bend) and the amide C–N regions (1319 cm⁻¹) relative to the μG starting material. Also present in the spectrum are the NH stretch (3426 cm⁻¹) of the Boc amino protecting group and the prominent C–N amine stretch at 1022 cm⁻¹ of the aziridino linkage.

High resolution TEM images show graphene sheets layered over each other, with an average length of 300–500 nm and with varying widths (Fig. 1). This is in agreement with STEM measurements (Fig. S6, ESI†), in which large, few-layer graphitic domains are visible. The formation of few- or multi-layer sheets is further supported by selected area electron diffraction (SAED, Fig. 1 inset and Fig. S4, ESI†) and fast Fourier transform (FFT, Fig. S4, ESI†) in selected areas.

The AFM analysis confirmed the presence of graphene sheets with a wide variety of lateral dimensions from 150 nm to > 5 μm. The thickness of the observed sheets ranged from 0.5 nm to ~2.5 nm (Fig. 2). The theoretical height of our Phe functional group is ~0.75 nm, correlating to the addition of 1.5 nm to the thickness of the graphene sheet if functionalization occurs on both sides. Several groups have reported a height of ~1 nm for GO sheets with some variability.^{10–12} Our analysis of **1** shows a variety of sheet thicknesses, however, we surmise that the thinnest sheets, 0.5 nm, are only edge functionalized while the thickest at 2.5 nm are basal plane functionalized on both sides. Based on both the TEM and AFM characterization, we conclude that few-layer (*n* < 5) graphene sheets are produced by this reaction method.

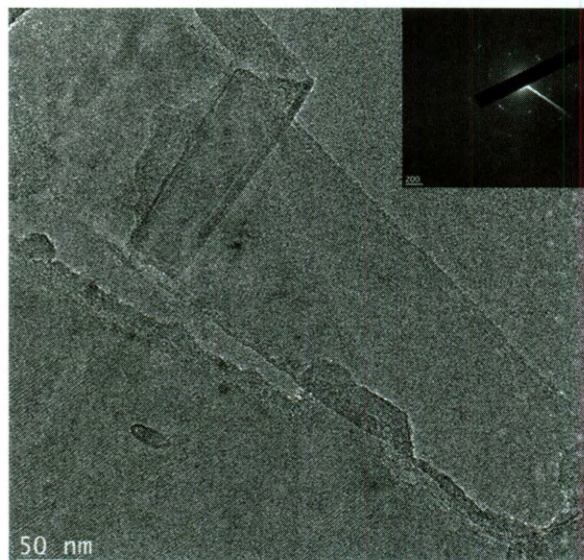


Fig. 1 TEM image of Phe–N–μG (**1**) showing stacked, few layer, sheets with SAED inset confirming few-layer graphene sheets.

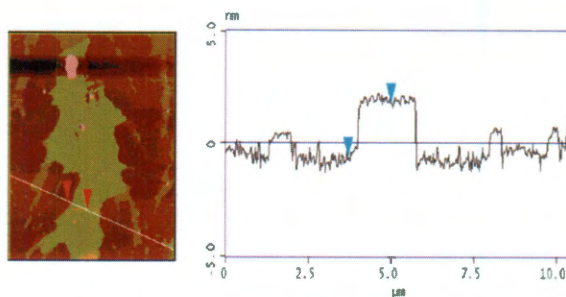


Fig. 2 AFM image and associated height profiles of Phe–N–μG (**1**), spin coated on a cleaved mica substrate from CHCl₃, showing a large graphene sheet surrounded by smaller graphene flakes.

Scanning TEM (STEM) images of **1** (Fig. S6, ESI†) deposited from DMSO on a lacey carbon grid show few-layer sheets, the majority of which had lengths of over 1 μm and widths of about 500 nm. However, some sheets were as small as 150 × 300 nm, in agreement with TEM and AFM measurements.

The extent of functionalization is obtained from thermogravimetric analysis (TGA) over the temperature range of 130–850 °C in agreement with the decomposition of phenylalanine (Fig. S7, ESI†). Assuming no mass loss due to μG and taking into account the carbonaceous material remaining from phenylalanine (Fig. S7–S8 and discussion, ESI†), the final product **1** was determined to be 69% phenylalanine (wt%). This corresponds to one Boc–Phe substituent per 10 μG carbons (XPS data show 1 : 13 C : Phe, Fig. S1, ESI†). It should be noted, however, that each Phe substituent is bonded to two carbon atoms (Scheme 1). It has been shown previously that graphene is preferentially functionalized along its edges.¹¹ However, even with the smallest sheets of **1** (150 × 300 nm by STEM), if the functionalization is limited to the edges, only 2–3% by mass of the sample is attributable to Phe. Assuming the entire mass loss by TGA is due to covalently bonded Phe, to achieve 69% by mass functionalization of **1**, the nitrene addition could not occur solely at the edges of the sheets. STEM images (Fig. S6, ESI†) show dark spots along the basal plane of the sheets but EDX analysis of the spots could not definitively confirm that they are Phe. We conclude, therefore, that by our route, functionalization is not limited to the edges and the resulting structure is analogous to that of GO.⁴

Raman spectroscopy (514 nm excitation) of **1** (Fig. 3) showed a D : G ratio of 0.78 in comparison to that of exfoliated μG at 0.66 (Fig. 3a and b). While there is not a significant change, this could be due to the distribution of functional groups on the surface and/or an effect of the size of the sheets.¹² The most noticeable feature in the spectrum of **1** is the loss of the 2D peak (*ca.* 2700 cm⁻¹). Most previous reports of functionalized graphene omit mention of this peak.^{11,13} The only material reported to show a similar loss of the 2D peak is graphene oxide (GO),¹⁴ in which the graphitic structure is almost completely oxidized with some unoxidized regions remaining. Based on the similar spectra of **1** to GO (Fig. 3b and c), the absence of the 2D peak indicates the lack of sp² carbons present and, therefore, the high degree of functionalization. Thermolysis of **1** at 600 °C for 12 h produced a black powder with a D : G ratio of 0.67 and a partially restored 2D peak (Fig. 3d) similar to that of the

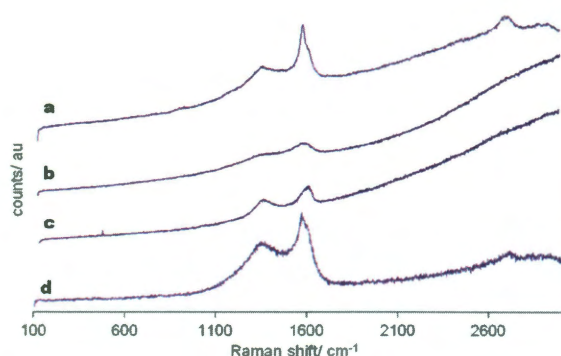


Fig. 3 Raman spectra of (a) exfoliated μ G, D : G 0.66; (b) **1**, D : G 0.78; (c) graphene oxide, D : G 0.77 and (d) annealed **1**, D : G 0.67.

exfoliated μ G sample. It should be noted that the bulk μ G material prior to exfoliation had a D : G ratio of 0.25 indicating possible modification to the electronic framework simply through sonication in ODCB.¹⁵

In conclusion, we have reported a high yield method of covalently functionalizing exfoliated graphene by nitrene addition in ODCB. The addition results in few-layer, DMSO soluble graphene sheets. Given the extensive range of organic azides accessible by a simple diazo-transfer reaction,⁶ this method offers a route to a wide variety of functional addends. The advantages of our method are as follows: (1) no final reduction step is required, (2) a wide variety of functional addends are accessible, (3) reactions are not limited to aqueous/polar conditions, and (4) highly functionalized, few-layer graphene sheets are produced. The control over the extent of functionalization is currently under investigation, as well as the feasibility of **1** as a solid phase support for peptide synthesis on the surface of a graphene scaffold.

Financial support for this work is provided by the Robert A. Welch Foundation. We thank Dr Noe Alvarez for the TEM images and Dr Dmitry Kosynkin for the graphene oxide sample.

Notes and references

† Boc-Phe(4-N₃)-OH (250 mg in ODCB) was added to the exfoliated μ G (Sigma Aldrich) solution in a 100 mL round bottom flask fitted with a condenser and a stir bar. Refluxing temperatures were maintained for 4 days after which the brown suspension was filtered over a 0.2 μ m PTFE filter paper. The filter cake was washed copiously with MeOH, CHCl₃, and DMF to remove any unreacted Phe(N₃). The fine brown powder was dried in an oven overnight at 125 °C. Final yield: 110 mg.

§ In a 500 mL Schlenk flask, imidazole-1-sulfonylazide-HCl (1.02 g, 6 mmol), Boc-Phe(4-NH₂)-OH (1.40 g, 5 mmol), and ZnCl₂ (27.3 mg, 0.20 mmol) was dissolved in MeOH : MeCN (3 : 2, 300 mL) to this

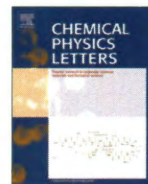
was added NEt₃ (1.39 mL, 10.0 mmol). After stirring at room temperature for 12 h, it was diluted with Et₂O (200 mL) and washed with AcOH (10%, 3 \times) and brine (1 \times). Drying with MgSO₄ and concentration, followed by flash chromatography yielded the pure product. Yield = 1.2 g, 80%. ¹H NMR (500 MHz, CDCl₃): δ 7.07 [2H, d, J (H-H) = 8.97 Hz, CH], 6.97 [2H, d, J (H-H) = 8.97 Hz, CH], 4.93 [1H, d, J (H-H) = 8.63 Hz, NH], 4.58 [1H, dd, J (H-H) = 6.64 Hz, J (H-H) = 14.92 Hz, CH], 3.12 [1H, dd, J (H-H) = 5.12 Hz, J (H-H) = 13.92 Hz, CH₂], 3.05 [1H, dd, J (H-H) = 6.41 Hz, J (H-H) = 13.64 Hz, CH₂], 1.42 [9H, s, 'Bu]. IR (cm⁻¹): 2115 (ν _{N₃}).

† To determine if polymerization of Phe on the graphene surface was occurring, we repeated the reaction with a methyl ester of Boc-azido-Phe. Protection at both carboxy and amino terminus should eliminate the possibility of peptide formation. Details of the reaction and characterization are included in the ESI.†

- 1 K. S. Novoselov, D. Jiang, F. Schedin, T. J. Booth, V. V. Khotkevich, S. V. Morozov and A. K. Geim, *Proc. Natl. Acad. Sci. U. S. A.*, 2005, **102**, 10451; A. K. Geim and K. S. Novoselov, *Nat. Mater.*, 2007, **6**, 183.
- 2 K. S. Novoselov, A. K. Geim, S. V. Morozov, D. Jiang, Y. Zhang, S. V. Dubonos, I. V. Grigorieva and A. A. Firsov, *Science*, 2004, **306**, 666.
- 3 A. B. Bourlino, D. Gournis, D. Petridis, T. Szabó, A. Szeri and I. Dékány, *Langmuir*, 2003, **19**, 6050; S. Park and R. S. Ruoff, *Nat. Nanotechnol.*, 2009, **4**, 217.
- 4 A. Lerf, H. He, M. Forster and J. Klinowski, *J. Phys. Chem. B*, 1998, **102**, 4477.
- 5 M. Prato, C. Li and F. Wudl, *J. Am. Chem. Soc.*, 1993, **115**, 1148; C. Gao, H. He, L. Zhou, X. Zheng and Y. Zhang, *Chem. Mater.*, 2009, **21**, 360.
- 6 E. D. Goddard-Borger and R. V. Stick, *Org. Lett.*, 2007, **9**, 3797.
- 7 C. E. Hamilton, J. R. Lomeda, A. Sun, J. M. Tour and A. R. Barron, *Nano Lett.*, 2009, **9**, 3460; C. E. Hamilton, J. R. Lomeda, Z. Sun, J. M. Tour and A. R. Barron, *Nano Res.*, 2010, **3**, 138.
- 8 L. M. Viculis, J. J. Mack, O. M. Mayer, H. T. Hahn and R. B. Kaner, *J. Mater. Chem.*, 2005, **15**, 974.
- 9 V. H. Rawal and M. P. Cava, *Tetrahedron Lett.*, 1985, **26**, 6141.
- 10 C. Gomez-Navarro, R. T. Weitz, A. M. Bittner, M. Scolari, A. Mews, M. Burghard and K. Kern, *Nano Lett.*, 2007, **7**, 3499; S. Stankovich, R. D. Piner, X. Chen, N. Wu, S. T. Nguyen and R. S. Ruoff, *J. Mater. Chem.*, 2006, **16**, 155; H. A. Becerril, J. Mao, Z. Liu, R. M. Stoltenberg, Z. Bao and Y. Chen, *ACS Nano*, 2008, **2**, 463.
- 11 J. Chattopadhyay, A. Mukherjee, C. E. Hamilton, J. H. Kang, S. Chakraborty, W. Guo, K. F. Kelly, A. R. Barron and W. E. Billups, *J. Am. Chem. Soc.*, 2008, **130**, 5414.
- 12 F. Tuinstra and J. L. Koenig, *J. Chem. Phys.*, 1970, **53**, 1126; A. C. Ferrari, *Solid State Commun.*, 2007, **143**, 47.
- 13 Y. Liua, J. Zhoua, X. Zhangb, Z. Liub, X. Wana, J. Tianb, T. Wanga and Y. Chen, *Carbon*, 2009, **47**, 3113; S. Ryu, M. Y. Han, J. Maultzsch, T. F. Heinz, P. Kim, M. L. Steigerwald and L. E. Brus, *Nano Lett.*, 2008, **8**, 4597; K. A. Worsley, P. Ramesh, S. K. Mandal, S. Niyogi, M. E. Itkis and R. C. Haddon, *Chem. Phys. Lett.*, 2007, **445**, 51.
- 14 J. R. Lomeda, C. D. Doyle, D. V. Kosynkin, W.-F. Hwang and J. M. Tour, *J. Am. Chem. Soc.*, 2008, **130**, 16201.
- 15 S. Niyogi, M. A. Hamon, D. E. Perea, C. B. Kang, B. Zhao, S. K. Pal, A. E. Wyant, M. E. Itkis and R. C. Haddon, *J. Phys. Chem. B*, 2003, **107**, 8799; K. R. Moonosawmy and P. Kruse, *J. Phys. Chem. C*, 2009, **113**, 5133.

Appendix B

K. S. Liao, J. Wang, D. Fruchtl, N. J. Alley, E. Andreoli, E. P. Dillon, A. R. Barron, H. Kim, H. J. Byrne, W. J. Blau, and S. A. Curran, *Chem. Phys. Lett.*, 2010, **489**, 207.



Optical limiting study of double wall carbon nanotube–Fullerene hybrids

Kang-Shyang Liao^{a,*}, Jun Wang^b, Daniel Früchtl^b, Nigel J. Alley^{a,c}, Enrico Andreoli^a, Eoghan P. Dillon^d, Andrew R. Barron^d, Hansoo Kim^e, Hugh J. Byrne^f, Werner J. Blau^{b,g}, Seamus A. Curran^a

^a Institute for NanoEnergy, Department of Physics, University of Houston, Houston, TX 77204, USA

^b School of Physics and the Centre for Research on Adaptive Nanostructures and Nanodevices (CRANN), Trinity College Dublin, Dublin 2, Ireland

^c School of Physical Sciences, Dublin City University, Glasnevin, Dublin 9, Ireland

^d Richard E. Smalley Institute for Nanoscale Science and Technology, Center for Biological and Environmental Nanotechnology, Carbon Nanotube Laboratory, Rice University, Houston, TX 77005, USA

^e Microscopy and Imaging Center, Texas A&M University, College Station, TX 77843, USA

^f Focas Institute, Dublin Institute of Technology, Dublin 8, Ireland

^g School of Physics, Dublin Institute of Technology, Kevin Street, Dublin 2, Ireland

ARTICLE INFO

Article history:

Received 5 January 2010

In final form 2 March 2010

Available online 6 March 2010

ABSTRACT

In order to merge complementary temporal and spatial nonlinear optical characteristics of Fullerene and carbon nanotubes, synthesis of double wall carbon nanotube–Fullerene hybrid was performed by covalently linking DWNT and C₆₀ by amination reaction with polyethylenimine. DWNT–Fullerene hybrids were characterized by thermogravimetric analysis, UV–vis spectroscopy and transmission electron microscopy. Optical limiting performance of DWNT–Fullerene hybrids is superior to those of Fullerenes and SWNTs at the same level (~80%) of transmission. Whereas nonlinear scattering is an evident mechanism, reverse saturable absorption from Fullerene moieties has significant contribution. Charge transfer between the DWNT and Fullerene moieties may play an important role of optical limiting.

© 2010 Elsevier B.V. All rights reserved.

1. Introduction

Recently, there has been increasing interest in the application of nanotechnology to protective coatings, including polymer nanotubular thin film composites. The use of carbon nanotubes in nanocomposites revealed a multiplicity of applications as nano-fillers in polymer hosts including thermal sensors [1] and antistatic coatings [2]. However, the success of nanocomposite fabrication is still dependent on developing reliable synthetic methods in forming their primary building blocks, a process that is challenging at the nanoscale for both inorganic and organic nanomaterials. Nonetheless, there have been significant advances in the use of nanocomposites in various optical applications, including organic light emitting diodes [3] and optical limiters [4]. Since the invention of lasers in the 1960s, not only have they become powerful instruments for material assessment, but are also commonly used in our daily life, such as surgery and telecom applications. Protection from lasers is consequently not a trivial matter but is one of genuine concern from a public safety and technological perspective. The development of optical limiting materials/devices provides a valuable solution to the dangers of lasers, as well as various other forms

of optical instruments being used. A successful optical limiter should strongly attenuate intense, potentially dangerous laser beams, while exhibiting high transmittance for low intensity ambient light. Investigating optical limiting materials/mechanisms/devices is therefore a very important area of research [5–8]. In the forefront of this field is a quest for ideal materials that include carbon nanomaterials [7,8], phthalocyanines [9,10], porphyrins [11], organometallics, inorganic semiconductors and liquid crystals [5,6]. In particular, the carbon nanomaterials: carbon black [12], Fullerenes [13,14], carbon nanotubes (CNTs) [4,15–17] and graphenes [18] all make a great contribution to laser protection applications.

During the past two decades, researchers have established several effective nonlinear optical (NLO) mechanisms for optical limiting, namely, reverse saturable absorption (RSA), two-photon absorption (TPA), free-carrier absorption, nonlinear scattering and nonlinear refraction [5,8]. Fullerene–C₆₀ is considered an ideal optical limiter across the visible spectrum (from 400 to 700 nm) since it was first studied by Tutt and Kost [14]. The primary mechanism of optical limiting for C₆₀ is RSA, which involves formations of excited states (triplet–triplet) with an absorption cross section much larger than that of the ground-state, leading to nonlinear absorption. More recent studies show CNTs have potential as a broadband optical limiter from 430 to 1064 nm [4,7,8,15]. Thermally-induced nonlinear scattering and nonlinear refraction are found to be the dominant mechanisms. At low fluences, nonlinear

* Corresponding author. Address: Institute for NanoEnergy, Department of Physics, 617 Science and Research Building 1, University of Houston, Houston 77004, USA. Fax: +1 713 743 3589.

E-mail address: kliao@mail.uh.edu (K.-S. Liao).

scattering comes from solvent microbubbles generated by heat transfer from CNTs. At high fluences, the scattering is mainly due to formations of carbon microplasmas. Therefore, the superior optical limiting performance of CNTs can be attributed to their unique electronic structures that absorb broadband energy, as well as their large surface area that can effectively dispatch the energy to surrounding environments. In contrast to Fullerenes with a quick response time in the picosecond regime, CNTs generally respond at best in the nanosecond regime.

The development of nonlinear absorber–CNT hybrids by covalent or noncovalent combination has been reported by several groups [19–23]. In this work, we report the synthesis, characterization and optical limiting property of a covalent linked CNT–Fullerene hybrid. The hybrid is expected to merge complementary temporal and spatial NLO characteristics of Fullerene and carbon nanotubes, resulting in a viable optical limiting material satisfying most of requirements for laser protection.

2. Experimental methods

2.1. Materials

DWNTs prepared using a CVD method (>95% purity, O.D. of 4 nm and length of 5–20 μm) were obtained from Nanolab. Transmission electron microscope (TEM) images revealed that the pristine DWNT sample is actually a mixture of SWNT, DWNT, TWNT and FWNT. Polyethylenimine (PEI, branched, $M_n = 10\,000$ Da), *N,N*-dimethylformamide (DMF, anhydrous, 99.8%), Fullerene- C_{60} (98%), chlorobenzene (anhydrous, 99.8%) were obtained from Aldrich and used as-received.

2.2. Direct amination of DWNTs

DWNTs (3 g) and polyethylenimine ($M_n \sim 10\,000$) (15 g) were mixed in 250 mL of DMF. Sonication for 20 min and stirring at 50 $^\circ\text{C}$ for 5 d formed the product, DWNT–PEI10 000. The resulting suspension was filtered through a 0.20 μm nylon membrane and the precipitate was washed with 1 M HCl, 1 M NaOH, water and methanol to remove any excess PEI. After drying, 5.5 g of the product was obtained. Characterization of the product was carried out by titration. A known amount of DWNT–PEI10 000 was added to 20 mL of 0.01 M HCl. After sonicating the mixture for 1 h at 25 $^\circ\text{C}$, an aliquot (5 mL) of the resulting HCl solution was titrated to a pH 9.0 endpoint using 0.01 M NaOH. The difference between

the original amount of HCl and the amount of HCl titrated corresponded to the loading of titratable amino groups on DWNT–PEI10 000 and was 0.9 mequiv of titratable amine groups/g.

2.3. Synthesis of DWNT–PEI10 000– C_{60}

DWNT–PEI10 000 (300 mg), Fullerene- C_{60} (150 mg) and triethylamine (0.5 mL) were mixed in 20 mL of chlorobenzene. Sonication for 1 min and stirring at 100 $^\circ\text{C}$ for 5 d formed the product, DWNT–PEI10 000– C_{60} . The resulting suspension was filtered through a 0.20 μm nylon membrane and the precipitate was washed with chlorobenzene and methanol to remove any excess C_{60} and triethylamine. After drying, 408 mg of the product was obtained.

2.4. Synthesis of PEI10 000– C_{60}

PEI10 000 (50 mg), Fullerene- C_{60} (100 mg) and triethylamine (1.0 mL) were mixed in 10 mL of chlorobenzene. Sonication for 1 min and stirring at 100 $^\circ\text{C}$ for 5 d formed the product, PEI10 000– C_{60} . The resulting suspension was filtered through a 0.20 μm nylon membrane and the precipitate was washed with chlorobenzene and methanol until the filtrate became colorless. After drying, 122 mg of the product was obtained.

2.5. Characterization

Thermogravimetric analysis (TGA) was recorded by SEIKO 1 TG/DTA 200 under Ar or air from 30 to 950 $^\circ\text{C}$. UV–vis spectra were recorded by an Ocean Optics HR2000 + high resolution spectrometer using a Mikropack PH-2000-BAL Deuterium–Halogen light source. High resolution micrographs were taken by an FEI TECNAI G2 20F transmission electron microscope. It was operated at a 200 kV accelerating voltage, equipped with a ZrO_2/W Schottky field emission gun and a Gatan imaging filter slow-scan CCD camera (GIF Tri-diem with $2\text{ k} \times 2\text{ k}$ pixels). Bright field TEM images were collected by the CCD camera of the TECNAI 20F.

2.6. Z-scan measurement

NLO and optical limiting properties of DWNT–Fullerene hybrids were studied using open aperture Z-scan method, which is widely adopted to investigate third-order NLO processes, including nonlinear absorption, scattering and refraction. In this work, a Z-scan

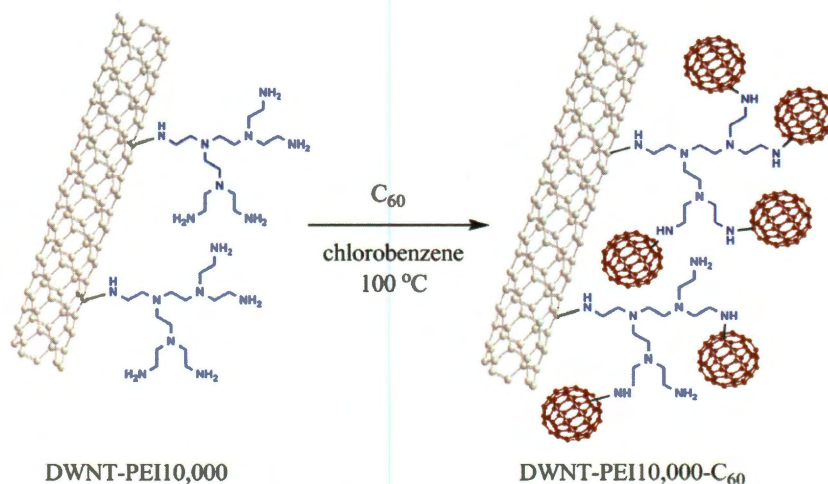


Fig. 1. Synthesis of DWNT–PEI10 000– C_{60} .

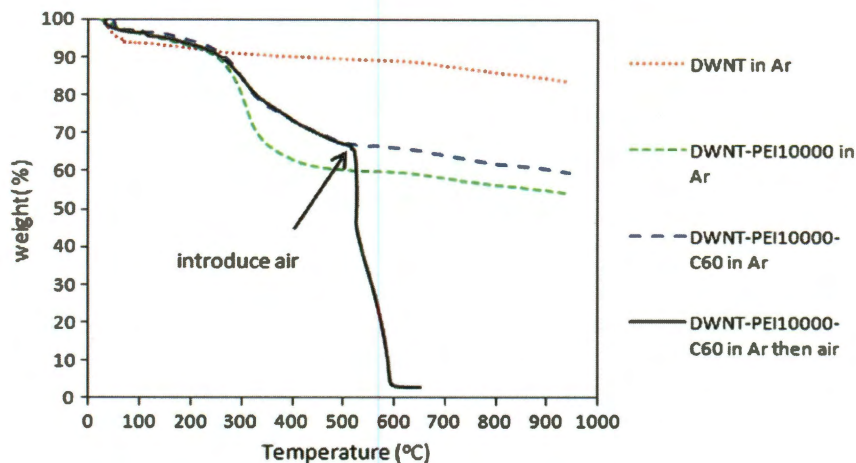


Fig. 2. TGA of DWNT, DWNT-PEI10 000, DWNT-PEI10 000-C₆₀ in Ar and DWNT-PEI10 000-C₆₀ in Ar followed by air introduced at 500 °C.

was performed using 6 ns pulses from a Q-switched Nd:YAG laser. After spatially removing higher-order modes, a laser beam was tightly focused with a 9 cm focal length lens. The laser was operated at its second harmonic, 532 nm, with a repetition rate of 10 Hz. Simultaneously, a focusing lens setup was arranged at $\sim 30^\circ$ to the direct incident beam to monitor the scattered light

from the dispersions. All samples were tested in 1.0 cm quartz cells.

3. Results and discussion

Syntheses and studies of CNT-Fullerene hybrids have been reported [24,25]. D'Souza et al. performed syntheses of SWNT/Pyr-NH₃⁺/crown-C₆₀ hybrids by supramolecular assembly and studied their photoinduced electron transfer [24]. The results suggested a possibility of electron transfer from SWNTs to singlet excited Fullerenes in the hybrids. Wu et al. performed syntheses of grapevine SWNT-C₆₀ hybrids by covalent amide formation between oxidized SWNT and C₆₀ derivative [25]. Characterizations revealed a ground-state electron transfer trend from SWNT to C₆₀ moieties in the grapevine nanostructure. Although these CNT-Fullerene hybrids show great potential as materials for non-linear optics, their syntheses are prohibitively complicated and time consuming. Here, we synthesized CNT-Fullerene hybrids using all commercial available reagents in only two steps. DWNTs are first treated with an excess amount of polyethylenimine (PEI) in *N,N*-dimethylformamide (DMF) at 50 °C to give DWNT-PEI10 000 by following a procedure described by Liao et al. [26]. Similar procedures were carried out by Dillon et al. for SWNT amination as well [27]. The PEI functionalized DWNTs can readily disperse in common organic solvents and the free amines on PEI functionalized DWNTs can act as nucleophiles. In the next step,

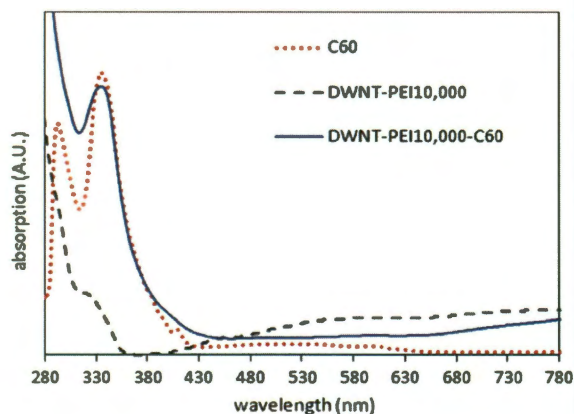


Fig. 3. UV-vis spectra of C₆₀, DWNT-PEI10 000 and DWNT-PEI10 000-C₆₀ in chlorobenzene.

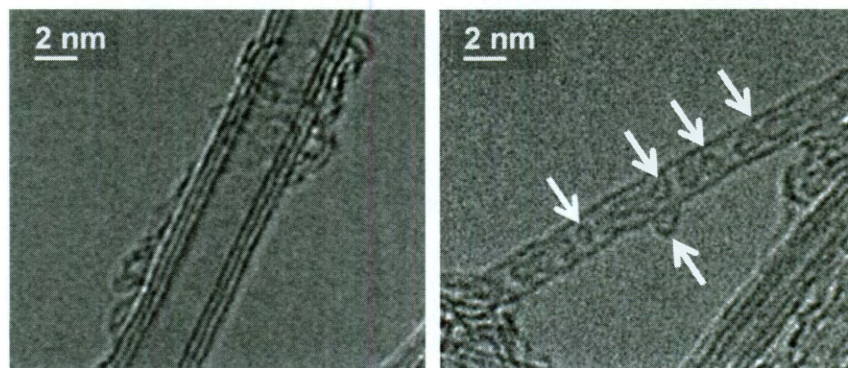


Fig. 4. TEM images of a pristine TWNT partially covered with carbon materials (left) and a SWNT-Fullerene hybrid (right). The circular profiles indicated by the arrows suggest that monomeric C₆₀ molecules (based on their size and shape) are attached to the inner and outer surfaces of the nanotube.

DWNT-PEI10 000 was reacted with an excess amount of C_{60} in chlorobenzene at 100 °C for 5 days, as shown in Fig. 1. Amination of Fullerenes was first studied by Hirsch et al. [28] and it is suggested that amination of CNTs involves a similar mechanism as amination of Fullerenes [29].

Characterization of CNT-Fullerene hybrids included a series of chemical and physical analyses. Thermogravimetric analysis (TGA) under Ar showed distinct differences between the PEI derivative of DWNTs and starting DWNTs. As shown in Fig. 2, as-received DWNTs exhibited a gradual weight loss of 10% over a temperature range 30–950 °C. DWNT-PEI10 000 exhibited a ~30% weight loss in the 250–350 °C temperature range. The

weight loss in this region was ascribed to loss of the grafted PEI on DWNT samples. The TGA of DWNT-PEI10 000- C_{60} under Ar exhibited a ~25% weight loss at the same temperature range, this represented the loss of grafted PEI. However, no extra weight loss was observed at higher temperature range. Presumably, both DWNT and C_{60} residue did not burn under Ar. This hypothesis was proved by a separate TGA of PEI10 000- C_{60} under Ar over a temperature range 30–800 °C (data not shown). The TGA showed more than 60% of residue was left which can be ascribed to the C_{60} residue. In order to differentiate the composition of remaining residue of DWNT-PEI10 000- C_{60} , the next TGA was first carried out under Ar from 30 to 500 °C to fully degrade PEI, air was then introduced to the heating chamber and the temperature was increased gradually to 650 °C. A sudden drop of ~25% weight was observed at 520 °C, followed by a more gradual weight loss of another 45% from 520 to 600 °C. The first sudden drop was ascribed to the loss of C_{60} because all C_{60} molecules should burn at the same temperature. While the gradual weight loss from 520 to 600 °C can be ascribed to the loss of DWNT because it is dependent on the diameter and length of DWNTs. Each individual DWNT should burn gradually under different temperature ranges.

The formation of DWNT-Fullerene hybrids was also confirmed by UV-vis spectroscopy. As shown in Fig. 3, relative to the spectrum of C_{60} , the spectrum of DWNT-PEI10 000- C_{60} in chlorobenzene showed a maximum absorption of 330 nm. The peak at 330 nm can be assigned to the allowed ${}^1T_{1u} \rightarrow {}^1A_g$ transition of C_{60} [30]. Direct evidence of the formation of nanotube-Fullerene hybrids can be seen through high resolution TEM micrographs as well. As shown in Fig. 4, while the image of a pristine nanotube (left) shows a smooth surface covered with some amorphous carbon materials, a monomeric form of C_{60} spheres (right) can be clearly seen to be attached to the inner and outer surfaces of the SWNT in the image of the nanotube-Fullerene hybrid.

For the optical limiting study, the hybrid was dispersed in chlorobenzene and poly(*m*-phenylenevinylene-*co*-2,5-dioctoxyp-phenylenevinylene) (PmPV), respectively. PmPV is a well-known conjugated polymer used to disperse carbon nanotubes, resulting in property modified nanocomposites [3,31]. The normalized transmission and scattered light as functions of incident energy density is shown in Fig. 5. As the incident energy density was increased, intense scattered light was observed from DWNT-Fullerene dispersions along with decreasing transmission. Therefore the nonlinear scattering, arising from DWNT moieties, is regarded as one of the main mechanisms for optical limiting. The mechanism leading to optical limiting effects in carbon nanotubes has been studied intensively. The induced scattering centers are composed of solvent bubbles and carbon microplasmas. Due to the solvent effect [8,17], the hybrid dispersed in chlorobenzene possess superior optical limiting response and stronger scattered signal in comparison to the polymer dispersions. In addition, it is believable that RSA from Fullerene moieties has significant contribution as well. The superior optical limiting effect of the hybrids results from an accumulation of different mechanisms.

In order to evaluate the optical limiting ability of DWNT-Fullerene dispersions, we compare the optical limiting response of this

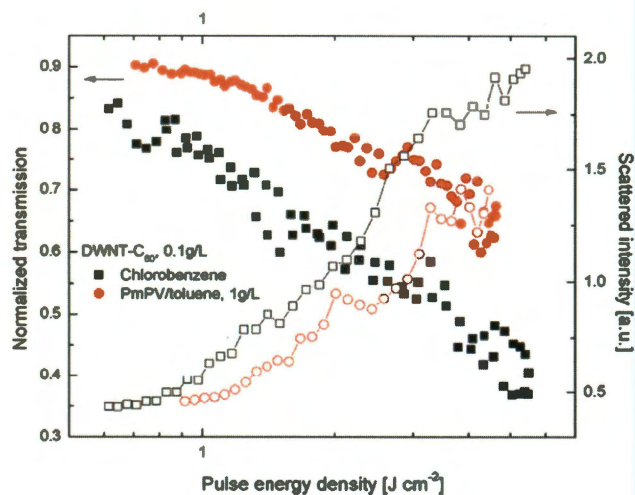


Fig. 5. Plots of normalized transmission and scattering light against incident pulse energy density for DWNT-Fullerene dispersions.

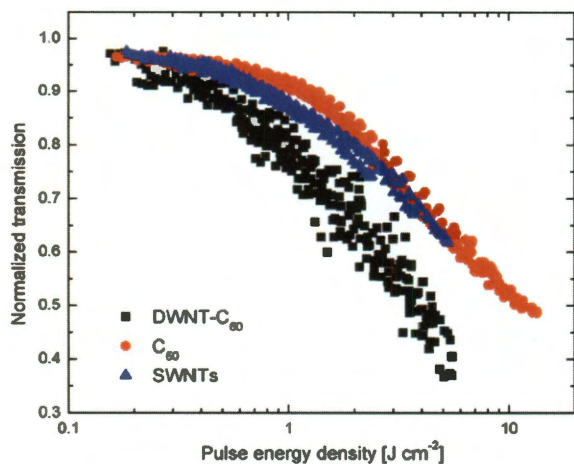


Fig. 6. Optical limiting responses of the DWNT-Fullerene, Fullerene and SWNTs.

Table 1
Linear and NLO coefficients for the DWNT-Fullerene, Fullerene and SWNTs.

Material	Host	Conc. (g/L)	T (%)	α_0 (cm ⁻¹)	β_{eff} (cm GW ⁻¹)	$\text{Im}\{\chi^{(3)}\}$ ($\times 10^{-12}$ esu)
DWNT- C_{60}	Chlorobenzene	0.1	79.8	0.23	7.01 ± 0.99	2.74 ± 0.39
	PmPV/toluene	0.1	83.4	0.18	4.01 ± 1.15	1.51 ± 0.43
SWNTs	DMF	0.005	81.3	0.21	2.46 ± 0.50	0.85 ± 0.17
C_{60}	Toluene	0.11	81.9	0.20	3.28 ± 0.51	1.24 ± 0.19

hybrid with that of Fullerenes and SWNTs. As shown in Fig. 6, the optical limiting performance of this hybrid is superior to those of Fullerenes and CNTs at the same level of transmission. Table 1 summarizes the linear and NLO coefficients for these three materials.

4. Conclusion

In summary, synthesis and characterization of DWNT–Fullerene hybrids was performed to merge complementary temporal and spatial NLO characteristics of Fullerene and carbon nanotubes. The optical limiting performance of DWNT–Fullerene hybrids is superior to those of Fullerenes and SWNTs at the same level of transmission. Future studies regarding mechanisms that contribute to this better optical limiting performance and the influence of covalent linkages between DWNTs and C₆₀ to optical limiting are currently underway.

Acknowledgements

The work is supported by the US Department of Energy under Grant No. DE-FG36-08GO88008 and in part by the Science Foundation Ireland (SFI) under Grant No. 08/CE/I1432. J.W. thanks SFI for his postdoctoral research fellowship.

References

- [1] C. Li, E.T. Thostenson, T.-W. Chou, *Compos. Sci. Technol.* 68 (2008) 1227.
- [2] S.A. Curran, D. Zhang, W.T. Wondmagegn, A.V. Ellis, J. Cech, S. Roth, D.L. Carroll, *J. Mater. Res.* 21 (2006) 1071.

- [3] S.A. Curran et al., *Adv. Mater.* 10 (1998) 1091.
- [4] P. Chen, X. Wu, X. Sun, J. Lin, W. Ji, K.L. Tan, *Phys. Rev. Lett.* 82 (1999) 2548.
- [5] L.W. Tutt, T.F. Boggess, *Prog. Quantum Electron.* 17 (1993) 299.
- [6] Y.-P. Sun, J.E. Riggs, *Int. Rev. Phys. Chem.* 18 (1999) 43.
- [7] Y. Chen et al., *J. Nanosci. Nanotechnol.* 7 (2007) 1268.
- [8] J. Wang, W.J. Blau, *J. Opt. A: Pure Appl. Opt.* 11 (2009) 024001.
- [9] S.M. O'Flaherty, S.V. Hold, M.J. Cook, T. Torres, Y. Chen, M. Hanack, W.J. Blau, *Adv. Mater.* 15 (2003) 19.
- [10] J.J. Doyle et al., *J. Opt. A: Pure Appl. Opt.* 10 (2008) 075101.
- [11] W. Blau, H. Byrne, W.M. Dennis, J.M. Kelly, *Opt. Commun.* 56 (1985) 25.
- [12] K. Mansour, M.J. Soileau, E.W. Van Stryland, *J. Opt. Soc. Am. A* 9 (1992) 1100.
- [13] W.J. Blau et al., *Phys. Rev. Lett.* 67 (1991) 1423.
- [14] L.W. Tutt, A. Kost, *Nature* 356 (1992) 225.
- [15] L. Vivien, P. Lancon, D. Riehl, F. Hache, F. Anglaret, *Carbon* 40 (2002) 1789.
- [16] J. Wang, W.J. Blau, *Appl. Phys. B* 91 (2008) 521.
- [17] J. Wang, W.J. Blau, *J. Phys. Chem. C* 112 (2008) 2298.
- [18] J. Wang, Y. Hernandez, M. Lotya, J.N. Coleman, W.J. Blau, *Adv. Mater.* (2009).
- [19] N. Izard, C. Menard, D. Riehl, E. Doris, C. Mioskowski, E. Anglaret, *Chem. Phys. Lett.* 391 (2004) 124.
- [20] S. Webster, M. Reyes-Reyes, X. Pedron, R. López-Sandoval, M. Terrones, D.L. Carroll, *Adv. Mater.* 17 (2005) 1239.
- [21] E.M. Ni Mhuircheartaigh, S. Giordani, W.J. Blau, *J. Phys. Chem. B* 110 (2006) 23136.
- [22] Z.B. Liu, J.G. Tian, Z. Guo, D.M. Ren, F. Du, J.Y. Zheng, Y.S. Chen, *Adv. Mater.* 20 (2008) 511.
- [23] J. Wang, W.J. Blau, *Chem. Phys. Lett.* 465 (2008) 265.
- [24] F. D'Souza, R. Chitta, A.S.D. Sandanayaka, N.K. Subbaiyan, L. D'Souza, Y. Araki, O. Ito, *J. Am. Chem. Soc.* 129 (2007) 15865.
- [25] W. Wu, H. Zhu, L. Fan, S. Yang, *Chem. Eur. J.* 14 (2008) 5981.
- [26] K.-S. Liao, A. Wan, J.D. Batteas, D.E. Bergbreiter, *Langmuir* 24 (2008) 4245.
- [27] E.P. Dillon, C.A. Crouse, A.R. Barron, *ACS Nano* 2 (2008) 156.
- [28] A. Hirsch, Q. Li, F. Wudl, *Angew. Chem., Int. Ed. Engl.* 30 (1991) 1309.
- [29] E.V. Basiuk, M. Monroy-Pelaez, I. Puente-Lee, V.A. Basiuk, *Nano Lett.* 4 (2004) 863.
- [30] Z. Gasyna, P.N. Schatz, J.P. Hare, T.J. Dennis, H.W. Kroto, R. Taylor, D.R.M. Walton, *Chem. Phys. Lett.* 183 (1991) 283.
- [31] S. Curran et al., *Synth. Met.* 103 (1999) 2559.

Appendix C

A. Haldar, S. D. Yambem, K-L, Liao, N. Alley, E. P. Dillon, A. R. Barron, and S. A. Curran, *Thin Solid Films*, 2011, **519**, 6169-6173.



Organic photovoltaics using thin gold film as an alternative anode to indium tin oxide

Amrita Haldar^{a,*}, Soniya D. Yambem^a, Kang-Shyang Liao^a, Nigel J. Alley^{a,b}, Eoghan P. Dillon^c, Andrew R. Barron^c, Seamus A. Curran^a

^a Institute for NanoEnergy, Department of Physics, University of Houston, Houston, TX 77204, USA

^b School of Physical Sciences, Dublin City University, Glasnevin, Dublin 9, Ireland

^c Richard E. Smalley Institute for Nanoscale Science and Technology, Center for Biological and Environmental Nanotechnology, Carbon Nanotube Laboratory, Rice University, Houston, Texas 77005, USA

ARTICLE INFO

Article history:

Received 3 June 2010

Received in revised form 12 April 2011

Accepted 13 April 2011

Available online 22 April 2011

Keywords:

Solar cell

Gold

Work-function

Bulk hetero-junction

Photo-voltage

ABSTRACT

Indium Tin Oxide (ITO) is the most commonly used anode as a transparent electrode and more recently as an anode for organic photovoltaics (OPVs). However, there are significant drawbacks in using ITO which include high material costs, mechanical instability including brittleness and poor electrical properties which limit its use in low-cost flexible devices. We present initial results of poly(3-hexylthiophene): phenyl-C₆₁-butyric acid methyl ester OPVs showing that an efficiency of 1.9% (short-circuit current 7.01 mA/cm², open-circuit voltage 0.55 V, fill factor 0.49) can be attained using an ultra thin film of gold coated glass as the device anode. The initial I-V characteristics demonstrate that using high work function metals when the thin film is kept ultra thin can be used as a replacement to ITO due to their greater stability and better morphological control.

© 2011 Elsevier B.V. All rights reserved.

1. Introduction

In the last two decades there has been a significant rise in interest in organic electronics and in particular organic photovoltaics (OPVs) [1–3]. The interest arises as thin film cells offer the opportunity to work in regions of diffuse light as opposed to classical crystalline silicon solar cells. In addition, the tailorability of OPVs in terms of the heterojunction and the use of a variety of organic semiconductors can enable greater tenability of the OPVs [4–7]. In its simplest form, bulk hetero-junction OPVs consists of a light absorbing semiconducting thin (50–100 nm) film sandwiched between two electrodes [8,9]. More specifically, the heterojunction consists of an electron acceptor blended into the semiconducting polymer which acts as the electron donor as opposed to the more classical p–n junction seen in the inorganic world. The reason for blending both together is that in order to get effective exciton dissociation, both acceptor and donor must lie in close proximity due to short exciton diffusion length. Additionally, the films must be kept ultra thin due to the inherent poor mobility of organic semiconductors, thereby reducing some of the risks of deep traps and loss of charges that can occur due to the potential presence of defect states. Bulk heterojunctions, as a consequence of the blending, has the advantage of being able to dissociate excitons quite efficiently thereby generating electron–hole pairs throughout the film. The most commonly used polymer as the electron donor is

regioregular poly(3-hexylthiophene) (P3HT) and phenyl-C₆₁-butyric acid methyl ester (PCBM) is the electron acceptor. OPVs made using the P3HT:PCBM blend can reach efficiencies as high as 5.2% [10]. In a typical OPV architecture, a low work function metal is used as the electron-collecting cathode and a high work function metal (or metal oxide) is used as the hole-collecting anode. Indium Tin Oxide (ITO) is the most common choice for the hole-collecting anode because it provides an excellent combination of high optical transparency in the visible range (~85%) and a low surface resistivity of 20–80 Ω/□ for a 100 nm thick ITO film [11]. Depending on the thickness and the deposition condition, even lower surface resistivity of 8–12 Ω/□ for a 120–160 nm thick ITO film coated on glass slides is commercially available [12]. ITO has however significant drawbacks that include rising costs due to scarcity of indium and its brittleness, which limits its usage in flexible devices [13–17]. The preparation of high quality ITO films uses high temperature processes and usually requires post deposition treatments. This expensive production process commercially rules out ITO as an anode material for low cost OPVs. Recent studies have shown that the conductivity of ITO is a major contributor to series resistance. High series resistance causes the fill factor (FF) to decrease and thus, lowers the power conversion efficiency (PCE) [18]. This effect especially limits the performance of large area devices [19,20]. These issues have led to significant efforts to find alternative transparent, conductive electrode materials with mechanical flexibility.

Au has been used in combination with other materials in organic optoelectronic applications [21–23]. Bernede et al. demonstrated that the use of an ultra-thin Au film (0.5 nm) over transparent anodes

* Corresponding author.

E-mail address: ahaldar@mail.uh.edu (A. Haldar).

improved the performance of OPVs. The PCE increased from 1.12% to 2.1% for ITO, 0.11% to 2% for fluorine-doped tin oxide (FTO) and from 0.27% to 1.27% for aluminum-doped zinc oxide [22]. The insertion of an ultra-thin Au film caused the series resistance of the device to decrease significantly and the shunt resistance to increase, resulting in improved performance. The author suggests that the high work function of Au leads to a better energy matching between the work function of anode and the highest occupied molecular orbital of the organic electron donor, increasing the hole transfer efficiency. Thus, the improved performance of the OPVs can be largely attributed to the high work function of Au. Kouskoussa et al. introduced an ultra-thin Au film at the interface of FTO and copper phthalocyanine (CuPc) [23]. The presence of Au film caused the PCE of the resulting FTO/Au/CuPc/C₆₀/tris(8-hydroxyquinolino)aluminum (Alq₃)/Al device to increase from 0.27 to 1.12%. They suggest that the insertion of Au improved the hole collection efficiency, and thus, the cell performance. Au layer has also been used to improve the performance of organic light emitting diodes (OLEDs) [21,24]. A thick layer of Au (up to 15 nm) was used over ITO to improve conductivity and to form a better band matching which results in improved device performance [21]. However, research work using Au films as independent electrodes for organic optoelectronics has been limited [24–26]. Hatton et al. demonstrated that when an ultra thin Au anode (70 Å) was incorporated in a bilayer OLED Au anode/N,N'-bis(3-methylphenyl)-N,N'-diphenyl-1,1'-biphenyl-4,4'-diamine/Alq₃/lithium benzoate/Al, it exhibited a lower turn-on voltage. Also its uniformity of brightness and stability was comparable with OLEDs with ITO [24]. Au anodes have been used as a part of solution-processed organic tandem solar cells, but the efficiencies were low, 0.35% and 0.23% for the bottom and top cells, respectively [25]. Cho et al. demonstrated using Au anodes as a part of a multi-functional device, comprising of a field-effect transistor and an OPV on the same substrate reported a PCE of only 0.6% and a short circuit current (J_{sc}) of 2.3 mA/cm² [26].

The high conductivity of the Au anodes is of critical importance for large area devices, where high sheet resistance leads to Ohmic losses which reduce the OPV performance. The use of non-patterned thin metal films as anodes, instead of metallic conductive grids, will significantly reduce processing and fabrication costs. Thin metal films can be bent and still retain their conductivity due to their ductility [27]. Thus, the replacement of ITO by thin metal films can lead to improved mechanical properties of the OPVs. Our results indicate that Au anodes are a promising replacement for ITO in organic photovoltaics. We present the initial results of P3HT:PCBM bulk heterojunction OPV fabrication using semi-transparent Au as an anode showing PCE of 1.9%. The maximum J_{sc} obtained is 10.77 mA/cm².

2. Experimental details

2.1. Fabrication of photovoltaic device

The present OPV device structure and layout are shown in Fig. 1. In this study, an island-type electrode geometry was used instead of a crossbar-type electrode geometry in order to eliminate errors arising due to a contribution from a poly(3,4-ethylenedioxythiophene)-poly(styrenesulfonate) (PEDOT:PSS) OPV device (PEDOT:PSS anode/active blend/Al cathode) [28,29]. The first step of the fabrication process was the cleaning of the microscope cover glass (Fisher). They were cleaned in an ultra-sonic bath using 1.75% micro-90 solution (10 min), water (15 min) and isopropyl alcohol (IPA) (15 min) consecutively and dried using nitrogen. Successive layers of Chromium (Cr, 99.998%, Kurt Lesker) (~5 nm) and Au (99.999%, Kurt Lesker) (~20 nm) were thermally evaporated through a shadow mask onto the cleaned glass slides at a pressure of 2×10^{-4} Pa. The deposition was carried out using a one-filament system and vacuum was broken between deposition of Cr and Au. Two separate tungsten wire baskets were used to prevent cross-contamination of the metals.

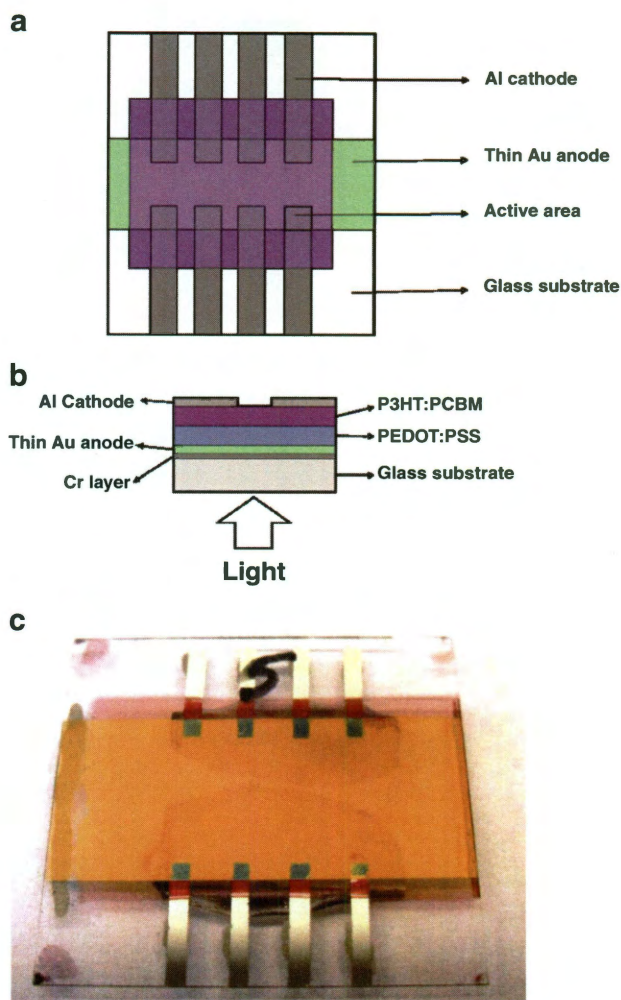


Fig. 1. (a) A schematic representation of the OPV device layout. The active area of each device is defined as the overlapping region of the electrodes. (b) A schematic representation of the OPV device structure illustrates the deposition sequence. (c) Image of the actual slide.

The Au covered glass substrates were dipped in IPA and blow-dried with nitrogen to remove any dust particles. They were treated by ozone plasma for 20 min before spin-coating a thin layer (~110 nm) of electron blocking PEDOT:PSS (Clevios PH750, H. C. Starck, filtered through a 0.45 μm Corning SFCA membrane filter) at 1500 rpm for 3 min. This step was skipped for the devices fabricated without the PEDOT:PSS layer. The substrates were dried in an oven at 100 °C for 1 h in N₂ atmosphere. A thin layer (~65 nm) of photo-active material was spin-coated (1200 rpm, 3 min) onto the substrates before dried again in an oven under the same conditions. The photo-active material was prepared using a donor/acceptor blend of P3HT:PCBM (purchased separately from Aldrich) with a weight ratio of 1 to 0.68 and a concentration of 12 g/L in anhydrous chlorobenzene solution. Thermally evaporated aluminum electrodes were deposited through a custom made shadow mask, at a pressure of 3×10^{-4} Pa. Immediately after Al deposition, the devices were encapsulated with glass slides and epoxy resin in a N₂ filled glove box (~10% relative humidity) at room temperature to avoid environmental influences.

Several reference devices were also produced on ITO for comparison. All devices were fabricated on ITO-coated glass slides (8–12 Ω/□ surface resistivity, Aldrich). The pristine ITO substrates were dusted with Zinc powder and etched under a 18% HCl_(aq) solution for 10 s to form the desired anode layout. They were then

cleaned as the same process described above. The substrates were subsequently treated with ozone plasma for 6 min and then PEDOT:PSS layer was spin-coated at 3000 rpm for 2 min to form a thin, hole transport layer. The substrates were dried in an 80 °C oven for 1 h before deposition of the active layer. The P3HT:PCBM active layer was spin-coated on top of the PEDOT:PSS layer at 1500 rpm for 2 min. This step was skipped for the devices fabricated without PEDOT:PSS layer. After the final spin coating process, the substrates were solvent-annealed in an environment filled with chlorobenzene vapor at room temperature for 30 min and dried in an 80 °C oven for 1 h. Patterned Al electrodes were thermally evaporated (at a pressure of 8×10^{-4} Pa) on top of the photoactive layer by a custom made shadow mask. All devices were encapsulated with glass slides using epoxy resin in a N_2 atmosphere (~10% relative humidity) at room temperature before characterization.

2.2. Characterization of photovoltaic device

An Abet LS 150 Xenon Arc Lamp Source coupled with an AM 1.5 G filter was used as the light source. The devices were illuminated through the thin Au anode under 1 sun (100 mW/cm^2 , calibrated with Oriel 91150 V Solar Reference Si Cell certified by NREL). The current–voltage (*I*-*V*) characteristics of the photovoltaic device were measured using a Keithley 2400 SourceMeter without correction for spectral mismatch. The measurements were done in a N_2 filled glove box (~10% relative humidity).

The transmission measurements were obtained using an OCEAN OPTICS spectrometer (model HR2000+). The thickness measurements were carried out using an Alpha-Step 200 Profilometer (Tencor Instruments). The surface morphology was determined by Digital Instrument Nanoscope IIA Atomic Force Microscope (AFM) using the tapping mode. The active areas were measured using a Leitz ERGOLUX microscope. The active areas of each device, defined by the overlap of Al cathode and the Au anode, were between 0.7 and 1.1 mm^2 . The sheet resistance was determined by a two-point probe (Sperry DM-4400A Digital Multimeter).

3. Results and discussion

Critically, using ITO as an electrode can have significant consequences to the performance of organic solar cells. ITO with PEDOT:PSS over time changes its conductivity, decreasing significantly due to etching of the ITO by PSS [30]. This results in significant efficiency drops, which is simply not viable in a solar module. Consequently, the field has been looking for an alternative solution, but even high conductivities demonstrated by nanotube thin films have yet to show success in this area [31]. The use of thin film Au demonstrates the potential of using metallic thin films. By maintaining an ultra thin film and keeping it sufficiently conductive, the layer can maintain semi-transparency across the visible spectrum making Au an attractive replacement for ITO glass.

For optimum performance a critical consideration is the adhesion of the Au films to the glass surface. Adhesion of gold to oxide surfaces such as glass (SiO_2) is poor. The metal atoms initially accumulate to form island structures during vacuum deposition because the binding forces between the metal film and the glass substrate are very weak. The thermally evaporated Au film on bare glass flakes and peels off easily. It has poor stability in various solvents such as IPA and water [32], leading to the film peeling off while spin-coating an aqueous PEDOT:PSS solution. The OPVs fabricated on this substrate possessed low efficiencies and many were electrically shorted. This problem was overcome by depositing an adhesion-promoting thin metal layer, in this case Cr, between the Au electrode and the glass substrate. This metal layer formed a covalently bonded mixed oxide at the glass–metal interface, and an alloy with gold at the electrode interface

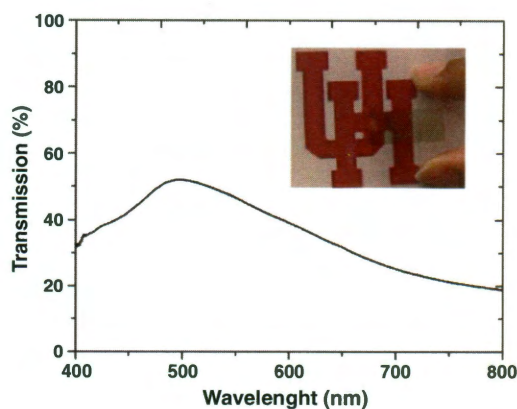


Fig. 2. The optical transmittance of an Au film with sheet resistance of $5.19 \Omega/\square$. Inset: A picture of a slide with a semi-transparent Au electrode.

creating good adhesion between the Au electrode and the glass substrate [33].

The Au film deposited using the aforementioned procedure had a sheet resistance of $5.19 \Omega/\square$ and transmittance in the range of 45–55% at 500 nm shown in Fig. 2. The AFM images of a glass slide with Au and a glass slide with Cr–Au are shown in Fig. 3. The AFM was used to

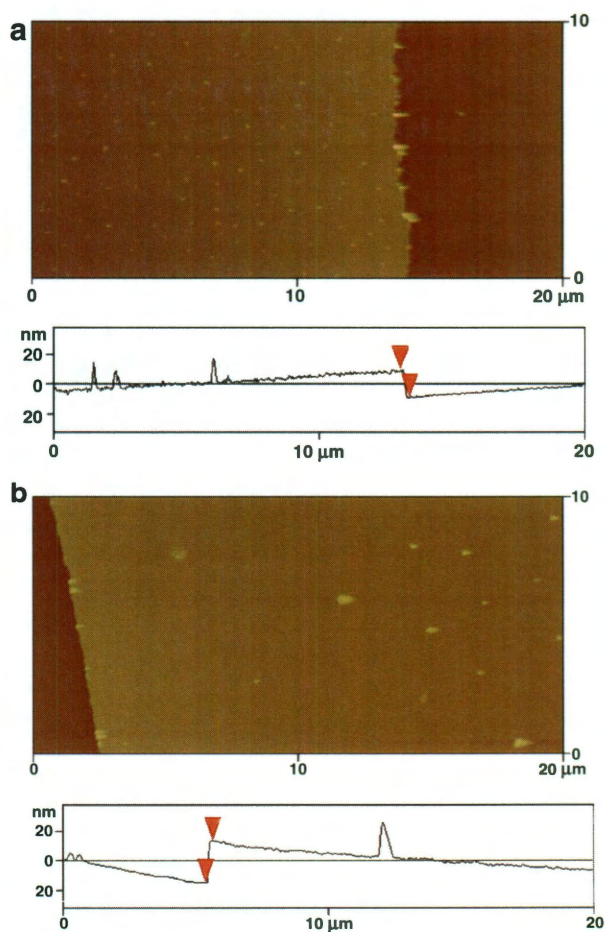


Fig. 3. Tapping mode atomic force microscopy (AFM) images ($20 \times 20 \mu\text{m}$) for surface morphology of (a) glass slide with Au film, and (b) glass slide with Cr–Au deposition.

determine the change in morphology of the Au layer due to the inclusion of a very thin adhesion promoting layer (<1 nm) of Cr between the glass substrate and Au. It is evident from Fig. 3a that a smooth film was not obtained for the bare glass substrate coated with Au, instead there were a number of randomly dispersed peak like structures (~20 nm in height). On the other hand, when thin layer of Cr was included, there were significantly fewer peaks present on the thin film surface and these peaks are less pronounced, as shown in Fig. 3b. It is clear that the morphology of the Au layer was altered by including the Cr adhesion layer. The OPVs fabricated on Au electrodes deposited on bare glass substrates displayed short circuiting or poor performances due to low shunt resistance. By incorporation of the Cr layer, the decrease in the number of shorted devices suggests that these Au peaks can more easily be covered by the PEDOT:PSS and the photoactive layer and thus do not introduce electrical shorts in the device. Improvement of device performance also suggests that these less pronounced peaks only have a minor effect to the leakage current.

Both the devices fabricated on ITO or Au coated substrates without a PEDOT:PSS layer showed poor performance. The current density–voltage (J–V) characteristics of the devices are shown in Fig. 4. The OPV with an Au anode had a J_{SC} of 1.97 mA/cm² and open circuit voltage (V_{OC}) of 0.32 V, giving a PCE of 0.24%. The OPV with an ITO anode also showed a PCE of only 0.76%. The poor performance of such devices is attributed to the formation of low resistance pathways through the film. A large number of devices with either the ITO or the Au anode were completely short-circuited. The surface roughness of both ITO and Au also results in a higher occurrence of electrical shorts across the device. This problem can be avoided using the PEDOT:PSS as an interfacial layer covering the spikes and decreasing the roughness of the underlying electrode. In addition, PEDOT:PSS enhances the wetting of the organic layer resulting in the formation of pinhole free films. This increases the shunt resistance and the device performance [34]. As the work function of Au is 5.1 eV [21], it forms an Ohmic contact with PEDOT:PSS, resulting in efficient charge transfer.

The devices fabricated on ITO and Au coated substrates using a PEDOT:PSS layer showed a significant improvement in performance. The OPVs showed increased V_{OC} , J_{SC} and FF compared to their counterparts without the PEDOT:PSS layer. The current density–voltage (J–V) characteristics of the Glass/Cr/Au/PEDOT:PSS/P3HT:PCBM/AI devices are shown in Fig. 4. A V_{OC} of 0.55 V and J_{SC} in the range of 5–7 mA/cm² was observed. The highest PCE obtained was

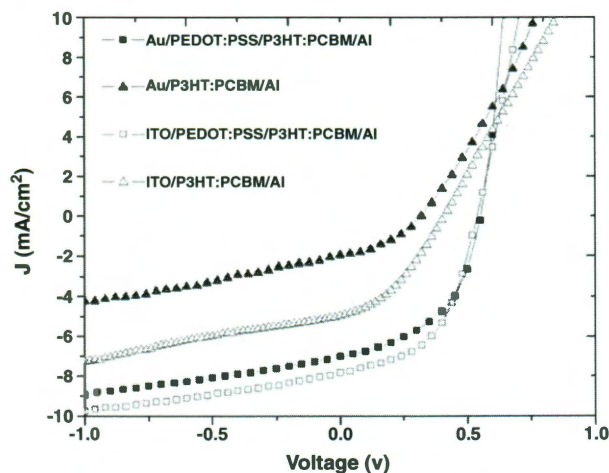


Fig. 4. The current density–voltage (J–V) characteristics under illumination with intensity of 100 mW/cm² of (a) Au anode OPV with PEDOT:PSS layer (b) Au anode OPV without the PEDOT:PSS layer (c) ITO anode with the PEDOT:PSS layer and (d) ITO anode without the PEDOT:PSS layer.

1.9% (J_{SC} = 7.01 mA/cm², V_{OC} = 0.55 V). The average PCE of the Au thin film devices was $1.2 \pm 0.3\%$ having a FF of $40 \pm 7\%$ and J_{SC} of 5.7 ± 1.1 mA/cm². The maximum value for FF was 53% and J_{SC} was 10.77 mA/cm². The J–V curves of comparison devices fabricated on ITO with PEDOT:PSS also showed an improved current generation, giving a highest PCE of 2.17%. Thus, we observe that the performance of the device with the Au anode is comparable with that of the device with ITO anode. We also determined the series resistance of the OPV devices from the slopes at V_{OC} of their J–V characteristics. The value of R_{SA} for Au anode OPV is 10.47 Ω cm² and for ITO anode OPV is 18.94 Ω cm². This is consistent with the lower sheet resistance of the Au anode (5.19 Ω/\square) as compared to that of ITO at 8–12 Ω/\square .

4. Conclusion

The objective of this work was to demonstrate that thin Au film can be an alternative semi-transparent electrode for OPV applications. We have demonstrated that an efficiency of 1.9% (J_{SC} 7.01 mA/cm², V_{OC} 0.55 V, FF 0.49) can be reached by using Au as an anode instead of ITO. Such results are particularly promising considering that the device parameters such as the thickness of the Au films have not yet been optimized.

In order to optimize the performance of the Au anode OPVs, the following criteria also need to be considered in our future work. An ideal anode material must possess high electrical conductivity and high optical transparency across the solar spectrum. However, these two requirements directly oppose each other. As the film thickness and the conductivity of the anode increases, its ability to transmit light tends to decrease significantly. A thicker Au layer with a higher conductivity leads to a lower J_{SC} and reduced solar cell performance, due to the low optical transmittance. Alternatively, a very thin Au layer, while having higher transmittance, will have also a higher series resistance at higher photo-generated currents, resulting in a reduction of FF and thus the performance. It is crucial to find an optimum thickness of the Au layer at which the combination of transmittance and sheet resistance gives the highest PCE. It would be logical to expect higher J_{SC} values for thinner conductive Au films as J_{SC} depends strongly on optical transmittance of the electrode. In addition, a large portion of the light is lost by reflection and is not transmitted by the thin metal film. Optical transmittance can be increased significantly by using a suitable anti-reflective coating. Studies focusing on reflectivity, thickness and the surface morphology of the Au layer for optimal OPV performance are currently underway.

Acknowledgment

The work is supported by the US Department of Energy under Grant no. DE-FG36-08G088008. AH would like to thank James Glennie for his valuable comments.

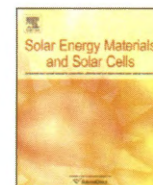
References

- [1] J.H. Burroughes, D.D.C. Bradley, A.R. Brown, R.N. Marks, K. Mackay, R.H. Friend, P.L. Burns, A.B. Holmes, *Nature* 347 (1990) 539.
- [2] N.S. Sariciftci, L. Smilowitz, A.J. Heeger, F. Wudl, *Science* 258 (1992) 1474.
- [3] S. Roth, S. Blumentritt, M. Burghard, E. Cammi, D. Carroll, S. Curran, G. Dusberg, K. Liu, J. Muster, G. Philipp, T. Rabenau, *Synth. Met.* 94 (1998) 105.
- [4] C.W. Tang, *Appl. Phys. Lett.* 48 (1986) 183.
- [5] G. Li, V. Shrotriya, J.S. Huang, Y. Yao, T. Moriarty, K. Emery, Y. Yang, *Nat. Mater.* 4 (2005) 864.
- [6] F.C. Krebs, M. Jorgensen, K. Norrman, O. Hagemann, J. Alstrup, T.D. Nielsen, J. Fyenbo, K. Larsen, J. Kristensen, *Sol. Energy Mater. Sol. Cells* 93 (2009) 422.
- [7] K.S. Liao, S.D. Yambem, A. Haldar, N.J. Alley, S.A. Curran, *Energies* 3 (2010) 1212.
- [8] G. Li, V. Shrotriya, Y. Yao, Y. Yang, *J. Appl. Phys.* 98 (2005) 043704.
- [9] S. Curran, S. Roth, A.P. Davey, A. Drury, W. Blau, *Synth. Met.* 83 (1996) 239.
- [10] M. Reyes-Reyes, K. Kim, J. Dewald, R. Lopez-Sandoval, A. Avadhanula, S. Curran, *D.L. Carroll, Org. Lett.* 7 (2005) 5749.
- [11] H.J. Peng, X.L. Zhu, J.X. Sun, Z.L. Xie, S. Xie, M. Wong, H.S. Kwok, *Appl. Phys. Lett.* 87 (2005) 3.

- [12] Indium tin oxide coated glass slide (surface resistivity 8–12 Ω/sq) from Sigma Aldrich.
- [13] Z. Chen, B. Cotterell, W. Wang, E. Guenther, S.-J. Chua, *Thin Solid Films* 394 (2001) 201.
- [14] Z. Chen, B. Cotterell, W. Wang, *Eng. Fract. Mech.* 69 (2002) 597.
- [15] Y. Leterrier, L. Medico, F. Demarco, J.A.E. Manson, U. Betz, M.F. Escola, M.K. Olsson, F. Atamny, *Thin Solid Films* 460 (2004) 156.
- [16] D.R. Cairns, G.P. Crawford, *Proc. IEEE* 93 (2005) 1451.
- [17] G.F. Wang, X.M. Tao, R.X. Wang, *Nanotechnology* 19 (2008) 145201.
- [18] J.G. Xue, S. Uchida, B.P. Rand, S.R. Forrest, *Appl. Phys. Lett.* 84 (2004) 3013.
- [19] S. Choi, W.J. Potscavage, B. Kippelen, *J. Appl. Phys.* 106 (2009) 10.
- [20] J. Liu, A.W. Hains, J.D. Servaites, M.A. Ratner, T.J. Marks, *Chem. Mater.* 21 (2009) 5258.
- [21] K. Lin, R.S. Kumar, C. Peng, S. Lu, C. Soo-Jin, A.P. Burden, *IEEE Photonics Technol. Lett.* 17 (2005) 543.
- [22] J.C. Bernede, L. Cattin, M. Morsli, Y. Berredjem, *Sol. Energy Mater. Sol. Cells* 92 (2008) 1508.
- [23] B. Kouskoussa, M. Morsli, K. Benchouk, G. Louarn, L. Cattin, A. Khelil, J.C. Bernède, *Phys. Status Solidi A* 206 (2009) 311.
- [24] R.A. Hatton, M.R. Willis, M.A. Chesters, D. Briggs, *J. Mater. Chem.* 13 (2003) 722.
- [25] A. Hadipour, B. de Boer, J. Wildeman, F.B. Kooistra, J.C. Hummelen, M.G.R. Turbiez, M.M. Wienk, R.A.J. Janssen, P.W.M. Blom, *Adv. Funct. Mater.* 16 (2006) 1897.
- [26] S. Cho, J. Yuen, J.Y. Kim, K. Lee, A.J. Heeger, *Appl. Phys. Lett.* 90 (2007) 3.
- [27] P. Varguez, F. Aviles, A.L. Oliva, *Surf. Coat. Technol.* 202 (2008) 1556.
- [28] A. Cravino, P. Schilinsky, C.J. Brabec, *Adv. Funct. Mater.* 17 (2007) 3906.
- [29] M.-S. Kim, M.-G. Kang, L.J. Guo, J. Kim, *Appl. Phys. Lett.* 92 (2008) 133301.
- [30] M.P. de Jong, L.J. van Ijzendoorn, M.J.A. de Voigt, *Appl. Phys. Lett.* 77 (2000) 2255.
- [31] S. Kim, J. Yim, X. Wang, D.D.C. Bradley, S. Lee, J.C. de Mello, *Adv. Funct. Mater.* 20 (2010) 2310.
- [32] P.A. Mosier-Boss, S.H. Lieberman, *Appl. Spectrosc.* 53 (1999) 862.
- [33] J.C. Hoogvliet, W.P. van Bennekom, *Electrochim. Acta* 47 (2001) 599.
- [34] J.C. Bernede, Y. Berredjem, L. Cattin, M. Morsli, *Appl. Phys. Lett.* 92 (2008) 083304.

Appendix D

S. D. Yambem, A. Haldar, K. S. Liao, E. P. Dillon, A. R. Barron, and S. A. Curran;
Solar Energy Materials and Solar Cells, 2011, **95**, 2424-2430.



Optimization of organic solar cells with thin film Au as anode

Soniya D. Yambem^{a,*}, Amrita Haldar^a, Kang-Shyang Liao^a, Eoghan P. Dillon^b, Andrew R. Barron^b,
Seamus A. Curran^{a,*}

^a Institute for NanoEnergy, Department of Physics, University of Houston, Houston, TX 77204, USA

^b Richard E. Smalley Institute for Nanoscale Science and Technology, Rice University, Houston, TX 77005, USA

ARTICLE INFO

Article history:

Received 9 February 2011

Received in revised form

8 April 2011

Accepted 17 April 2011

Available online 4 May 2011

Keywords:

Au thin films

Organic photovoltaics

Transparent electrode

ABSTRACT

Optical transmittance and conductivity for thin metallic films, such as Au, are two inversely related and extremely important parameters for its application in organic photovoltaics as the front electrode. We report our findings on how these parameters have been optimized to attain maximum possible efficiencies by fabricating organic solar cells with thin Au film anodes of differing optical transmittances and consequently due to scaling at the nanolevel, varying electrical conductivities. There was an extraordinary improvement in the overall solar cell efficiency (to the order of 49%) when the Au thin film transmittance was increased from 38% to 54%. Surface morphologies of these thin films also have an effect on the critical parameters including, V_{oc} , J_{sc} and FF .

© 2011 Elsevier B.V. All rights reserved.

1. Introduction

Organic photovoltaics (OPVs) have attracted significant interest in recent years, in particular since organic electronics are no longer viewed as a vague research topic but a realistic and alternative class of electronic [1,2] and optoelectronic [3–5] materials and also gained focus in industry since the demonstration of an efficient two layer organic photovoltaic cell in 1986 [6]. OPVs have several advantages over their inorganic counterparts, including solution processable fabrication at low temperatures light weight, flexibility and potentially decreasing their cost element in bulk synthesis, although this has yet to be achieved [7–10].

The fundamental structure of OPVs consists of a photoactive layer sandwiched between two electrodes of asymmetric work functions. The photoactive layer can be a single organic semiconductor layer, bilayer of an n-type (donor) and a p-type (acceptor) or a bulk heterojunction consisting of a blend of an n-type and a p-type organic semiconductor. OPVs based on the concept of the bulk heterojunction are amongst the most promising and hence extensively studied type of OPV. However, there has been recent significant and much lauded progress in p–n structures [11,12] and work done in managing the spectral absorption using nanofillers in a similar manner to that of the organic heterojunction should not be forgotten while novel architecture are likewise being explored [13,14]. In a bulk

heterojunction, and for the purpose of this study, the donor and the acceptor materials are mixed together in a solution depending on miscibility and by mole volume to determine the optimum concentrations of the constituents. This facilitates the generation of donor–acceptor interfaces in the bulk active layer (exciton dissociation site) within exciton diffusion lengths of each absorbing site and hence enhances exciton dissociation, resulting in higher photocurrent. This also maintains the need to have n and p conduction paths within the mix, in particular given current limitations in carrier mobility. In this study, we will use one of the most common donor and acceptor mixes: poly-(3-hexylthiophene) (P3HT) and [6,6]-phenyl-C₆₁-butyric acid methyl ester (PCBM), respectively.

There has been significant progress in low temperature processing [7], which allows the choice of different substrates giving mechanical flexibility to the OPVs, which then enhances options in fabrication and applications. However, this is not a trivial matter as substrate morphology, in particular those made from plastics can have varying surfaces, which can alter the thickness of the electrode layer. This is an ongoing challenge as altered conductivities at the surface will also be mirrored in the performance of the devices. In terms of the active semiconductor layer there have been many different polymers and composite mixes used in OPV fabrication in the last few years [15,16], and it seems that OPVs are essentially entering a form of Moore's law in terms of performance [17,18]. Every 6 to 9 months we have seen a change and improvement in device performance from organics and clearly it seems as we improve our chemistry and specific synthesis control, we will see this to continue. The range and flexibility available to organic chemistry will ensure that we will

* Corresponding authors.

E-mail addresses: sdymbem@mail.uh.edu (S.D. Yambem),
sacurran@mail.uh.edu (S.A. Curran).

be able to manage the semiconductor behavior by altering the HOMO–LUMO gap between p and n types to improve the V_{oc} , while better heterojunction and p–n junction systems are showing significant improvements in how both the exciton and charge carrier mobility is managed.

Predominantly OPV devices studied have the following structure: substrate/ITO/PEDOT:PSS/active organic semiconductive layer/Al, where PEDOT:PSS is poly(3,4-ethylenedioxythiophene) poly(styrenesulfonate), the higher work function electrode ITO is the anode and Al the cathode and in our case we use P3HT:PCBM as the active organic semiconductive layer. While we can add subtleties to the device architecture such as a LiF layer between Al and the organic semiconductor, one of the greatest challenges has been to manage the electrodes. The initial devices fabricated used Ca as a low workfunction metal; while the work function is significantly low it was totally impractical to use as an electrode [19]. So, in a very short period the metal of choice has been the less ideal Al electrode, although other metal such as Cr can be used as well [20]. But, except in a few instances, ITO has been the high workfunction electrode of choice. It is semitransparent in the visible region (generally 90% with suitable conductivities) and can be deposited on both glass and plastic substrates. However, ITO is a notoriously brittle electrode and there are significant challenges in cost and morphology when using this material as an electrode on any surface. During the growth phase of ITO it will form islands and this can lead to spike structures on the surface, whether the substrate is plastic or glass that can have heights in excess of 30 nm. Since OPVs require thin layers for improved device performance, this is a significant obstacle. The other significant problem with ITO is that indium, which is itself a relatively scarce material, will become ever rarer with the greater use of transparent screens for phone and other forms of electronics, while it is also a critical ingredient in manufacturing CIGS solar cell. Consequently, there is a huge need to move away from the use of ITO to a more reasonable electrode.

There has been a significant interest in using varying forms of carbon nanotubes as electrodes for multiple applications [21–23]. When transmittance is not an issue, they can be used in bulk composites for sensor and EMI shielding. If higher conductivities are required, the use of SWNT on their own or in composites is an option. This may be a very good use of them if the cost component is reduced below the costs of ITO. However, there has been a recent effort in using nanotubes or nanotube composites as electrodes in photovoltaics [24,25]. Aside from the fact that the sheet resistance is nowhere close to that required (less than $10\ \Omega$), there is also the difficulty in the HOMO match-up, which will in the end impair the V_{oc} . Additionally, because of the rough interface that will naturally occur for conductive paths to exist in connection with the active polymer layer, this will add additional resistance to the electrode as opposed to improve matters. There may be some possible use of nanotubes in the area in the future, if for instance better control over chirality happens and a better monodispersed layer is formed that has both the desired high transmittance and low sheet resistance. Perhaps, if costs can be managed even graphene could be viewed as an option, but with the current efforts this is not clear. Consequently, our approach is to look at traditional high workfunction metals such as Au in this case, to see if their sheet resistance, morphology and transmittance can be managed as an alternative to ‘transparent’ electrodes currently in vogue. In terms of achieving low sheet resistance, which is important for fabrication of large area OPVs, as well as improving mechanical flexibility, thin metal films such as Ag [26] are suitable for using as anodes. Also, complete roll to roll process of ITO-free OPV fabrication is possible using Ag nanoparticles and grids [27]. In our previous work we reported that an Au thin film is an ideal candidate for replacing ITO because of its attractive features such

as high conductivity, semi-transmittance across the visible region and ohmic contact at the anode/donor interface [28]. In addition, the use of Au in place of ITO avoids the problem of etching ITO by PEDOT:PSS [29]. An interlayer of Cr between the glass substrate and the Au film was used to increase the adhesion of Au on glass. It also reduces the roughness of the surface of Au films thereby reducing the number of pinholes and hence prevents short circuiting of the devices. The high conductivity of Au makes it very suitable for large area devices compared to ITO. However there is always a compromise between the transmittance and conductivity of the Au film. As the transmittance increases, the conductivity decreases and beyond a threshold transmittance the Au film is no longer conductive. Increase in transmittance ensures that more photons reach the photoactive layer, but decrease in conductivity will negate this positive effect. Therefore, there will be an optimum level of transmittance above which the negative effect of reducing conductivity overtakes and degrades the performance of the OPV.

In this work, we fabricated OPVs with different active layer thicknesses on Au films with the same transmittance and hence the same sheet resistance, to optimize the thickness of the active layer with respect to efficiency. Using the optimized parameters, we fabricated OPVs on Au films of different transmittances. Optimization of OPV performance with respect to thickness of the active layer and also as a function of transmittance and sheet resistance of the Au films will be presented and discussed. In addition, the surface morphologies of Au films at different transmittances were studied to understand its effect on the critical parameters.

2. Experimental section

Firstly, OPVs were fabricated on Au thin films with the same transmittance or sheet resistance. The thicknesses of the active layers were varied using different concentrations (4, 6, 9, 12, 15 and $24\ \text{g L}^{-1}$) of P3HT:PCBM and were deposited by spin coating. By keeping the spin speed constant, each concentration of P3HT:PCBM corresponds to a different thickness of the active layer.

Microscope cover-glass slides (Fisher) were used as the substrates for the deposition of thin Au films. They were cleaned by sonicating in micro-90 solution, water and isopropanol (IPA) followed by blow drying with nitrogen (N_2). Using a shadow mask, chromium (Cr, 99.9998%, Kurt Lesker) and Au (Au, 99.9999%, Kurt Lesker) were successively evaporated using a thermal evaporator at pressures $\sim 10^{-6}$ mbar. Pressure was broken between the two evaporations and separate wire baskets were used for the two metals in order to prevent cross contamination. The slides were kept under ozone plasma for 20 min and then spin coated with PEDOT:PSS (Clevios PH750, H. C. Starck, filtered through a $0.45\ \mu\text{m}$ Corning membrane filter). They were oven dried for an hour at $100\ ^\circ\text{C}$ under N_2 environment. Blends of P3HT:PCBM (Aldrich) with the same weight ratio of 1:0.66 but different concentrations, mentioned above, in anhydrous chlorobenzene were then spin coated on top of the PEDOT:PSS films. The top Al electrodes were deposited using a thermal evaporator at pressures $\sim 10^{-6}$ mbar using a shadow mask with an improved layout [30]. The OPVs were immediately encapsulated using glass slides and epoxy resins in an N_2 filled glove box with a relative humidity of $\sim 10\%$.

Secondly, four sets of Au films (1, 2, 3 and 4), with different thicknesses and hence different transmittances and sheet resistances were made using thermal evaporation and organic solar cells were made using them, in the same manner as above. A single concentration of P3HT:PCBM, $12\ \text{g L}^{-1}$, was used for making the active layer in all the four sets.

The transmittances of glass/Cr/Au slides were measured after the evaporation of the Au layer using a UV–vis spectrometer

(OCEAN OPTICS model HR2000+). For the sheet resistance calculation, the resistances across the length of the Au film were measured using a Keithley 2400 SourceMeter. The calculation is discussed in Section 3.1.

The photovoltaic characterizations of the OPVs were done in an N₂ filled glove box with a relative humidity of around 10%. The light source used was an Abet LS 150 Xenon Arc Lamp Source coupled with an AM 1.5G filter. It was calibrated with Oriol 91150V Solar Reference Si Cell certified by the National Renewable Energy Laboratory (NREL). The current–voltage (*I*–*V*) measurements of the OPVs under one sun (100 mW cm⁻²) were taken using a Keithley 2400 SourceMeter. The active areas of the OPVs were measured using a Leitz ERGOLUX microscope. Surface morphology of the different transmittance slides were studied using Digital Instrument Nanoscope IIA Atomic Force Microscope (AFM) in the tapping mode. The thicknesses of the active layers were measured using a Tencor Alpha-Step 200 Profilometer and also confirmed by a DI 3000 AFM in the tapping mode.

3. Results and discussions

3.1. Transmittance versus sheet resistance

A simple method was followed to calculate the sheet resistance. By measuring the resistance across the length of the Au film and from the dimensions of the film, the sheet resistance can be calculated. The sheet resistance R_s is then given by

$$R_s = \frac{R}{n}, \quad n = \frac{l}{b} \quad (1)$$

where R is the resistance across the length of the Au film; l and b are the length and breadth, respectively, of the Au film [31]. The average transmittance at wavelength 500 nm and their corresponding average sheet resistance of all the sets are given in Table 1.

The variation of the sheet resistances with the change in the transmittances (or thicknesses) of the Au films can be understood from the series of well defined growth stages of the film during evaporation. This pattern of film growth is seen in other metal evaporations like Cu and Ag as well [32]. In the initial stage of evaporation, the film consists of a separate nuclei [32,33]. Surface diffusion makes them move towards each other forming islands of concentrated metal dispersed across the surface of the substrate. Further evaporation, joins the islands and forms a continuous film, the longer the deposition the more the spaces between the islands are filled, until a continuous bulk layer is formed. There are two patterns to recognize here, firstly the incomplete pattern of metal deposition spread evenly across the substrate and secondly below 50 nm the transition of a metal to semiconductor due to the lower overlap of the wave functions. The first is a control problem in film deposition; the second is a phenomenological issue at the nanoscale.

At 66% transmittance the sheet resistance is as high as 511 $\Omega \square^{-1}$. Since the thickness of the Au film is ~ 10 nm, the resistivity is $\sim 511 \times 10^{-8} \Omega \text{ m}$, which is much higher than the

Table 1
Transmittance and corresponding sheet resistance of the Au films.

Set no.	Average transmittance, T (%)	Average sheet resistance, R_s ($\Omega \square^{-1}$)	Standard deviation of R_s ($\Omega \square^{-1}$)
1	66	511	390
2	60	27.9	12.5
3	54	9.07	1.81
4	38	3.19	0.27

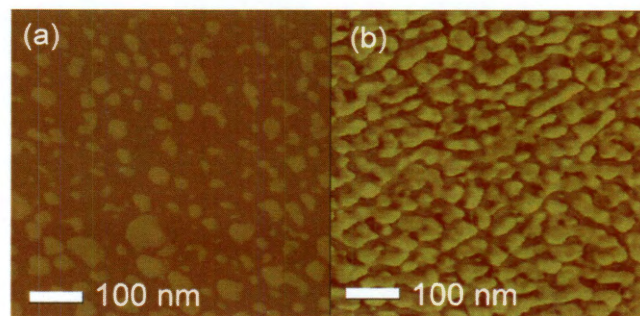


Fig. 1. AFM pictures of Au films for (a) set 1 and (b) set 2, showing the transition from an island to a bridge like network film.

resistivity of bulk Au, which is $2.44 \times 10^{-8} \Omega \text{ m}$ [34]. This corresponds to the stage of island films, which is evident from the AFM image shown in Fig. 1(a). There is no physical path for the electrons to go from one island to the other and therefore the sheet resistance is very high. However, there are contributions to the electrical conduction of island films from other mechanisms such as thermal electron emission, Schottky field emission and tunnelling emission [33]. From Table 1 we see that the standard deviation of sheet resistance is also very high, which is accounted by the fact that the conduction in this film is rather random because of the absence of a direct pathway. In comparison to the 66% transmittance film, the sheet resistance drops steeply to 27.9 $\Omega \square^{-1}$ when the transmittance is $\sim 60\%$. At this point, the Au thin film has reached a percolation threshold; the islands have grown bigger and started joining to form a bridge like network, shown in Fig. 1(b), providing a direct path for the electrons. This bridge like network does not dramatically alter the surface resistance as one would expect if we were in the microscale. Instead, the bulk conductivity of the samples is not observed as the wave function of the nanocrystals do not entirely close off the gap between the valance and conduction bands, which we will always see in bulk metals. A further decrease in transmittance does not have a very strong effect on the sheet resistance; nevertheless it does decrease to a lower value. This is because once the islands are joined and form a continuous film, further increase in the thickness has lesser contribution to the conductivity of the film. The sheet resistance is 3.19 $\Omega \square^{-1}$ for a film of transmittance $\sim 38\%$. The standard deviation of the sheet resistance decreases as the thickness (transmittance) of Au film increases (decreases) and is shown in Table 1. This is expected because the contributions of thermally activated mechanisms in the conduction of the film, which were more dominant in the island type films, decrease as the thickness increases.

3.2. Performance of OPVs

The critical parameters in determining the efficiency of an OPV are the short circuit current (J_{sc}), the open circuit voltage (V_{oc}), and the fill factor (FF). While searching for an alternative for ITO, the effect on these parameters are vital as these determine the overall performance of the OPV. The efficiency is calculated according to the formula:

$$\eta = \frac{J_{sc} \times V_{oc} \times FF}{P_{incident}} \quad (2)$$

where η stands for efficiency and $P_{incident}$ is the incident solar power.

J_{sc} depends on a number of factors including the photo-induced charge carrier density within the organic semiconductor, which in turn depends on the amount of light reaching the active

layer. Dyakonov [35] reported that there is a linear variation of the short circuit current density with light intensity. While Koster et al. [36] established a power law relationship between short circuit current density and intensity of incident light: J_{sc} is proportional to I^α , where α ranges from 0.85 to 1. The amount of photo-induced charge carrier density can also be increased by using thicker active layers.

Different types of OPVs have different factors that determine their V_{oc} . A single layer OPV follows the metal insulator metal (MIM) model, where the V_{oc} scales with the difference in the work function of the two metal electrodes [37]. For bilayer OPVs there is an intensity dependent contribution to V_{oc} in addition to its linear scaling with the difference in work function of the electrodes [38]. In bulk heterojunction solar cells the V_{oc} is determined by the difference between the highest occupied molecular orbital (HOMO) of the donor and the lowest unoccupied molecular orbital (LUMO) of the acceptor [39]. The electrode work function on either side also influences the V_{oc} [40,41]. In addition, at a particular temperature, the V_{oc} increases with increase in intensity of light [35,42].

FF is the ratio of the maximum power that can be obtained from the OPV to the theoretical power ($J_{sc} \times V_{oc}$). It is mainly affected by the series and shunt resistances, which are parasitic internal resistances of the OPV [43]. The series resistance is the sum total of the electrode resistances, interfacial and active layer resistances and the resistances due to the various contacts [44]. High series resistance decreases the FF , and hence lowers the efficiency. The shunt resistance arises due to current leakage in the OPV. Also, it has been reported that for temperatures above 100–140 K, the intensity of light weakly influences FF [35].

3.2.1. OPVs with different thicknesses of active layer

The normalized efficiencies of OPVs fabricated with different thicknesses of active layers using thin Au film (~50% transmittance at 500 nm) as anode are shown in Fig. 2. The thicknesses mentioned are the averages of thicknesses measured at different parts of the film. The number of excitons generated is greater for thicker active layers; however, low charge carrier mobilities [45]

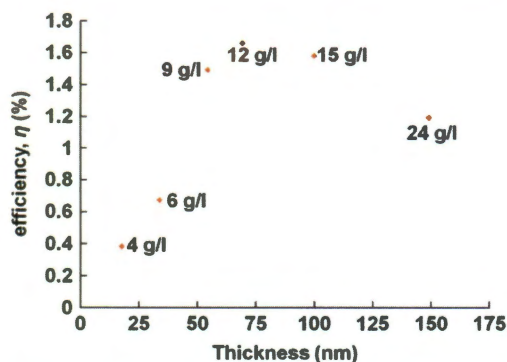


Fig. 2. Efficiencies of OPVs with different thickness of active layer.

Table 2

Highest efficiency and corresponding V_{oc} , J_{sc} and FF of OPVs fabricated on Au films of different transmittances. Average efficiency, V_{oc} , J_{sc} and FF for each set are given in the brackets.

Set no.	Transmittance, T (%)	Sheet resistance, R_s ($\Omega \square^{-1}$)	Highest efficiency, η (%)	V_{oc} (V)	J_{sc} (mA cm^{-2})	FF
1	66	511	1.06 (1.03)	0.49 (0.48)	4.64 (4.74)	0.46 (0.45)
2	60	27.9	1.59 (1.43)	0.58 (0.57)	5.61 (5.44)	0.49 (0.46)
3	54	9.07	1.83 (1.51)	0.55 (0.54)	6.75 (6.00)	0.49 (0.47)
4	38	3.19	1.23 (1.10)	0.53 (0.53)	5.64 (4.85)	0.41 (0.43)

and short exciton diffusion lengths [46] of the organic molecules limit the efficiency of the OPVs. This leads to a dichotomy, whereby the better performance in terms of exciton diffusion is an ultra-thin layer, while a greater number of excitons will be generated through thick films. In addition, using the heterojunction effect will mean that once we generate the exciton the carriers can be moved on through their respective preferred carrier type (p or n), it is still better in those terms to have a thinner layer. Therefore an optimum thickness of the active layer, which balances all parameters is important to obtain the maximum possible efficiency of an OPV. The optimum weight ratio of P3HT (donor) and acceptor PCBM (acceptor) depends on the thickness of the active layer [47,48]. On the other hand, the optimum thickness of active layer also depends on the weight ratio of P3HT and PCBM [48]. There are various reports of optimum thicknesses for different weight ratios of P3HT:PCBM. For a weight ratio of 1:1, the optimum thickness of active layer was reported to be 225 nm by Moule et al. [47], while according to Li et al. it is ~63 nm. Moule et al. [47] also showed that as the thickness of active layer increases the optimum percentage of PCBM increases while the opposite result has been obtained by Reyes-Reyes et al. [48]. Furthermore, Alstrup et al. [49] demonstrated that the efficiency increases throughout the thickness range of 0–800 nm. The disagreements in the various results might be attributed to the fact that the device fabrication processes and the optimization conditions were different in each case. The mentioned reports are for devices fabricated on ITO. For our OPVs on Au, we optimized the thickness of the active layer for a P3HT:PCBM weight ratio of 1:0.66. Devices were fabricated with a variation in the active layer thickness from 18 to 149 nm. The highest efficiency of 1.66% was obtained for an active layer thickness of ~69 nm (shown in Fig. 2). Having obtained this optimized thickness of the active layer, we proceed to the next stage of optimization using different Au films of different transmittances.

3.2.2. OPVs on Au films of different transmittances

Using the optimum thickness of photoactive layer obtained from Section 3.2.1 we fabricated OPVs on four sets of Au films with different transmittances. Table 2 gives the efficiencies of the most efficient device of each set of OPVs and their corresponding V_{oc} , J_{sc} and FF . The highest efficiency of 1.83% was obtained for Au film of transmittance 54%. It can be seen from Table 2, that all the critical parameters change with the change in transmittance of the Au films. Thus variation in the efficiency with transmittance has contributions from all the three critical parameters. The average efficiencies and the average V_{oc} , J_{sc} and FF of devices in each set (given in brackets in Table 2), taken over at least four devices, show a similar trend to the one for the highest efficiencies of each set. The variation in the critical parameter is explained by the following two factors. Firstly, the change in sheet resistances, which accounts for changes in series resistances. Since all other fabrication parameters of the OPVs are constant there would be a reduction in series resistance from set

1 to set 4 solely due to the decrease in the sheet resistances (Table 1). Secondly, the decrease in light intensity reaching the active layer, which arises due to the decrease in transmittance (Table 1) of the Au films.

From set 1 to set 2, the V_{oc} increases by almost 100 mV, and then decreases very gradually for the remaining two sets (set 3 and set 4). The decrease in V_{oc} from set 2 to set 4 is explained by the decrease in light intensity reaching the active layer. Koster et al. demonstrated that at a constant temperature, the V_{oc} when plotted as a function of light intensity has a constant positive slope (equal to kT/q , where k , T and q are the Boltzmann constant, temperature and elementary charge, respectively) [42]. This is probably the cause for the decrease in V_{oc} from 0.57 to 0.53 V as percentage of light reaching the active layer decreases from 60% to 38% as we go from set 2 to set 4. However, this does not explain the change in V_{oc} from set 1 to set 2. It has been shown that for metal thin films such as Cu, the work function increases with increase in film thickness and stays constant after a critical thickness [50]. Au films may also have a similar trend for its work function since Au and Cu have similar growth stages of deposition [32]. Hence it may be speculated that the work function of the Au film for set 1 is significantly lower than the rest of the sets because the film for set 1 is an island film (Fig. 1(a)) while for a set with higher transmittance it is a bridge network film as seen in Fig. 1(b). This accounts for the change in V_{oc} from set 1 to set 2.

As a result of decrease in series resistance J_{sc} should increase monotonically from set 1 to set 4. However, to the contrary, there should be a monotonic decrease in J_{sc} because of lesser intensity of light reaching the active layer from set 1 to set 4. The opposing effects of the two factors gave an optimum point of J_{sc} at Au film transmittance of 54%, which has a corresponding J_{sc} 6.75 mA cm^{-2} . The effect of series resistance is dominant for the OPVs fabricated with Au films with higher transmittance (set 1 and set 2) and we can see a monotonic increase in J_{sc} from set 1 to set 3 (Table 2). While for OPVs fabricated on Au films with lower transmittance

(set 4) the effect of light intensity is more pronounced and hence J_{sc} decreases.

From set 1 to set 4, there are variations in multiple parameters, which affect FF , such as the intensity of light, the sheet resistance and the morphology of the electrodes. FF is higher for the two middle sets, set 2 and set 3 (Table 2). In this case, the morphology of the anode seems to have taken dominance over the influence of variation in light intensity and sheet resistance. Surface morphologies of Au films as revealed by atomic force microscopy are shown in Fig. 3. Evaporated Au films may yield a surface containing peaks with a sharp profile. These peaks can act as leakage paths for the currents and reduce the shunt resistance, and hence FF of the OPV. From the AFM pictures we see that there is a variation in the density and the height of peaks in the Au films of all the sets. The Au film arranged in order of increasing density of peaks is: set 3 < set 4 < set 1 < set 2. And arranged in order of increasing height of peaks is: set 2 < set 1 < set 4 < set 3. On the basis that the density of peaks as well as the height of the peaks contribute equally to the leakage current, set 2 and set 3 should have lesser leakage current and hence higher FF . This can be better understood from the schematics of AFM images in Fig. 4. Fig. 4(a) represents a monodispersed Au film with high density but short Au spikes, which corresponds to set 2. Fig. 4(b) represents an Au film with sporadic tall Au spikes, which corresponds to set 3. Fig. 4(c) represents an Au film with moderate density and medium height Au spikes, which corresponds to sets 1 and 4. Both the density and height of spikes contribute to the leakage current. FF of OPVs fabricated on Au films with schematics given in Fig. 4(a) and (b) will have a higher FF than OPVs fabricated on Au films, which correspond to Fig. 4(c). And this is exactly what is seen in FF of the OPVs fabricated with different Au films (Table 2).

However, surface roughness of the Au films is rather random and shows no correlation with the thickness of the films. Similar features have been observed for Ag thin films as well where the surface roughness is independent of the thickness of the film [26].

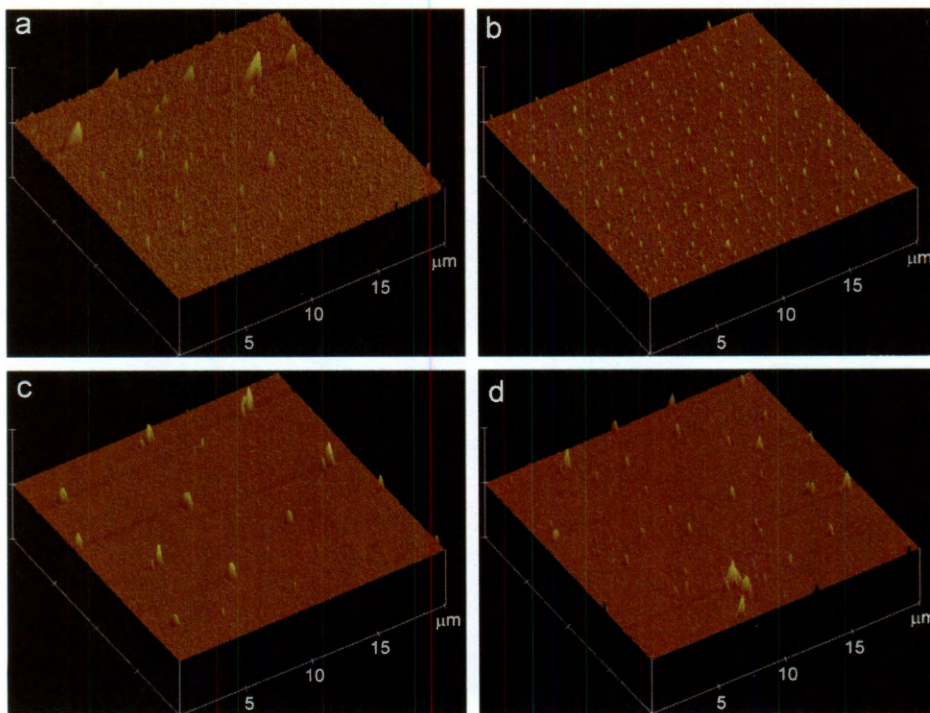


Fig. 3. Surface morphology of the Au films: (a) set 1, 66% T, (b) set 2, 60% T (c) set 3, 53% T and (d) set 4, 38% T.

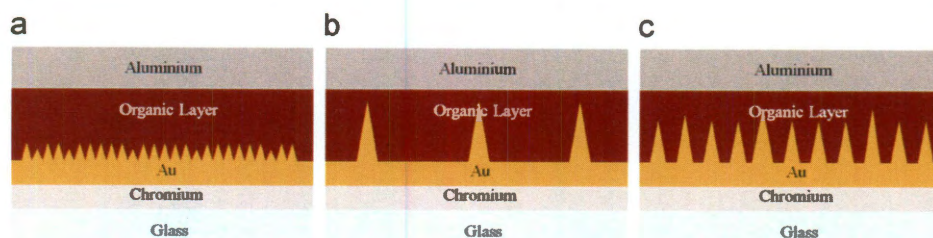


Fig. 4. Schematics of AFM images: (a) corresponds to set 2, (b) corresponds to set 3 and (c) corresponds to sets 1 and 4.

The only noticeable change is the comparative reduction in density of peaks with thicker films; set 3 and set 4 as compared to set 1 and set 2 (Fig. 3).

Critically the challenge in using Au as opposed to a more traditional electrode material such as ITO is feasible. But, the issues with ITO such as sporadic island formation can also occur with Au. In this case, however, by forming bridges between the islands in a percolation form, we get a better electrode. The real challenge is to reduce the formation of island and have a more controlled thin film deposition and consequently better connectivity along the electrode. It may even mean we can work with a thinner electrode and reduce the reflection. The use of thin metal films in OPV is not exclusive to Au and investigations of other thin metals films, which can potentially replace ITO are being carried out. Furthermore, Au being a noble metal, devices fabricated on thin Au films are expected to be more stable than those fabricated on ITO. Ongoing work is proceeding towards a study of the stability of the devices fabricated on Au thin films.

4. Conclusion

We have shown that the optimum thickness of P3HT:PCBM (1.0:0.66) active layer is ~ 69 nm for OPVs fabricated using Au thin films as the anode. Using this optimization, we fabricated OPVs on Au films with different transmittances. With the increase in transmittance of Au films there is a compromise on the sheet resistance of the film. The variation in transmittance of Au films affects the critical parameters and hence the efficiency of an OPV. An optimum is obtained beyond which the increase in sheet resistance overtakes the positive effect of increase in transmittance. The best OPV obtained has an efficiency of 1.83% and this corresponds to a thin Au film with 54% transmittance. This is an increase of 49% in the efficiency compared to OPV fabricated on Au films of 38% transmittance. Further improvement in the efficiency may be obtained with a more controlled deposition technique to reduce the sharp peaks of the Au films. The lifetime of OPVs with Au as anodes is yet to be investigated. Use of Au anode on flexible substrates like plastic would have applications on designs of OPVs, which does not use the flat panel architecture.

Acknowledgment

This work is supported by the US Department of Defense under Grant no. DD-N000141110069.

References

[1] J.H. Burroughes, D.D.C. Bradley, A.R. Brown, R.N. Marks, K. Mackay, R.H. Friend, P.L. Burns, A.B. Holmes, Light-emitting-diodes based on conjugated polymers, *Nature* 347 (1990) 539–541.
 [2] S.R. Forrest, The path to ubiquitous and low-cost organic electronic applications on plastic, *Nature* 428 (2004) 911–918.

[3] S. Roth, S. Blumentritt, M. Burghard, E. Cammi, D. Carroll, S. Curran, G. Düsberg, K. Liu, J. Muster, G. Philipp, T. Rabenau, Molecular rectifiers and transistors based on [pi]-conjugated materials, *Synth. Met.* 94 (1998) 105–110.
 [4] S.A. Curran, P.M. Ajayan, W.J. Blau, D.L. Carroll, J.N. Coleman, A.B. Dalton, A.P. Davey, A. Drury, B. McCarthy, S. Maier, A. Strevens, A composite from poly(m-phenylenevinylene-co-2,5-dioctoxy-p-phenylenevinylene) and carbon nanotubes: a novel material for molecular optoelectronics, *Adv. Mater.* 10 (1998) 1091–1093.
 [5] T. Kamata, S. Curran, S. Roth, T. Fukaya, H. Matsuda, F. Mizukami, Third-order nonlinear optical properties of evaporated thin films of platinum-alkyldionedioxime complexes: effects of metal–metal distance, *Synth. Met.* 83 (1996) 267–271.
 [6] C.W. Tang, 2-Layer organic photovoltaic cell, *Appl. Phys. Lett.* 48 (1986) 183–185.
 [7] G. Li, V. Shrotriya, J.S. Huang, Y. Yao, T. Moriarty, K. Emery, Y. Yang, High-efficiency solution processable polymer photovoltaic cells by self-organization of polymer blends, *Nat. Mater.* 4 (2005) 864–868.
 [8] F.C. Krebs, T. Tromholt, M. Jorgensen, Upscaling of polymer solar cell fabrication using full roll-to-roll processing, *Nanoscale* 2 (2010) 873–886.
 [9] F.C. Krebs, T.D. Nielsen, J. Fyenbo, M. Wadstrom, M.S. Pedersen, Manufacture, integration and demonstration of polymer solar cells in a lamp for the Lighting Africa initiative, *Energy Environ. Sci.* 3 (2010) 512–525.
 [10] F.C. Krebs, J. Fyenbo, M. Jorgensen, Product integration of compact roll-to-roll processed polymer solar cell modules: methods and manufacture using flexographic printing, slot-die coating and rotary screen printing, *J. Mater. Chem* 20 (2010) 8994–9001.
 [11] J.G. Xue, S. Uchida, B.P. Rand, S.R. Forrest, 4.2% Efficient organic photovoltaic cells with low series resistances, *Appl. Phys. Lett.* 84 (2004) 3013–3015.
 [12] F. Yang, K. Sun, S.R. Forrest, Efficient solar cells using all-organic nanocrystalline networks, *Adv. Mater.* 19 (2007) 4166–4171.
 [13] S. Curran, J. Talla, S. Dias, J. Dewald, Microconcentrator photovoltaic cell (the m-C cell): modeling the optimum method of capturing light in an organic fiber based photovoltaic cell, *J. Appl. Phys* 104 (2008) 064305-1–064305-6.
 [14] W.U. Huynh, J.J. Dittmer, A.P. Alivisatos, Hybrid nanorod-polymer solar cells, *Science* 295 (2002) 2425–2427.
 [15] W.T. Wong, S.A. Curran, A study of C-60-poly(m-phenylenevinylene-co-2,5-dioctoxy-p-phenylenevinylene) nanocomposite, *Thin Solid Films* 515 (2006) 2393–2397.
 [16] S. Curran, S. Roth, A.P. Davey, A. Drury, W. Blau, Photoconduction and photovoltaic effects from a conjugated polymer poly-tert-butyl-isothionaphthalene, *Synth. Met.* 83 (1996) 239–243.
 [17] M.A. Green, K. Emery, Y. Hishikawa, W. Warta, Solar cell efficiency tables (version 36), *Prog. Photovolt: Res. Appl.* 18 (2010) 346–352.
 [18] M.A. Green, K. Emery, Y. Hishikawa, W. Warta, Solar cell efficiency tables (version 37), *Prog. Photovolt: Res. Appl.* 19 (2011) 84–92.
 [19] Y.S. Eo, H.W. Rhee, B.D. Chin, J.-W. Yu, Influence of metal cathode for organic photovoltaic device performance, *Synth. Met.* 159 (2009) 1910–1913.
 [20] M. Manceau, D. Angmo, M. Jorgensen, F.C. Krebs, ITO-free flexible polymer solar cells: from small model devices to roll-to-roll processed large modules, *Org. Electron.* 12 (2011) 566–574.
 [21] K.S. Liao, J.A. Talla, S.D. Yambem, D. Bix, G. Chen, F. Coldren, D.L. Carroll, L.J. Ci, P.M. Ajayan, D.H. Zhang, S.A. Curran, Formation of highly conductive composite coatings and their applications to broadband antennas and mechanical transducers, *J. Mater. Res.* 25 (2010) 1741–1747.
 [22] S.A. Curran, J. Talla, S. Dias, D.H. Zhang, D. Carroll, D. Bix, Electrical transport measurements of highly conductive carbon nanotube/poly(bisphenol A carbonate) composite, *J. Appl. Phys.* 105 (2009) 073711-1–073711-5.
 [23] Y.J. Jung, S. Kar, S. Talapatra, C. Soldano, G. Viswanathan, X.S. Li, Z.L. Yao, F.S. Ou, A. Avadhanula, R. Vajtai, S. Curran, O. Nalamasu, P.M. Ajayan, Aligned carbon nanotube-polymer hybrid architectures for diverse flexible electronic applications, *Nano Lett.* 6 (2006) 413–418.
 [24] M.W. Rowell, M.A. Topinka, M.D. McGehee, H.J. Prall, G. Dennler, N.S. Sariciftci, L.B. Hu, G. Gruner, Organic solar cells with carbon nanotube network electrodes, *Appl. Phys. Lett.* 88 (2006) 233506-1–233506-3.
 [25] R.C. Tenent, T.M. Barnes, J.D. Bergeson, A.J. Ferguson, B. To, L.M. Gedvilas, M.J. Heben, J.L. Blackburn, Ultrasoft, large-area, high-uniformity, conductive transparent single-walled-carbon-nanotube films for photovoltaics produced by ultrasonic spraying, *Adv. Mater.* 21 (2009) 3210–3216.

- [26] B. O'Connor, C. Haughn, K.H. An, K.P. Pipe, M. Shtein, Transparent and conductive electrodes based on unpatterned, thin metal films, *Appl. Phys. Lett.* 93 (2008) 223304-1–223304-3.
- [27] F.C. Krebs, All solution roll-to-roll processed polymer solar cells free from indium-tin-oxide and vacuum coating steps, *Org. Electron.* 10 (2009) 761–768.
- [28] A. Haldar, S.D. Yambem, K.S. Liao, N.J. Alley, E.P. Dillon, A.R. Barron, S.A. Curran, Organic photovoltaics using thin gold film as an alternative anode to indium tin oxide, *Thin Solid Films*, in press, doi:10.1016/j.tsf.2011.1004.1071.
- [29] M.P. de Jong, L.J. van Ijzendoorn, M.J.A. de Voigt, Stability of the interface between indium-tin-oxide and poly(3,4-ethylenedioxythiophene)/poly(styrenesulfonate) in polymer light-emitting diodes, *Appl. Phys. Lett.* 77 (2000) 2255–2257.
- [30] K.-S. Liao, S. Dias, N.J. Alley, S.D. Yambem, A. Haldar, S.A. Curran, Design and fabrication of linear pixel arrays for organic photovoltaic modules to achieve scalable power output, *Thin Solid Films* 519 (2011) 3264–3267.
- [31] M.H.J. Lee, R.J. Collier, Sheet resistance measurement of thin metallic films and stripes at both 130 GHz and DC, *IEEE Trans. Instrum. Meas.* 54 (2005) 2412–2415.
- [32] C.G. Granqvist, Transparent conductors as solar energy materials: a panoramic review, *Sol. Energy Mater. Sol. Cells* 91 (2007) 1529–1598.
- [33] G.P. Zhirgalskii, B.K. Jones, *The Physical Properties of Thin Metal Films*, Taylor & Francis, London, 2003, pp. 35–51.
- [34] J.D. Cutnell, K.W. Johnson, *Physics*, fourth ed., Wiley, New York, 1998.
- [35] V. Dyakonov, Electrical aspects of operation of polymer-fullerene solar cells, *Thin Solid Films* 451 (2004) 493–497.
- [36] L.J.A. Koster, V.D. Mihailetschi, H. Xie, P.W.M. Blom, Origin of the light intensity dependence of the short-circuit current of polymer/fullerene solar cells, *Appl. Phys. Lett.* 87 (2005) 203502.
- [37] J. Liu, Y.J. Shi, Y. Yang, Solvation-induced morphology effects on the performance of polymer-based photovoltaic devices, *Adv. Funct. Mater.* 11 (2001) 420–424.
- [38] C.M. Ramsdale, J.A. Barker, A.C. Arias, J.D. MacKenzie, R.H. Friend, N.C. Greenham, The origin of the open-circuit voltage in polyfluorene-based photovoltaic devices, *J. Appl. Phys.* 92 (2002) 4266–4270.
- [39] M.C. Scharber, D. Wuhlbacher, M. Koppe, P. Denk, C. Waldauf, A.J. Heeger, C.L. Brabec, Design rules for donors in bulk-heterojunction solar cells—towards 10% energy-conversion efficiency, *Adv. Mater.* 18 (2006) 789–794.
- [40] V.D. Mihailetschi, P.W.M. Blom, J.C. Hummelen, M.T. Rispen, Cathode dependence of the open-circuit voltage of polymer:fullerene bulk heterojunction solar cells, *J. Appl. Phys.* 94 (2003) 6849–6854.
- [41] H. Frohne, S.E. Shaheen, C.J. Brabec, D.C. Müller, N.S. Sariciftci, K. Meerholz, Influence of the anodic work function on the performance of organic solar cells, *ChemPhysChem* 3 (2002) 795–799.
- [42] L.J.A. Koster, V.D. Mihailetschi, R. Ramaker, P.W.M. Blom, Light intensity dependence of open-circuit voltage of polymer:fullerene solar cells, *Appl. Phys. Lett.* 86 (2005) 123509-1–123509-3.
- [43] K.S. Liao, S.D. Yambem, A. Haldar, N.J. Alley, S.A. Curran, Designs and architectures for the next generation of organic solar cells, *Energies* 3 (2010) 1212–1250.
- [44] J.D. Servaites, S. Yeganeh, T.J. Marks, M.A. Ratner, Efficiency enhancement in organic photovoltaic cells: consequences of optimizing series resistance, *Adv. Funct. Mater.* 20 (2010) 97–104.
- [45] P.W.M. Blom, M.J.M. de Jong, M.G. van Munster, Electric-field and temperature dependence of the hole mobility in poly(p-phenylene vinylene), *Phys. Rev. B* 55 (1997) R656–R659.
- [46] P. Peumans, S.R. Forrest, Very-high-efficiency double-heterostructure copper phthalocyanine/C-60 photovoltaic cells, *Appl. Phys. Lett.* 79 (2001) 126–128.
- [47] A.J. Moule, J.B. Bonekamp, K. Meerholz, The effect of active layer thickness and composition on the performance of bulk-heterojunction solar cells, *J. Appl. Phys.* 100 (2006) 094503-1–094503-7.
- [48] M. Reyes-Reyes, K. Kim, J. Dewald, R. Lopez-Sandoval, A. Avadhanula, S. Curran, D.L. Carroll, Meso-structure formation for enhanced organic photovoltaic cells, *Org. Lett.* 7 (2005) 5749–5752.
- [49] J. Alstrup, M. Jørgensen, A.J. Medford, F.C. Krebs, Ultra fast and parsimonious materials screening for polymer solar cells using differentially pumped slot-die coating, *ACS Appl. Mater. Interfaces* 2 (2010) 2819–2827.
- [50] J. Vancea, G. Reiss, D. Butz, H. Hoffmann, Thickness-dependent effects in the work function of polycrystalline Cu-films, *Europhys. Lett.* 9 (1989) 379–384.

Appendix E

S. J. Corr, L. O'Reilly, E. P. Dillon, A. R. Barron, and P. J. McNally, *J. Raman Spectroscopy*, published online, **2011**.

Poly(vinylpyrrolidone)-stabilized silver nanoparticles for strained-silicon surface enhanced Raman spectroscopy

Stuart J. Corr,^{a,b*} † Lisa O'Reilly,^a Eoghan P. Dillon,^b Andrew R. Barron^b and Patrick J. McNally^a



Poly(vinylpyrrolidone)-stabilized silver nanoparticles deposited onto strained-silicon layers grown on graded Si_{1-x}Ge_x virtual substrates are utilized for selective amplification of the Si–Si vibration mode of strained silicon via surface-enhanced Raman scattering spectroscopy. This solution-based technique allows rapid, highly sensitive and accurate characterization of strained silicon whose Raman signal would usually be overshadowed by the underlying bulk SiGe Raman spectra. The analysis was performed on strained silicon samples of thickness 9, 17.5 and 42 nm using a 488 nm Ar⁺ micro-Raman excitation source. The quantitative determination of strained-silicon enhancement factors was also made. Copyright © 2011 John Wiley & Sons, Ltd.

Supporting information may be found in the online version of this article.

Keywords: plasmonics; strained-silicon; SERS; silver nanoparticles; polyol

Introduction

Strained silicon (ϵ -Si) layers epitaxially grown on lattice-mismatched, graded silicon–germanium (Si_{1-x}Ge_x) virtual substrates are becoming extremely important for high-frequency microelectronics applications. Used for the channel region of metal-oxide field-effect transistors, these ϵ -Si structures have been demonstrated to improve the charge carrier transport properties compared to bulk silicon,^[1] leading to faster computer chip performance with lower energy consumption. These nanometer-thick ϵ -Si layers must be accurately characterized in order to have tight control over transistor properties. Micro-Raman spectroscopy is a nondestructive tool that can be used for ϵ -Si characterization, but it must be used with low-penetration-depth excitation lasers (usually in the ultraviolet (UV) range) to prevent the underlying bulk SiGe signal from overwhelming the weak ϵ -Si signal.

Micro-Raman studies investigating ϵ -Si characterization using a variety of laser sources and techniques have shown promising results.^[2–5] Although it has been shown that expensive UV (325 nm) laser sources with shallow penetration depths (\sim 9 nm) and low wavenumber resolution are capable of nondestructive strain investigation,^[2,5] longer wavelengths (e.g. 514.5 nm), although possessing greater wavenumber resolution, penetrate deep into the bulk substrate (\sim 770 nm^[6]) resulting in the SiGe peak overshadowing the inherently weak ϵ -Si signal. Hence, ϵ -Si analysis at these wavelengths has to be done either with accurate curve-fitting algorithms (which can be difficult, especially for 17.5-nm ϵ -Si samples as no obvious ϵ -Si peak can be found) or with a combination of etching and software deconvolution techniques to separate this weak ϵ -Si signal.^[4] The ability to accurately map ϵ -Si layers using a nondestructive technique at wavelengths longer than 325 nm is imperative for higher resolution strain mapping and characterization. These limitations provide good reasons for the

use of surface-enhanced Raman scattering (SERS) spectroscopy techniques.

Previous work by Hayazawa *et al.*^[7] has shown selective enhancement of ϵ -Si layers via SERS using direct thermal evaporation techniques. However, with the standard size of silicon wafers reaching 300 mm, which is comparable to the diameter of standard evaporation chambers, this could prove problematic for rapid onsite semiconductor characterization protocols. Previous research has also found evaporation techniques to be highly sensitive to parameters such as substrate-to-target height, pressure and evaporation temperature.^[8] This limits the reproducibility of ϵ -Si SERS characterization. With this in mind, an alternative solution-based SERS technique has been investigated that would enable small areas ($<$ 1 mm²) of ϵ -Si to be characterized via a silver (Ag) nanoparticle (NP) solution.

Experimental

In this experiment, poly(vinylpyrrolidone) (PVP) stabilized Ag NPs of diameter 33–147 nm synthesized via the polyol process^[9] were deposited on 9-, 17.5-, and 42-nm thick ϵ -Si substrates

* Correspondence to: Stuart J. Corr, Nanomaterials Processing Laboratory, (The RINCE Institute), Dublin City University, Dublin 9, Ireland. E-mail: sjcorr@gmail.com

† Present address: Rice University, Department of Chemistry, MS-60, 6100 Main Street, Houston, TX 77005-1892.

^a Nanomaterials Processing Laboratory, (The RINCE Institute), Dublin City University, Dublin 9, Ireland

^b The Richard E. Smalley Institute for Nanoscale Science and Technology, Rice University, Houston, TX 77005, USA

($\text{Si}_{0.7}\text{Ge}_{0.3}$, $\text{Si}_{0.8}\text{Ge}_{0.2}$, and $\text{Si}_{0.8}\text{Ge}_{0.2}$, respectively) and tested for SERS enhancements. The polyol process involves the preparation of NPs by reduction of inorganic compounds in liquid polyols. Originally developed by Fievet *et al.*,^[10] it is a simple solution-phase synthesis technique for metallic and alloy colloidal NPs. The standard reaction involves the reduction of an inorganic salt by a polyol such as ethylene glycol at an elevated temperature (140–170 °C). By introducing stabilizing agents such as PVP, a variety of NP morphologies can be formed, such as spherical, cubic and triangular.^[9–12] Although other techniques such as citrate-reduction protocols can be used for NP synthesis,^[13] they do not allow such tight control over the NP morphology. Details of the protocol used for this experiment can be found in the literature.^[9]

Once a typical synthesis was carried out, the NPs were removed from the supernatant via centrifugation and washed with deionized (DI) water several times to remove the excess surfactant. The final NPs were suspended in 10 ml of DI water. For SERS and scanning transmission electron microscopy (STEM) analysis, 10 μl of the solution was directly deposited on top of the ϵ -Si substrates and allowed to dry at room temperature. A metallic, uniform, bronze-like film was evident after the water had evaporated. This droplet covered an area of $\sim 1 \text{ mm}^2$. Subsequent STEM analysis (which illustrated a good degree of the NP uniformity across the sample) estimated ϵ -Si coverage to be $\sim 100 \text{ NPs}/\mu\text{m}^2$. SERS spectra were obtained on areas that exhibited little deviation across the laser spot size using the integrated micro-Raman optical imaging camera as a visual reference.

SERS measurements were performed on a Jobin Yvon LabRam HR800 micro-Raman system in backscattering geometry using the 488-nm Ar^+ laser excitation ($\sim 20 \text{ mW}$) at room temperature. A $50\times$ objective (NA 0.75) was used which gave a laser spot size diameter of $\sim 4 \mu\text{m}$ (determined by measuring the diameter of the observed focal spot shown via the integrated optical camera). A liquid-nitrogen-cooled charged coupled device detector was also used to detect the Raman signals via the same objective using a confocal hole of $200 \mu\text{m}$ and a grating of 2400 g/mm . The equipment was calibrated first using the 520 cm^{-1} Raman peak from a strain-free reference silicon substrate. Raman spectra were collected for all ϵ -Si samples before NP deposition for comparison. Peak-fitting was done via a double Lorentian peak fit using both the SiGe and ϵ -Si Raman peaks to an accuracy of 0.04 cm^{-1} . Post measurement, the peak positions were adjusted with reference to an internal 332-nm neon emission line.

For rapid SERS characterization, a new technique was developed that performed a series of micro-Raman xy mapping scans so that certain areas could be examined more thoroughly to highlight maximum SERS enhancements. For each sample, a $100 \mu\text{m}^2$ area scan (50 points, 10 s, 30 accumulations) was first taken and mapped, and then another 50-point scan was taken across a smaller area of $25 \mu\text{m}^2$ where the highest SERS intensities were visible (Fig. 1). This ultimately meant that the largest SERS enhancement across an area of $100 \mu\text{m}^2$ could be found. All Ag NP samples were first tested on 17.5-nm thick ϵ -Si substrates. Strained-silicon samples of thickness 9 and 42 nm were then investigated using the Ag NPs exhibiting the greatest SERS enhancements. All Raman spectra were intensity-normalized to their SiGe peak at 5000 arb. units, as the SiGe peak intensities were attenuated by up to $\sim 25\%$ after Ag NP coverage.

NP size and morphology were examined using a Hitachi S-5550 microscope operating in the STEM mode at 20 kV at a working distance of 0.7–0.8 mm. Appropriate software was used

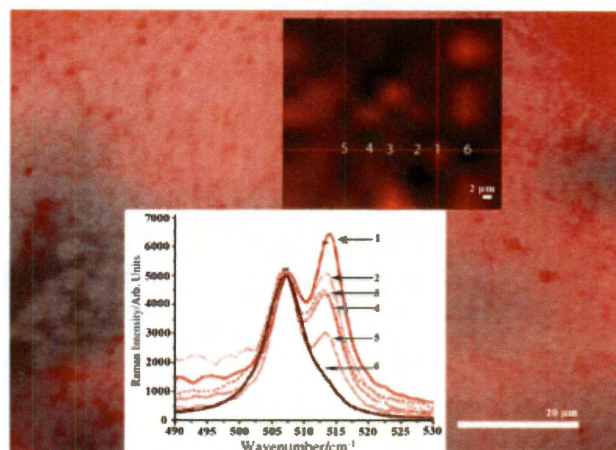


Figure 1. Micro-Raman optical image of Ag NP coverage on 17.5 nm ϵ -Si (black and white image, $20 \mu\text{m}$ scale). Superimposed on top are areas of 17.5-nm SERS enhancements shown by varying the red intensities (bright red being the largest SERS enhancement, black being equal to the non-SERS Raman spectra). A smaller area was then scanned (top right-hand corner, $2 \mu\text{m}$ scale) with SERS enhancements superimposed. Final Raman spectra of points 1–6 are shown in the bottom right-hand spectrum. Point 1 shows the largest SERS enhancement (thick red); point 6 is equal to the non-SERS spectrum (black). SERS SiGe peak is located at $506.98 \pm 0.33 \text{ cm}^{-1}$, while SERS ϵ -Si peaks are located at $513.33 \pm 0.37 \text{ cm}^{-1}$. Standard deviation bars also shown.

to develop histogram charts to determine mean NP size and standard deviation.

Results and Discussion

From STEM measurements, the average NP size for each sample was 33 ± 11 , 78 ± 19 , 80 ± 18 and $147 \pm 38 \text{ nm}$ corresponding to sample numbers 1–4, respectively. Figure 1 depicts five random SERS micro-Raman spectra for sample 3 NPs deposited onto 17.5-nm thick ϵ -Si ($\text{Si}_{0.8}\text{Ge}_{0.2}$) and also includes non-SERS spectra for comparison (point 6). Figure 1 also highlights the technique employed to obtain maximum SERS enhancements across the sample area. Overall, sample 3 gave the greatest SERS enhancement, although sample 2 SERS spectra were similar, which would be expected as their histogram profiles are almost identical. The SERS spectra for samples 1, 2 and 4 along with their corresponding histogram profiles are shown in Figs S1–S4 (Supporting Information). As sample 3 NPs displayed the greatest SERS enhancements, these were then applied to the 9- and 42-nm ϵ -Si samples. Their corresponding SERS spectra are shown in Fig. 2, where, although there were ϵ -Si intensity variations similar to those depicted in Fig. 1, only the largest SERS enhancements are shown. A STEM image of sample 3 NPs is also shown in Fig. S5 (Supporting Information). Equation (1) was used to calculate biaxial tensile strain^[13]:

$$\sigma_{xx} = \sigma_{yy} = \frac{-\Delta\omega}{4} (\text{GPa}) \quad (1)$$

where $\Delta\omega$ is the wavenumber difference (in cm^{-1}) between the enhanced ϵ -Si peak and the reference non-strained silicon peak at 520 cm^{-1} . These values depicted in Table 1 correspond well with those cited in the literature^[5,14–16] and, as can be seen, the calculated strain for 9-nm ϵ -Si is larger than 17.5- and 42-nm ϵ -Si,

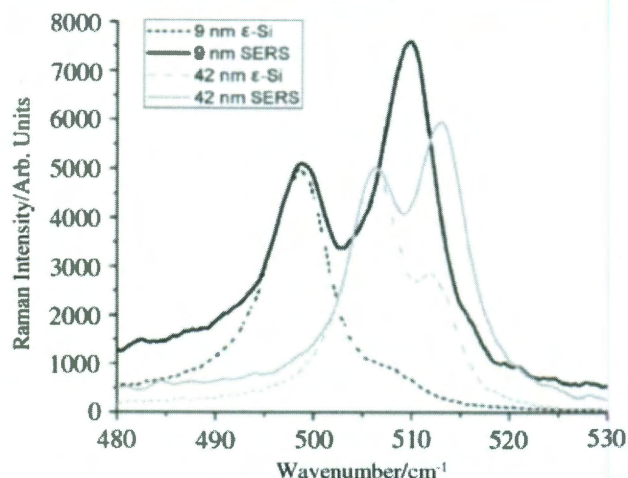


Figure 2. SERS enhancements for sample 3 Ag NPs (80 ± 18 nm) on 9-nm (black) and 42-nm (grey) thick ϵ -Si. Non-SERS Raman spectrum is also shown for 9- and 42-nm thick ϵ -Si (dotted black and grey lines, respectively).

which would be expected because of the larger Ge concentration. Also, the SERS enhancements seem to produce slightly smaller strain values, suggesting that the strain is overspeculated in the non-SERS case because of inaccurate peak assignment.

These results also suggest that ϵ -Si SERS enhancements are a function of NP size, as no SERS enhancements were evident for NPs of size 33 ± 11 nm. This is most likely due to a decrease in the electrical conductivity caused by a decrease in the electron mean free path (55 nm for Ag^[17]), which effectively reduces SERS enhancements, a fact recently illustrated by Prahara *et al.*^[18] Although the source of SERS enhancement is localized surface plasmon resonances throughout the NP thin films, it is also suggested that SERS enhancements vary across the samples due to inhomogeneous variations in PVP coverage from sample to sample which would effectively reduce localized electric field interactions with ϵ -Si due to the r dependence^[19] (where r is the distance between Ag NP and ϵ -Si). These intensity variations could also be due to variations in the so-called SERS hot spots – areas and junctions between aggregated NPs where enormous SERS enhancements are generated in contrast to localized NPs^[20] – but are unlikely as no ϵ -Si is located between these NP junctions. Also, as can be seen in Fig. S5, there are areas (~ 10 – 100 nm²) where no NPs reside, which would reduce electromagnetic enhancements in these areas illuminated by the 4- μ m laser spot.

However, as can be clearly seen in Figs 1 and 2, this solution-based approach (which we call 'Sol-SERS') in obtaining SERS enhancements of nanometer-thick ϵ -Si layers is extremely sensitive, especially for a ϵ -Si thickness of 17.5 nm where a ϵ -Si peak was virtually nondetectable for the pre-NP deposition

case. Considering that only 10 μ l of the sample is needed to perform SERS analysis, up to 1000 experiments can be potentially performed from one single 10-ml stock solution. Sol-SERS is hence an ideal portable-probe technique that can be used to simultaneously amplify the Raman spectra of both SiGe and ϵ -Si layers using a high resolution 488-nm Ar⁺ excitation source. An attempt was also made to quantify these SERS enhancements.

Previous work regarding determination of SERS enhancement factors (EF) can be used to estimate relative SERS EF from sample to sample.^[21] Eqn (2) can be used, with modified parameters, to determine the ϵ -Si SERS EF where I_{SERS} is the SERS intensity, N_{SURF} is the number of molecules bound to the enhancing Ag substrate, I_{NRS} is the normal Raman intensity and N_{VOL} is the number of molecules in the excitation volume^[21,22]:

$$EF = \frac{I_{\text{SERS}}/N_{\text{SURF}}}{I_{\text{NRS}}/N_{\text{VOL}}} \quad (2)$$

In the case of ϵ -Si, where ϵ -Si layers are investigated as opposed to actual molecules, Eqn (2) can be modeled by changing N_{SURF} to the number of ϵ -Si atoms affected by the total evanescent near field (emitted by the illuminated NP layer from localized surface plasmons penetrating into the ϵ -Si) and N_{VOL} to the number of ϵ -Si atoms in the excitation volume (modeled as a cylinder with heights 9, 17.5 or 42 nm). The depth to which the ϵ -Si atoms are affected by the evanescent near field emitted from the NP layer was chosen to be 5 nm from previously published work.^[23] Although there is no technique to date to measure the exact value of the evanescent near-field penetration depth, 5 nm can still be used to obtain a relative EF by keeping this value constant from sample to sample. Finally, as silicon has the face-centered diamond cubic crystal structure with eight atoms per unit cell,^[24] the total number of atoms contained within N_{SURF} and N_{VOL} can be directly calculated for each sample by using Eqn (3):

$$a\text{Si}_{1-x}\text{Ge}_x = 0.5431 + 0.10922x + 0.0002733x^2 \text{ (nm)} \quad (3)$$

where x is the Ge concentration^[25] and $a\text{Si}_{1-x}\text{Ge}_x$ is the calculated lattice constant. However, the degree of precision obtained when using this equation is unnecessary, as an exact value for the evanescent near-field penetration depth still has to be determined.

Using these calculated values for N_{SURF} and N_{VOL} and the experimentally acquired values for I_{SERS} and I_{NRS} (taken from Raman data), the EF values (calculated using the maximum SERS enhancement for each ϵ -Si sample) were found to be 14.17, 12.55 and 26.62 for ϵ -Si of thickness 9, 17.5 and 42 nm, respectively. These calculated EFs are rather small when compared to reported values such as 10^6 – 10^9 .^[23] This is most likely due to the difference in modeling parameters (i.e. atoms as opposed to organic molecules) as well as the fact that only a small two-dimensional (2D) section of the available near field is actually interacting with the ϵ -Si layers. These figures do, however, serve as a figure of qualitative relative merit for each SERS enhancement.

Table 1. SiGe and ϵ -Si SERS/non-SERS peaks for 9, 17.5, and 42 nm thick ϵ -Si samples

Sample (nm)	Non-SERS SiGe peak (cm ⁻¹)	SERS SiGe peak (cm ⁻¹)	Non-SERS ϵ -Si peak (cm ⁻¹)	SERS ϵ -Si peak (cm ⁻¹)	ϵ -Si Strain non-SERS (GPa)	ϵ -Si Strain SERS (GPa)
9	498.25 \pm 0.38	498.49 \pm 0.26	507.64 \pm 0.37	509.21 \pm 0.47	3.09 \pm 0.09	2.70 \pm 0.12
17.5	506.55 \pm 0.21	506.98 \pm 0.33	512.52 \pm 0.27	513.33 \pm 0.37	1.87 \pm 0.07	1.68 \pm 0.09
42	505.90 \pm 0.15	506.46 \pm 0.16	511.96 \pm 0.21	513.26 \pm 0.09	2.01 \pm 0.05	1.69 \pm 0.02

Calculated strain values for both SERS and non-SERS cases are also compared.

Conclusion

To conclude, we have shown that PVP-stabilized Ag NPs of diameter 33–147 nm applied to thin layers of ϵ -Si (9, 17.5, and 42 nm) on top of graded SiGe virtual substrates allow accurate and highly sensitive ϵ -Si SERS characterization. Across this size range, SERS enhancements were greatest for NPs of diameter 80 ± 18 nm. The SERS EFs were roughly estimated by taking into account the number of ϵ -Si atoms in the excitation volume affected by the evanescent near field emitted from the NP layer. While the EFs are relatively low, this portable-probe technique can still produce very reasonable SERS signals for the analysis of nanometer-thick ϵ -Si epilayers. A rapid characterization protocol was also developed to quickly assess the maximum SERS enhancements across relatively large areas ($100 \mu\text{m}^2$), which will invariably aid in reducing ϵ -Si characterization time and expenditure. This Sol-SERS technique is an inexpensive and rapid portable-probe technique for accurate ϵ -Si characterization.

Acknowledgements

The Science Foundation of Ireland is gratefully acknowledged for financial support to this work through Grant number 05/IN/I656 and the Precision Strategic Research Cluster (08/SRC/11411). This research was also supported by the Irish Higher Education Authority Program for Research in Third Level Institutions via the INSPIRE program.

Supporting information

Supporting information may be found in the online version of this article.

References

- [1] D. J. Paul, *Adv. Mater.* **1999**, *11*, 191.
- [2] C. Hincinschi, I. Radu, R. Singh, W. Erfurth, A. P. Milenin, M. Reiche, S. H. Christiansen, U. Gösele, *Mat. Sci. Eng. B* **2006**, *135*, 184.
- [3] J. Parsons, E. H. C. Parker, D. R. Leadley, T. J. Grasby, A. D. Capewell, *Appl. Phys. Lett.* **2007**, *91*, 063127.
- [4] P. Dobrosz, S. J. Bull, S. H. Olsen, A. G. O'Neill, *Surf. Coat. Technol.* **2005**, *200*, 1755.
- [5] W. M. Chen, P. J. McNally, G. D. M. Dillway, J. Bonar, T. Tuomi, A. F. W. Willoughby, *J. Mater. Sci. – Mater. Electron.* **2003**, *14*, 455.
- [6] I. de Wolf, *Semicond. Sci. Technol.* **1996**, *11*, 139.
- [7] N. Hayazawa, M. Motohashi, Y. Saito, S. Kawata, *Appl. Phys. Lett.* **2005**, *86*, 263114.
- [8] S. J. Corr, L. O'Reilly, F. Lucas, P. J. McNally, Enhanced Plasmonic Nanoparticle Interactions: Synthesis Techniques and Characterisation Schemes, Surface Plasmon Photonics 4, De Rode Hoed, Amsterdam, 21–26 June **2009**.
- [9] S. E. Skrabalak, L. Au, X. Li, Y. Xia, *Nat. Protoc.* **2007**, *2*, 2182.
- [10] F. Fievet, J. P. Lagier, B. Blin, B. Beaudoin, M. Figlarz, *Solid State Ionics* **1989**, *32/33*, 198.
- [11] B. Wiley, Y. Sun, B. Mayers, Y. Xia, *Chem. Eur. J.* **2005**, *11*, 454.
- [12] Y. Sun, Y. Xia, *Science* **2002**, *298*, 2176.
- [13] K. Horan, A. Lankinen, L. O'Reilly, N. S. Bennett, P. J. McNally, B. J. Sealy, N. E. B. Cowern, T. O. Tuomi, *Mater. Sci. Eng. B* **2008**, *154–155*, 118.
- [14] S. Nakashima, T. Mitani, M. Ninomiya, K. Matsumoto, *J. Appl. Phys.* **2006**, *99*, 053512.
- [15] J. McCarthy, T. S. Perova, R. A. Moore, S. Bhattacharya, H. Gamble, B. M. Armstrong, *Scanning* **2004**, *26*, 235.
- [16] M. A. Lourenço, D. J. Gardiner, V. Gouvenayre, M. Bowden, *J. Mater. Sci. Lett.* **2000**, *19*, 771.
- [17] U. Kreibitz, C. V. Fragstein, *Z. Phys.* **1969**, *224*, 307.
- [18] S. Prahraj, S. Jana, S. Kundu, S. Pande, T. Pal, *J. Coll. Int. Sci.* **2009**, *333*, 699.
- [19] B. J. Kennedy, S. Spaeth, M. Dickey, K. T. Carron, *J. Phys. Chem. B* **1999**, *103*, 3640.
- [20] P. H. C. Camargo, C. M. Cobley, M. Rycenga, Y. Xia, *Nanotechnology* **2009**, *20*, 434020.
- [21] E. C. Le Ru, E. Blackie, M. Meyer, P. G. Etchegoin, *J. Phys. Chem. C* **2007**, *111*, 13794.
- [22] A. D. McFarland, M. A. Young, J. A. Dieringer, R. P. van Duyne, *J. Phys. Chem. B* **2005**, *109*, 11279.
- [23] P. L. Stiles, J. A. Dieringer, N. C. Shah, R. P. Van Duyne, *Annu. Rev. Anal. Chem.* **2008**, *1*, 601.
- [24] W. C. O'Mara, R. B. Herring, L. P. Hunt, Handbook of Semiconductor Silicon Technology, Noyes Publications: New Jersey, **1990**.
- [25] D. J. Paul, *Semicond. Sci. Technol.* **2004**, *19*, R75.

Appendix F
List of publications

1. E. P. Dillon, C. A. Crouse, and A. R. Barron, *ACS Nano*, 2008, **2**, 156-164.
2. T. A. Strom, E. P. Dillon, C. E. Hamilton, and A. R. Barron, *Chem. Comm.* 2010, **46**, 4097-4099 .
3. K. S. Liao, J. Wang, D. Fruchtl, N. J. Alley, E. Andreoli, E. P. Dillon, A. R. Barron, H. Kim, H. J. Byrne, W. J. Blau, and S. A. Curran, *Chem. Phys. Lett.*, 2010, **489**, 207-211.
4. A. Haldar, S. D. Yambem, K-L, Liao, N. Alley, E. P. Dillon, A. R. Barron, and S. A. Curran, *Thin Solid Films*, 2011, **519**, 6169-6173.
5. S. D. Yambem, A. Haldar, K. S. Liao, E. P. Dillon, A. R. Barron, and S. A. Curran; *Solar Energy Materials and Solar Cells*, 2011, **95**, 2424-2430.
6. S. J. Corr, L. O'Reilly, E. P. Dillon, A. R. Barron, and P. J. McNally, *J. Raman. Spectroscopy*, published online, **2011**.
7. "Polyethyleneimine functionalized nano carbons for CO₂ capture" E. P. Dillon and A. R. Barron; *in preparation*, **2011**
8. " Polyethyleneimine functionalized C₆₀ for high capacity CO₂ capture" E. P. Dillon, A. R. Barron; *in preparation*, **2011**.